A Finite Element Conjugate Heat Transfer Method

Remo Marini

A Thesis

in

The Department

of

Mechanical and Industrial Engineering

Presented in Partial Fulfillment of the Requirements

for the Degree of Master of Applied Science at

Concordia University

Montreal, Quebec, Canada

December 2002

0-612-77980-7

ABSTRACT

A Finite Element Conjugate Heat Transfer Method

Remo Marini

The need to accurately predict heat transfer in aircraft anti-icing systems or in turbomachinery cooling passages is a current topic of Computational Fluid Dynamics (CFD). In both applications, the flow structure is highly complex and three-dimensional. The traditional use of correlations might be useful in describing the average heat transfer behavior, but not the localized effects. Accurate heat transfer predictions are required to design efficient complex cooling or heating schemes and only a full 3D Navier-Stokes code, coupled with a solid conduction code, is the sole alternative. Conjugate Heat Transfer (CHT) is the commonly used term to identify such coupling of convection and conduction across one or several fluid-solid interfaces.

The CHT approach proposed in this thesis solves both the fluid and solid thermal fields simultaneously, in a fully-implicit manner using the infrastructure of a 3D Navier-Stokes flow solver, FENSAP. The algorithm supports 3D structured, unstructured, and hybrid meshes, with mismatched node connectivity and with non-uniform grid densities between fluid and solid domains at CHT interfaces.

The heat transfer validation is assessed for both laminar and turbulent flows against relevant open literature data. The CHT validation is assessed with three cases: a blunt flat plate flow, a fully-developed pipe flow, and the complex piccolo tube system flow in a 3D nacelle lip. The results show that the proposed method can be used as a reliable and cost-effective tool for the analysis and design of thermal anti-icing devices, and can easily be extended to cooled gas turbine components, such as: blades, vanes, shrouds, and disks.

ACKNOWLEDGEMENTS

I would first like to thank Dr. Habashi for serving as my Thesis Supervisor. His continuous technical advice and support have made my years of studies fruitful and interesting. I would also like to thank Dr. Svoboda for serving as my Thesis co-Supervisor.

I am also grateful to Drs. Croce and Guevremont for their many valuable and insightful interventions during the course of my work.

My colleagues at the CFD Lab and at Pratt & Whitney Canada have helped me during numerous conversations we had on the contents of my Thesis. To all of them, thanks.

This work was partially supported by a National Sciences and Engineering Research Council of Canada (NSERC) scholarship, and their role in shaping my future is duly acknowledged.

To my family: Luigi, Anna, and Sabina, my eternal thanks for their continuous encouragement and support during my studies.

Last but not least, I would like to specially thank, Genevieve, for her support, patience, and words of encouragement during my studies.

Table of Contents

List of Figures

List of Tables

Nomenclature

Variables

p, pressure

u, v, w, velocity components

T, temperature

ρ, density

μ, dynamic viscosity

κ, thermal conductivity

t, time

τ, shear stress

c_p, specific heat

Φ, dissipation terms

Re, Reynolds number

Pr, Prandtl number

M, Mach number

q, heat flux

k, turbulent kinetic energy

ε, rate of dissipation of turbulent kinetic energy

f, damping function

y^+, dimensionless distance

u^+, dimensionless velocity

u_τ, friction velocity

ν, kinematic viscosity

P, turbulence dissipation and generation term

Re_T, turbulent Reynolds number

T^+, dimensionless temperature

T^*, characteristic temperature

T_w, wall temperature

T_{aw}, adiabatic wall temperature

q_w, wall heat flux

l_m, Van Driest mixing length

i, turbulence intensity

h, C_h heat transfer coefficient

T_r, reference temperature

ξ, η, local element coordinates

J, Jacobian

ω, Gauss weight

Nu, Nusselt number

St, Stanton number

L, length

W, width

H, height

C, chord

R, radius

D, diameter

$\bar{u}$, average velocity

t, thickness

p, thermal conductivity parameter

Pe, Peclet Number

Subscripts

∞, freestream

i, j, k, indices

I, J, K, L, local node numbering

s, solid

f, fluid

v, virtual grid

l, laminar

t, turbulent

w, wall

p, node-off-the-wall

e, entrance

in, inlet

wi, inner wall

wo, outer wall

Superscripts

s, solid

f, fluid

n, iteration level

m, nodes per element

Constants

R, Gas constant

Pr_t, Turbulent Prandtl number (Pr_t=0.9)

A, Van Driest damping constant (A=26.0)

C_μ, turbulence constant (C_μ=0.09)

C_1, turbulence constant (C_1=1.44)

C_2, turbulence constant (C_2=1.92)

s_κ, turbulence constant (s_κ=1.00)

s_ε, turbulence constant (s_ε=1.00)

κ, Von Karman constant (κ=0.41)

α, Kader constant (α=2.12)

Operators

D, total derivative

∂, partial derivative

δ, Kronecker delta

N, shape function

W, weight function

$\Re$, residual

Units

K, Kelvin

kPa, 10^3 Pascal

W, Watt

m, meter

1. Introduction

1.1. Overview of Conjugate Heat Transfer Analysis

The need to accurately predict heat transfer in aircraft anti-icing systems or in turbomachinery cooling passages is a current topic of Computational Fluid Dynamics (CFD). Although both applications might be at the opposite end of the spectrum in terms of heat transfer (heating versus cooling) both share similar needs and complexities.

In the gas turbine industry, the need for higher efficiencies has driven turbine gas temperatures to exceed allowable metal temperatures in critical regions of the engine, thus requiring hot-end engine components to be cooled. Examples are high pressure cooled vanes, blades, and blade shrouds. Durability engineers must design cooling schemes that target regions of high thermal loads, using the least amount of cooling air. Detecting and eliminating hot spots during the design phase of these components requires a robust design and analysis system. An important challenge is the complex three-dimensional gas flow patterns in such passages. Thus, empirical correlations have traditionally been used to predict the heat load distribution. Convective heat transfer boundary conditions are commonly used for internal cooling schemes as they depend on the geometry and the recognized flow regimes, while the external heat load can be evaluated with simple boundary layer codes with correction factors for film cooling, if applicable. The interaction through the walls, however, is not properly considered in this manner, if conservation of heat fluxes is not addressed.

Another extreme is an aircraft's de-icing or anti-icing system that must remove or completely prevent ice accretion on surfaces before it degrades the aerodynamic performance of the aircraft. Ice accretion on nacelle lips, in particular, can be hazardous to the engine not only because of performance drop off, but through possible ice ingestion, fan blade damage, or combustor flameout. A typical example of a thermal anti-ice device is the use of a piccolo tube system where hot air taken from the engine impinges on the internal wall surfaces of the wing slat or nacelle lips. The heat transfer mechanism in this case is a strong function of the skin temperature, which is not uniformly distributed. The external cooling load also has to be taken into account, as the ratio between the internal and external heat transfer coefficients drive the skin temperature.

In both applications, the flow structure is highly complex and three-dimensional, containing adjacent regions of very high and low speeds and intense or little heat transfer. The use of simple or modified correlations might easily break down, as the extent of these regions cannot be well predicted *a priori*. While correlations might still be useful in describing the average heat transfer behavior, only CFD may be appropriate for localized three-dimensional effects. To close the loop on a design, iterations between the flow calculation and the solid calculation need to be performed to improve the heat balance accuracy.

Conjugate Heat Transfer (CHT) is thus the commonly used description of such interactions involving coupled convection and conduction through one or several fluid-solid interfaces. Solving the fluid and solid regions in a coupled manner offers the following advantages:

- eliminate the need to impose thermal boundary conditions at the walls of interest but only at locations where the temperature or heat flux are known more accurately
- complete interaction of different flows (film cooling with mainstream gaspath flow)
- more accurate temperature predictions for critical components

Two main approaches have been generally adopted for the coupling algorithms, as shown in figures 1.1 and 1.2. They are:

1. boundary condition-exchange method (wall temperature / heat flux, wall temperature / heat transfer coefficients and reference temperature, and Mortar element) where the CFD and the conduction codes are separate entities, and
2. implicit or simultaneous method, where the CFD code also solves the solid conduction equation.

Both methods ensure that the temperature and the heat flux equilibrium conditions are met, if done consistently, at each CHT interface, that is:

$$T_w^f = T_w^s \tag{1.1}$$

and,

$$q_w^f A^f = q_w^s A^s \tag{1.2}$$

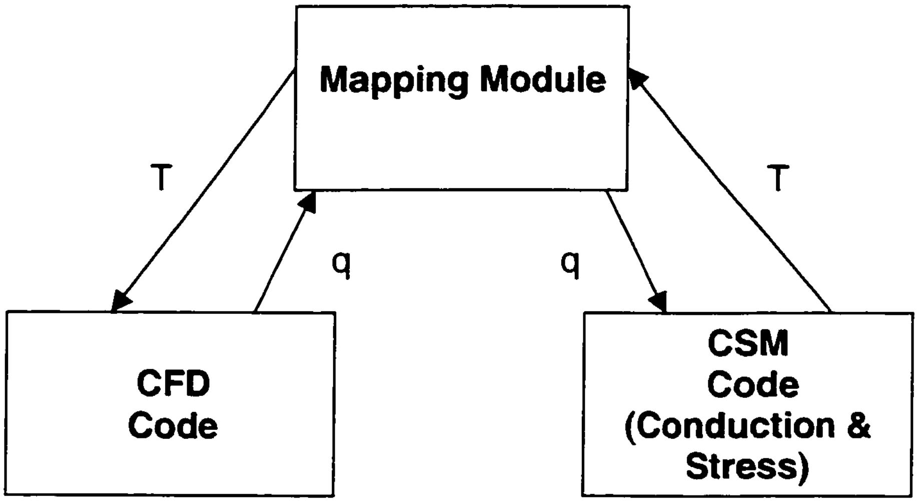

Figure 1.1: Boundary Condition-Exchange Method Flow Chart

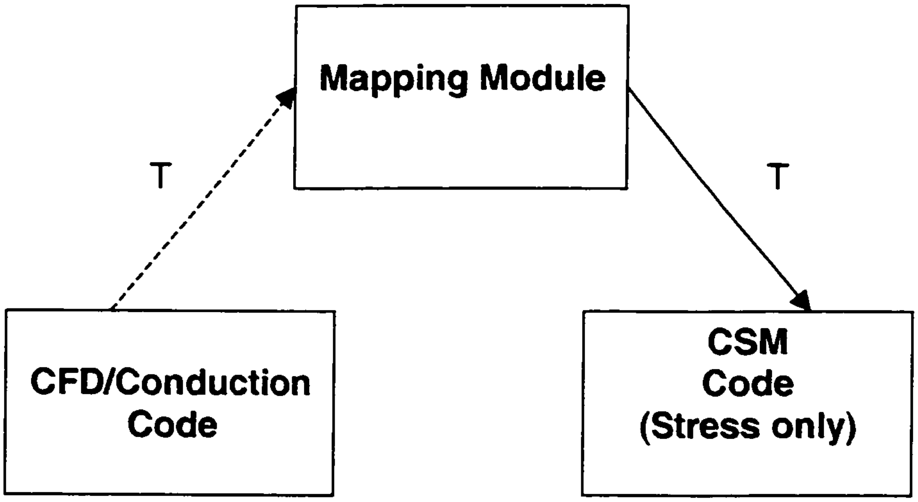

Figure 1.2: Implicit Method Flow Chart

1.2. Literature Review

1.2.1. Boundary Condition-Exchange Approach to CHT

This is the simplest approach used in industry if it is desired to couple the fluid and solid domains for a thermal analysis. The coupling is obtained through an exchange of boundary conditions at the CHT interfaces of interest. This allows the external interaction of state-of-the-art CFD codes with state-of-the-art CSM codes without any changes to them individually. The problem becomes an interface algorithm between the two solvers. This provides maximum flexibility in the design system since it breaks down the CHT problem into smaller pieces, reducing the computational effort in solving the problem. However, a couple of drawbacks are introduced:

1. Under-relaxation might be needed to prevent unphysical solutions when passing the boundary conditions back and forth
2. The sequential solution of the Navier-Stokes and the Conduction problem prevent their parallel execution on a multi-processor machine
3. Different discretization techniques between CFD and CSM codes can cause a loss of accuracy for the heat fluxes calculated
4. Different time step characteristics between CFD and CSM codes can cause numerical instabilities

Croce et al. [1, 2, 3] have published papers on the use of CHT in the aircraft anti-icing field with the boundary condition-exchange approach. The method proposed is the temperature / heat flux approach, described as follows:

1. Solve the fluid field with the CFD code using the Dirichlet boundary condition for interface temperature and obtain a new heat flux distribution at the interface.
2. Transfer the heat flux distribution from the fluid grid to the solid grid using some mapping algorithm (under-relaxation for the heat flux might be required).
3. Solve the solid field with the CSM code using the Neumann boundary condition for the interface heat flux and obtain a new temperature distribution at the interface.
4. Transfer the temperature distribution from the solid grid to the fluid grid using the same mapping code as in step 2 (under-relaxation for the temperature might be required).
5. Repeat steps 1 to 4 until some convergence criterion on the interface is achieved.

This method corresponds to the Shur Complement algorithm for domain decomposition of partial differential equations described by Funaro et al. [4] The use of a Neumann boundary condition for the solid and a Dirichlet boundary condition for the fluid satisfies the stability requirement of the overall system, while the opposite may lead to instabilities. [5]

Imlay et al. propose a variation to this method by damping the solid boundary condition by using an approximate variation of the heat flux with wall temperature. [6] The method proposed is the temperature / heat transfer coefficient and reference temperature approach where:

$$q_w = h(T_w - T_r) \tag{1.3}$$

The method is described as follows:

1. Solve the fluid field with the CFD code using the Dirichlet boundary condition for interface temperature and obtain a new heat flux distribution at the interface.
2. Calculate the heat transfer coefficient using the heat flux distribution and the stagnation temperature of the fluid, one node away from the wall.
3. Transfer the heat transfer coefficient and the stagnation temperature distributions from the fluid grid to the solid grid using some mapping algorithm.
4. Solve the solid field with the CSM code using the Neumann boundary condition for the interface heat flux and obtain a new temperature distribution at the interface.

5. Transfer the temperature distribution from the solid grid to the fluid grid using the same mapping code as in step 3 (under-relaxation for the temperature may be required).
6. Repeat steps 1 to 5 until some convergence criterion on the interface is achieved.

Another way to compute the heat transfer coefficients in step 2 might be to use the adiabatic wall temperature, thus requiring an adiabatic calculation to compute the reference temperature. Montenay et al. state that this method is cumbersome and may lead to negative heat transfer coefficients rendering the conduction problem ill-posed. [7] They propose to use an *a priori* value for the heat transfer coefficient, thus computing a reference fluid temperature with the heat flux distribution such as:

$$q_w = \alpha(T_w - T_r) \tag{1.4}$$

The heat transfer coefficient α used (maintained constant between coupling steps and along the whole fluid-solid interface) is chosen in order to be physically representative of the heat transfer coefficients of the computed flow (as it would be for an uncoupled solution). Montenay et al. show that their method can be viewed as some relaxation method in itself such that [7]:

$$q_w^{s,n+1} = \alpha(T_w^{s,n+1} - T_r^n) \tag{1.5}$$

and,

$$T_r^n = T_w^{f,n} - \frac{q_w^{f,n}}{\alpha} \tag{1.6}$$

and so,

$$q_w^{s,n+1} = q_w^{f,n} + \alpha(T_w^{s,n+1} - T_w^{f,n}) \tag{1.7}$$

The second term of the right-hand-side of equation 1.7 prevents the solid temperature from deviating too much from the fluid temperature, in order to satisfy the heat flux equality. The value of the heat transfer coefficient α is chosen high enough to make the coupled calculation stable since numerical experience has shown that a great value for heat transfer coefficient leads to a more stable calculation but also to a slower rate of convergence of the coupled problem. [7]

Finally, the Mortar element method can be viewed as a variant to the method proposed by Montenay et al. [7] The Mortar element method passes the same heat flux to the solid and fluid at the interface and then uses the resulting temperature difference to change the heat flux by using an *a priori* value for the heat transfer coefficient. The fluid grid is referred to the master grid since it is usually more refined than the solid grid at the interface. The Mortar element method can be described as follows:

1. Solve the fluid field with the CFD code and the solid field with the CSM code using the Neumann boundary condition for interface heat flux and obtain a new temperature distribution at the interface.

2. Interpolate the solid temperature distribution to the fluid grid using some mapping algorithm.
3. Evaluate a new heat flux distribution with the following equation:

   $$q_w^{n+1} = q_w^n + \alpha(T_w^{s,n+1} - T_w^{f,n+1}) \qquad (1.8)$$

4. Interpolate the heat flux distribution from the fluid grid to the solid grid using some mapping algorithm.
5. Repeat steps 1 to 4 until some convergence criterion on the interface is achieved.

The Mortar element method does not require any relaxation for the exchange of boundary conditions since the problem is already relaxed through the use of the *a priori* value for heat transfer coefficient. The method also permits for the parallel execution of both the CFD and CSM codes.

1.2.2. Implicit Approach to CHT

This is the most robust coupling method for CHT computations. The main advantage of this procedure is that the fluid flow and heat transfer are determined in just one code without any further iteration process that can cause numerical instabilities such as the boundary condition-exchange approach. Also, to maintain a high level of robustness, it is critical that the discretization of the heat fluxes be accurate and identical at the fluid-solid interfaces.

Bohn et al. have published papers on the use of CHT in the gas turbine industry with the implicit approach. The numerical scheme for the CHT calculation works on the basis of an implicit finite volume method, combined with a multiblock technique. [8, 9, 10] The Navier-Stokes equations are solved in the fluid blocks, while the Fourier equations are solved in the solid blocks. The coupling between the fluid and solid blocks is achieved via a common wall temperature, resulting from the equality of the local heat fluxes passing through the contacting cell faces. [11] Kao et al. present a similar approach using a Chimera grid system where overlapping grids between fluid and solid domains at the interface ensure temperature and heat flux continuity during the numerical solution. [12]

Han et al. presented results using hybrid triangular/quadrilateral grids in 2D and unstructured prismatic grids in 3D to solve the conjugate problem. [13] Temperature and heat flux continuity is enforced at the fluid-solid interface. Specifying the temperature boundary condition of the flow field with the wall temperature calculated from the solid field satisfies the temperature continuity. Specifying the heat flux boundary condition of the solid field with the value calculated from the flow field satisfies the heat flux continuity. In this manner, the heat flux continuity equation is iteratively enforced at the fluid-solid interface during flow field and heat conduction conjugate calculations. Thakur et al. and Rigby et al. report using the same numerical scheme as Han et al. for their CHT computations. [14, 15]

1.3. Purpose of the Present Work

The present work is motivated by the need to accurately predict heat transfer for aircraft anti-icing systems and for gas turbine cooling applications. The objective was to implement a CHT capability within the CFD code, FENSAP (Finite Element Navier-Stokes Analysis Package), with a minimum of changes to the existing code architecture. [16] The CHT algorithm presented in the following thesis supports 3D structured, unstructured, and hybrid meshes, with mismatched node connectivity between the fluid and solid domains at the interface, and with non uniform grid densities on both sides of the interface. Thus, the use of anisotropic mesh adaptation in the fluid domain is fully supported.

The approach taken is a multi-domain method where the fluid energy equation and the solid energy equation are solved simultaneously in a fully-implicit manner. Each domain has its own mesh, enabling discontinuities in thermal conductivity to be modeled exactly. The energy equations are assembled in the usual finite element method for both fluid and solid domains where the contributions to the residual terms and the matrix influence terms of the equations are distributed consistently. A special treatment is used at the interface to guarantee the temperature and heat flux equality, and the stability of the CHT algorithm. At the interface, the solution advances at each iteration where the temperature is solved only in the solid domain whereas the temperature in the fluid domain is interpolated from the solid domain. The heat fluxes are forced to be identical due to the implicit treatment of the calculation in the weak Galerkin finite element formulation.

1.4 Thesis Content

The thesis begins with a description of the flow solver FENSAP. [16] An overview of the Navier-Stokes equations, the energy equations for the fluid and solid domains, the turbulence modeling, and the heat transfer modeling are presented first. The description of the CHT algorithm implementation in FENSAP follows next. Heat transfer results are then presented in a two-fold manner. First, the heat transfer validation of FENSAP is presented for both laminar flow and turbulent flow, through relevant test cases. Next, the CHT validation of FENSAP is presented with three test cases. The first test is the CHT analysis of a 2D laminar blunt flat plate, the second test case is the CHT analysis of a fully-developed 3D laminar pipe flow, and the last test case is the CHT analysis of a 3D nacelle lip equipped with a piccolo tube system. For each test case, the results are compared to available empirical correlations or open literature experimental results. Finally, the conclusions of the present work and the future work possibilities are stated.

2. The Flow Solver FENSAP

2.1. Introduction

This chapter presents the flow solver FENSAP used in this thesis. An overview of the governing fluid flow equations and the solid conduction equation are presented first. Their non-dimensionalization and their boundary conditions are presented next. Some insight on turbulence modeling with special interest to turbulent heat transfer modeling will also be highlighted, since a considerable amount of modeling had to be developed in the course of the present work. Finally, a description of a higher order heat flux evaluation method is presented as this is of particular interest when dealing with CHT problems.

The governing equations for the fluid flow are the three-dimensional, compressible Reynolds-Averaged Navier-Stokes (RANS) equations. By the Navier-Stokes equations, it is understood to be the physical laws of conservation of mass (the continuity equation), of conservation of momentum (strictly speaking these are the Navier-Stokes equations), of conservation of energy (the energy equation), the equation of state for an ideal gas, and any additional empirical law such as Sutherland's law, which relates the dynamic viscosity and the thermal conductivity to the temperature. The governing equation for the solid is the solid conduction equation.

FENSAP is a general purpose CFD code that can handle 3D structured, unstructured, and hybrid grids. Spatial discretization is carried out by an implicit weak-Galerkin Finite Element Method (FEM), and the equations are linearized by a Newton or quasi-Newton method for the global iteration scheme. To advance the solution in time, an implicit scheme is selected, and an iterative GMRES procedure is used to solve the resulting sparse algebraic system. To enhance the steady-state iterative convergence, a local time stepping method is employed. First or second order artificial dissipation terms are added to the equations to stabilize their numerical resolution. Finally, a high-Reynolds two-equation k-ε model is used to model turbulence. A special element with a logarithmic shape function is used adjacent to the walls to model the law-of-the-wall in the high-Reynolds number turbulence model. This allows the integration of the full governing equations to the walls without the need for grid over-refinement in the boundary layer region.

2.2. Governing Fluid Flow Equations

The fluid flow solution variables in FENSAP are the pressure, the velocity components, the density, and the temperature. The formulation is in conservative form for the continuity and momentum equations, and in non-conservative form for the energy equation as follows (in Cartesian coordinates for simplicity):

The Continuity Equations is:

$$\frac{\partial \rho}{\partial t} + \frac{\partial (\rho u_i)}{\partial x_i} = 0 \tag{2.1}$$

The Momentum Equations are:

$$\frac{\partial (\rho u_i)}{\partial t} + \frac{\partial (\rho u_j u_i)}{\partial x_j} = -\frac{\partial p}{\partial x_i} + \frac{\partial \tau_{ij}}{\partial x_j} \tag{2.2}$$

where,

$$\tau_{ij} = \mu\left(\frac{\partial u_i}{\partial x_j} + \frac{\partial u_j}{\partial x_i} - \frac{2}{3}\delta_{ij}\frac{\partial u_k}{\partial x_k}\right) \tag{2.3}$$

The Energy Equation is:

$$\rho c_p \frac{DT}{Dt} = \frac{Dp}{Dt} + \frac{\partial}{\partial x_i}\left(\kappa \frac{\partial T}{\partial x_i}\right) + \Phi \tag{2.4}$$

where,

$$\Phi = \mu \frac{\partial u_i}{\partial x_j}\left(\frac{\partial u_i}{\partial x_j} + \frac{\partial u_j}{\partial x_i} - \frac{2}{3}\delta_{ij}\frac{\partial u_k}{\partial x_k}\right) \tag{2.5}$$

To close the system of equations we need three more equations. They are:

The Gas Equation of State (for ideal gas):

$$p = \rho RT \tag{2.6}$$

Sutherland's Law for the dynamic viscosity:

$$\frac{\mu}{\mu_\infty} = \left(\frac{T}{T_\infty}\right)^{\frac{3}{2}} \left(\frac{T_\infty + 110^\circ K}{T + 110^\circ K}\right) \tag{2.7}$$

Sutherland's Law for the thermal conductivity:

$$\frac{\kappa}{\kappa_\infty} = \left(\frac{T}{T_\infty}\right)^{\frac{3}{2}} \left(\frac{T_\infty + 133.7^\circ K}{T + 133.7^\circ K}\right) \tag{2.8}$$

This system now consists of nine equations in nine variables: the pressure p, the velocity components u_i, the temperature T, the density ρ, the dynamic viscosity μ, and the thermal conductivity κ.

2.3. Governing Solid Conduction Equation

Assuming the solid is isotropic, the governing equation for the heat transfer in the structure is the heat conduction equation. The formulation is in non-conservative form for the temperature as follows (in Cartesian coordinates for simplicity):

$$\rho_s c_s \frac{\partial T}{\partial t} = \frac{\partial}{\partial x_i}\left(\kappa_s \frac{\partial T}{\partial x_i} \right) \tag{2.9}$$

This system consists of one equation in one variable: the temperature T. The density ρ_s and the specific heat c_s are constant for the material, while the thermal conductivity κ_s can be constant or a function of temperature when a table is provided as an input. There are no heat sources or heat sinks in the solid energy equation.

2.4. Non-Dimensionalization of the Governing Equations

The governing equations are often written in non-dimensional form so that the non-dimensional flow variables are usually of the order of magnitude of unity, a convenient means in computational work to minimize numerical round-off errors resulting from the different flow variable scales.

Since FENSAP is a CFD code tailored for external flow computation, the fluid flow governing equations are non-dimensionalized as follows:

$$x_i^* = \frac{x_i}{l_\infty}, \quad \rho^* = \frac{\rho}{\rho_\infty}, \quad u_i^* = \frac{u_i}{U_\infty}, \quad t^* = \frac{tU_\infty}{l_\infty}, \quad p^* = \frac{p}{\rho_\infty U_\infty^2},$$

$$T^* = \frac{T}{T_\infty}, \quad \mu^* = \frac{\mu}{\mu_\infty}, \quad \kappa^* = \frac{\kappa}{\kappa_\infty}, \quad c_p^* = \frac{c_p}{c_{p,\infty}}$$

To maintain consistency through the non-dimensionalization of the governing equations, the solid conduction equation is non-dimensionalized by introducing the following dimensionless variables:

$$x_i^* = \frac{x_i}{l_\infty}, \quad T^* = \frac{T}{T_\infty}, \quad \rho_s^* = \frac{\rho_s}{\rho_\infty}, \quad c_s^* = \frac{c_s}{c_{p,\infty}}, \quad \kappa_s^* = \frac{\kappa_s}{\kappa_\infty}$$

In the above variables, l_∞ is the characteristic length of the physical problem; U_∞ is the freestream flow velocity based on the freestream Mach number M_∞ and freestream temperature T_∞; ρ_∞ is the freestream density; μ_∞ is the freestream dynamic viscosity; κ_∞ is the freestream thermal conductivity; $c_{p\infty}$ is the freestream specific heat.

Omitting the star notation, the non-dimensional forms of the equations (ignoring Sutherland's law) are as follows:

The Continuity Equation is:

$$\frac{\partial \rho}{\partial t}+\frac{\partial(\rho u_i)}{\partial x_i}=0 \tag{2.10}$$

The Momentum Equations are:

$$\frac{\partial(\rho u_i)}{\partial t}+\frac{\partial(\rho u_j u_i)}{\partial x_j}=-\frac{\partial p}{\partial x_i}+\frac{1}{Re_\infty}\frac{\partial \tau_{ij}}{\partial x_j} \tag{2.11}$$

The Fluid Energy Equation is:

$$\frac{\rho c_p}{(\gamma_\infty-1)M_\infty^2}\frac{DT}{Dt}=\frac{Dp}{Dt}+\frac{1}{Re_\infty Pr_\infty(\gamma_\infty-1)M_\infty^2}\frac{\partial}{\partial x_i}\left(\kappa\frac{\partial T}{\partial x_i}\right)+\frac{1}{Re_\infty}\Phi \tag{2.12}$$

The Gas Equation of State (for ideal gas):

$$p=\frac{\rho T}{\gamma M_\infty^2} \tag{2.13}$$

The Solid Energy Equation is:

$$\rho_s c_s\frac{\partial T}{\partial t}=\frac{1}{Re_\infty Pr_\infty(\gamma_\infty-1)M_\infty^2}\frac{\partial}{\partial x_i}\left(\kappa_s\frac{\partial T}{\partial x_i}\right) \tag{2.14}$$

Some recognized variables appear such as the Reynolds number Re_∞, the Prandtl number Pr_∞, and the Mach number M_∞:

$$Re_\infty=\frac{\rho_\infty l_\infty U_\infty}{\mu_\infty},\qquad Pr_\infty=\frac{\mu_\infty c_{p,\infty}}{\kappa_\infty},\qquad M_\infty=\sqrt{\gamma_\infty R T_\infty}$$

2.5. Boundary Conditions for the Governing Equations

For simplicity, only the conventional boundary conditions for subsonic flows are listed. They are:

1. Inlet: velocity components u_i, and temperature T are imposed
2. Walls: velocity components $u_i=0$, and temperature T or heat flux q are imposed
3. Exit: pressure p is imposed

For the solid conduction equation, the conventional boundary condition is:

4. Walls: temperature T or heat flux q are imposed

However, when a CHT problem is being solved some additional boundary conditions arise at the wall interface to ensure continuity for temperature and heat flux:

$$T_w^f = T_w^s \text{ and, } q_w^f A_f = q_w^s A_s \tag{2.15}$$

These two boundary conditions are enforced iteratively and not externally during the solution of the CHT problem.

2.6. Turbulence Modeling

For turbulence closure, the standard high-Reynolds $\kappa-\varepsilon$ model from Jones and Launder is employed in the version of FENSAP used in this thesis. [17] However, a few minor low-Reynolds corrections are introduced through damping functions. These modifications allow the prediction of a variety of low-Reynolds number problems with particular interest to heat transfer.

The turbulent viscosity is estimated from the turbulent kinetic energy κ, and the rate of dissipation of turbulent kinetic energy ε, by the following relationship:

$$\mu_t = \frac{C_\mu f_\mu \rho k^2}{\varepsilon} \tag{2.16}$$

The turbulent thermal conductivity is estimated using the turbulent viscosity and the assumption of a constant turbulent Prandtl number (Pr_t=0.9), as follows:

$$k_t = \frac{c_p \mu_t}{Pr_t} \tag{2.17}$$

Thus, the concept of effective viscosity and conductivity is used such that:

$\mu_{eff} = \mu_l + \mu_t$ and, $\kappa_{eff} = \kappa_l + \kappa_t$

The turbulent viscosity damping function is modeled through the Van-Driest damping function as follows [18]:

$$f_\mu = 1.0 - \exp\left(\frac{-y^+}{A}\right), \qquad y^+ = \frac{y u_\tau}{\nu} \tag{2.18}$$

where the constant A=26.0.

2.6.1. Turbulence Equations

The turbulent kinetic energy and the rate of dissipation of turbulent kinetic energy are estimated by their own transport equations which can be written in non-dimensional form, as follows (in Cartesian coordinates for simplicity):

$$\frac{\partial(\rho k)}{\partial t}+\frac{\partial(\rho u_i k)}{\partial x_i}=\frac{1}{Re_\infty}\left[\frac{\partial}{\partial x_i}\left[\left(\mu+\frac{\mu_t}{\sigma_k}\right)\frac{\partial k}{\partial x_i}\right]+P\right]-\rho\varepsilon \qquad (2.19)$$

$$\frac{\partial(\rho \varepsilon)}{\partial t}+\frac{\partial(\rho u_i \varepsilon)}{\partial x_i}=\frac{1}{Re_\infty}\left[\frac{\partial}{\partial x_i}\left[\left(\mu+\frac{\mu_t}{\sigma_\varepsilon}\right)\frac{\partial \varepsilon}{\partial x_i}\right]+C_1 f_1 P\frac{\rho}{\varepsilon}\right]-C_2 f_2 \rho\frac{\varepsilon^2}{k} \qquad (2.20)$$

where,

$$P=\tau_{ij}\frac{\partial u_i}{\partial x_j}=\left[\mu_t\left(\frac{\partial u_i}{\partial x_j}+\frac{\partial u_j}{\partial x_i}\right)-\frac{2}{3}\mu_t\frac{\partial u_l}{\partial x_l}\delta_{ij}\right]\frac{\partial u_i}{\partial x_j} \qquad (2.21)$$

The turbulence equations were non-dimensionalized as follows:

$$k^*=\frac{k}{U_\infty^2}, \qquad \varepsilon^*=\varepsilon\frac{l_\infty}{U_\infty^3}$$

The constants in the $\kappa-\varepsilon$ turbulence model have the following values:

$$C_\mu=0.09, \quad C_1=1.44, \quad C_2=1.92, \quad s_\kappa=1.0, \quad s_\varepsilon=1.0$$

Finally, the damping functions for the source terms in the $\kappa-\varepsilon$ equations are similar to the Jones and Launder damping functions as follows [19]:

$$f_1=1.0 \qquad (2.22)$$

$$f_2=1.0-0.3\exp(-R_t^2), \qquad R_t=\frac{k^2}{\varepsilon\nu} \qquad (2.23)$$

2.6.2. Boundary Conditions and Wall Modeling

The inlet boundary conditions for κ and ε is specified from physical considerations. The turbulence intensity is usually measured for experimental setups, or can be deduced for industrial applications. Thus, the turbulence kinetic energy can be obtained from the turbulence intensity as:

$$k = \frac{3}{2} i_{\text{inlet}}^2 U_{\text{inlet}}^2 \tag{2.24}$$

and, the dissipation rate is obtained by deducing the level of turbulent viscosity of the inlet flow as:

$$\varepsilon = \frac{C_\mu f_\mu \rho k^2}{\mu_{\text{t,inlet}}} \tag{2.25}$$

For high-Reynolds number flows, wall functions are usually applied to avoid excessively large grids near walls, although this is becoming less of an issue with the increase of computer storage and speed. The idea of wall functions is to apply Dirichlet boundary conditions for velocity, temperature, turbulent kinetic energy, and rate of dissipation of turbulent kinetic energy at the first node-off-the-wall. The governing equations are then not resolved in the layer of elements above the wall.

Thus, through the assumption of the velocity profile near the wall modeled with the universal turbulent profile, the boundary conditions for the $\kappa - \varepsilon$ model within a validity range of $y^+>30$ are:

$$k = \frac{u_\tau^2}{\sqrt{C_\mu}}, \qquad \varepsilon = C_\mu^{3/4}\frac{k^{3/4}}{\kappa y} = \frac{u_\tau^3}{\kappa y} \tag{2.26}$$

In the version of FENSAP used in this thesis, a damping function is introduced to the ε equation *a la* Mohamadi [20] such that:

$$\varepsilon = f_\varepsilon \varepsilon, \qquad f_\varepsilon = \frac{1}{1-\exp\left(\frac{-y^+ C_\mu^{3/4}}{2\kappa}\right)} \tag{2.27}$$

Through limited numerical investigation, this permits the range of y^+ to be lower than the recommended range and still maintain the validity of the boundary conditions for the $\kappa-\varepsilon$ model.

In Finite Element methods, a methodology has been developed which allows the continuity, momentum, and energy equations to be resolved within the wall elements for high-Reynolds flows. [21, 22] In the wall elements, the shape functions for velocity and temperature are modified to include some universal profile in the normal direction. The shape functions remain linear in the tangential directions.

2.6.2.1. Velocity Wall Element Modeling

To characterize the behavior of the velocity near the wall, a dimensionless velocity u^+ is introduced such as:

$$u^+ = \frac{u}{u_\tau} \tag{2.28}$$

The experimentally observed velocity profiles across the viscous sublayer ($y^+ < 5$), and the fully turbulent layer ($y^+ > 30$) can be described for the dimensionless slip velocity u^+ by a linear profile in the sublayer:

$$u^+ = y^+ \tag{2.29}$$

and, by a logarithmic profile in the log layer:

$$u^+ = \ln\left(\frac{y^+}{\kappa}\right) + 5.5 \tag{2.30}$$

The transitional sublayer ($5 < y^+ < 30$) can be described by some curve fit to smoothly join both the sublayer and the log layer.

In the present thesis, the velocity shape function is derived by Reichardt's Law of the Wall [21]:

$$u^+ = \frac{1}{\kappa}\ln(1.0 + 0.4y^+) + 7.8\left[1.0 - \exp\left(\frac{-y^+}{11.0}\right) - \frac{y^+}{11.0}\exp(-0.33y^+)\right] \tag{2.31}$$

A similar profile is the Spalding Law of the Wall, shown for completeness [23]:

$$y^+ = u^+ + \exp(-\kappa B)\left(\exp(z) - 1.0 - z - \frac{z^2}{2} - \frac{z^3}{6}\right),\ z = \kappa u^+ \tag{2.32}$$

Both these profiles match the experimental observations, as shown in figure 2.1.

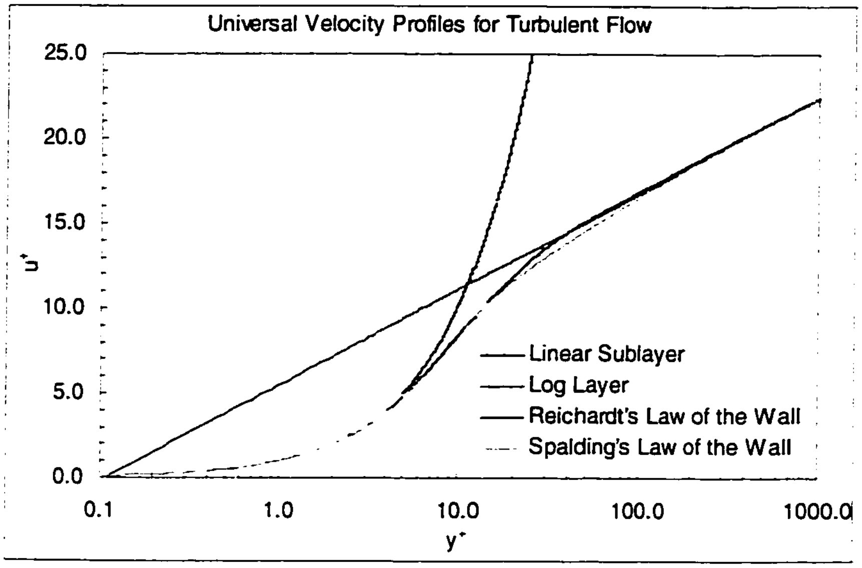

Figure 2.1: Universal Velocity Profiles for Turbulent Flow

2.6.2.2. Temperature Wall Element Modeling

To characterize the behavior of the temperature near the wall, a dimensionless temperature T^+ is introduced such as:

$$T^+ = \frac{T_w - T_p}{T^*}, \qquad T^* = \frac{q_w}{\rho c_p u_\tau} \tag{2.33}$$

Experimental work done by Kader on temperature profiles in turbulent boundary layers reveals that across the thermal viscous sublayer ($y^+ < 30$, for gases), and the fully turbulent thermal layer ($y^+ > 30$) the temperature profiles can be described for the dimensionless temperature T^+ by a linear profile in the thermal sublayer [24]:

$$T^+ = \Pr y^+ \tag{2.34}$$

and, by a logarithmic profile in the thermal log-layer:

$$T^+ = \alpha \ln(y^+) + \beta(\Pr) \tag{2.35}$$

where,

$$\alpha = 2.12 \text{ and, } \beta(\mathrm{Pr}) = (3.85\,\mathrm{Pr}^{1/3} - 1.3)^2 + 2.12\ln(\mathrm{Pr}) \tag{2.36}$$

Kader developed a universal equation for the whole range of y^+ [24]:

$$T^+ = \mathrm{Pr}\,y^+ \exp(-\Gamma) + \left[\alpha \ln(1+y^+) + \beta(\mathrm{Pr})\right]\exp(\frac{-1}{\Gamma}) \tag{2.37}$$

$$\text{where, } \Gamma = \frac{0.01(\mathrm{Pr}\,y^+)^4}{1+5\,\mathrm{Pr}\,y^+} \tag{2.38}$$

In the present thesis, the temperature shape function is inspired by the Spalding Law of the Wall for velocity, and is given by the following curve fit:

$$y^+ = \frac{T^+}{\mathrm{Pr}} + \exp(-\frac{\beta(\mathrm{Pr})}{\alpha})\left(\exp(z) - 1.0 - z - \frac{z^2}{2} - \frac{z^3}{6}\right),\ z = \frac{T^+}{\alpha} \tag{2.39}$$

This curve fit agrees well with the Kader curves as shown in figure 2.2 (Pr=0.72 for simplicity). It actually has a smoother blend fit between the linear and the logarithmic region. This is important when computing a first derivative for T^+.

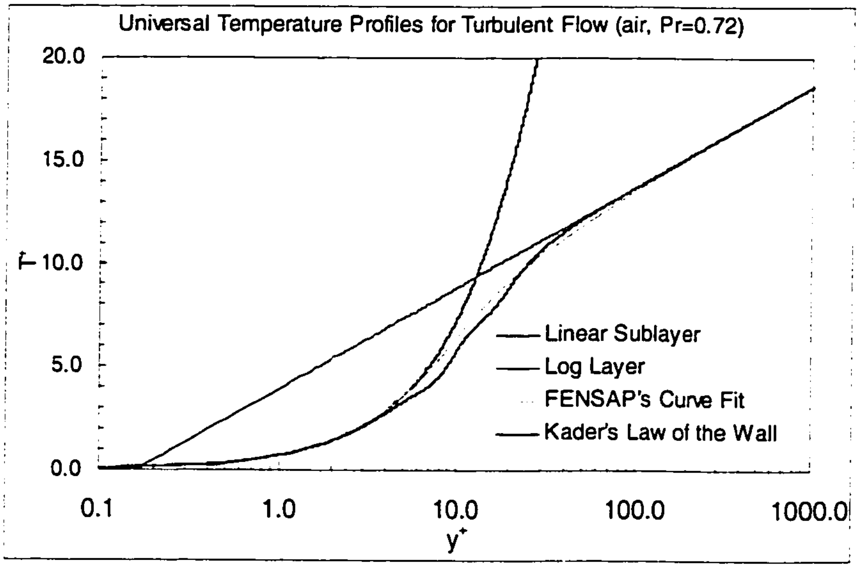

Figure 2.2: Universal Temperature Profiles for Turbulent Flow (air, Pr=0.72)

2.6.2.3. Turbulent Viscosity and Conductivity Wall Element Modeling

Finally, since the standard $\kappa-\varepsilon$ model is not solved in the vicinity of the walls, a modeling scheme must be devised to simulate the variation of the turbulent viscosity in the special element. Van Driest's mixing length model is used such as [18]:

$$\mu_t = \rho l_m^2 \left[\left(\frac{\partial u_i}{\partial x_j} + \frac{\partial u_j}{\partial x_i} \right) \frac{\partial u_j}{\partial x_j} \right]^{1/2} \tag{2.40}$$

where, l_m is the mixing length obtained from Van Driest's expression [18]:

$$l_m = \kappa y \left[1 - \exp\left(-\frac{y^+}{A} \right) \right] \tag{2.41}$$

In the present thesis, the turbulent viscosity shape function is derived with a simplified one-dimensional Van Driest's mixing length theory such as (assuming that y is the normal coordinate while x is the tangential coordinate) [18]:

$$\mu_t = \rho l_m^2 \left| \frac{\partial u}{\partial y} \right| \tag{2.42}$$

The turbulent thermal conductivity is calculated in the wall element via the assumption of a constant turbulent Prandtl number (Pr_t=0.9) with equation 2.17.

2.7. Consistent Heat Flux Evaluation

An accurate and consistent heat flux evaluation is of particular importance when dealing with conjugate heat transfer computations. For the case when the temperature is specified at the wall, it is often required to evaluate the heat flux once a converged solution is obtained. The intuitive method would be to simply evaluate the wall temperature gradient using the shape function derivatives at the wall face within the wall element. This would be a "first-order" method and would give inaccurate results unless a fine mesh was used. This would also not be consistent with the use of wall elements since they purposely require a "relatively coarse" mesh at the wall. In FENSAP, heat fluxes are post-processed via the consistent FEM approach of Gresho et al. allowing a more consistent and "second-order" accurate method to evaluate the heat flux. [25]

When the temperature is specified at the wall, the discretized energy equations are replaced by the Dirichlet boundary condition. These discretized equations at the wall nodes are used in "reverse" to evaluate the heat flux, i.e. the elements adjacent to a wall are once more re-assembled, with the temperature imposed as a Dirichlet boundary condition and the heat flux considered as the unknown. Gresho et al. labeled the method a "consistent" method for the simple reason that if the heat flux were implemented as the boundary condition, the exact same temperature field would result. [25] The later is not true if the heat flux evaluated through derivatives were employed. Finally, the Gresho heat fluxes are node-based, while the derivative heat fluxes are face-based.

The weak-Galerkin discretized fluid energy equation is as follows:

$$\oiint W_i\left[\frac{1}{Re_\infty Pr_\infty(\gamma_\infty-1)M_\infty^2}\left(\kappa_{eff}\frac{\partial T}{\partial x_i}\right)\right]dS = \qquad (2.43)$$

$$\iiint\left[W_i\left(\frac{\rho c_p}{(\gamma_\infty-1)M_\infty^2}\frac{DT}{Dt}-\frac{Dp}{Dt}-\frac{1}{Re_\infty}\Phi\right)+\frac{\partial W_i}{\partial x_k}\left(\frac{1}{Re_\infty Pr_\infty(\gamma_\infty-1)M_\infty^2}\frac{\partial}{\partial x_i}\left(\kappa_{eff}\frac{\partial T}{\partial x_i}\right)\right)\right]dV$$

Replacing the temperature gradient term by the heat flux in the surface integral one obtains:

$$\oiint W_i\left[\frac{1}{Re_\infty Pr_\infty(\gamma_\infty-1)M_\infty^2}q\right]dS = \qquad (2.44)$$

$$\iiint\left[W_i\left(\frac{\rho c_p}{(\gamma_\infty-1)M_\infty^2}\frac{DT}{Dt}-\frac{Dp}{Dt}-\frac{1}{Re_\infty}\Phi\right)+\frac{\partial W_i}{\partial x_k}\left(\frac{1}{Re_\infty Pr_\infty(\gamma_\infty-1)M_\infty^2}\frac{\partial}{\partial x_i}\left(\kappa_{eff}\frac{\partial T}{\partial x_i}\right)\right)\right]dV$$

The solution variable q is then discretized on the element face using the 2D shape functions N_j:

$$q=\sum_{j=1}^{m}N_jq_j \qquad (2.45)$$

Replacing back into the heat flux equation, and letting $W_i=N_i$ gives:

$$\sum_{j=1}^{m}\left(\oiint\left[\frac{1}{Re_\infty Pr_\infty(\gamma_\infty-1)M_\infty^2}\right][N_iN_j]dS\right)q_j \qquad (2.46)$$

$$\iiint\left[W_i\left(\frac{\rho c_p}{(\gamma_\infty-1)M_\infty^2}\frac{DT}{Dt}-\frac{Dp}{Dt}-\frac{1}{Re_\infty}\Phi\right)+\frac{\partial W_i}{\partial x_k}\left(\frac{1}{Re_\infty Pr_\infty(\gamma_\infty-1)M_\infty^2}\frac{\partial}{\partial x_i}\left(\kappa_{eff}\frac{\partial T}{\partial x_i}\right)\right)\right]dV$$

The right-hand-side is known at solution convergence and is evaluated in the usual manner (numerical integration). The left-hand-side N_iN_j is known as the consistent mass matrix. To eliminate the need to solve a matrix, mass-lumping (row sum technique), usually done at the element level, can also be used such as $\delta_{ij}N_iN_j$, i.e. N_iN_i thus, rendering the matrix diagonal. By comparing consistent and lumped masses, Thornton has verified that the lumped mass approach is generally a viable alternative in that it is simpler, sometimes more accurate because there are no numerical wiggles, and generally more cost effective; also, and importantly, the correct global balances are still obtained. [25, 26] The same procedure applies for the evaluation of the solid heat fluxes.

3. Implementation of Conjugate Heat Transfer in FENSAP

3.1. Introduction

The CHT algorithm implemented in FENSAP is a multi-domain method where the fluid energy equation and the solid energy equation are solved simultaneously in a fully-implicit manner. The CHT algorithm supports 3D structured, unstructured, and hybrid meshes, with mismatched node connectivity and with non-uniform grid densities at the interface between the fluid and solid domains. Each domain has its own mesh, enabling discontinuities in thermal conductivity to be modeled exactly.

The method ensures that the temperature equality and the heat flux equality conditions are respected iteratively at the CHT interface during the solution of the energy equation, that is:

$$T_w^f = T_w^s \tag{3.1}$$

and,

$$q_w^f A^f = q_w^s A^s \tag{3.2}$$

At the CHT interface, a master grid is generated by splitting all the edges of the fluid and solid grids to create a triangular grid where both the fluid and solid grid are subsets. A conservative interpolation scheme is used to ensure the heat flux equality of equation 3.2 at the CHT interface.

3.2. Conjugate Heat Transfer Methodology

The methodology adopted in this thesis is inspired by the work of Sleiman in multistage turbomachinery for rotor-stator interaction implicit treatment. [27] The idea is to treat the CHT problem as a multi-domain problem. Each domain has its own meshes which are later combined together inside FENSAP. However, the elements are not connected at the CHT interfaces through the nodal connectivity nor do the meshes need to have matching nodes.

At a CHT interface, the nodes of the solid grid will be termed the "live" nodes, while the nodes of the fluid grid will be termed the "dead" nodes. Also, the fluid elements at the CHT interface will be termed "dead" elements, while any other element in the fluid or solid domains will be termed "live" elements during the assembly of the energy equation.

The assembly of the discretized finite element energy equations for both the live fluid elements and the live solid elements is performed as usual, that is the element contributions to the residual terms and the matrix terms are distributed according to the node connectivity of the meshes. At the interface, some sort of node connectivity must be built to ensure that the fluid nodes and the solid nodes become part of the same system of equations being solved. One set of nodes at the interface is thus redundant: the dead fluid nodes. Note that if the meshes were matched at the interface, then an easy way to connect both domains is to set the fluid nodes periodic to the solid nodes. However, at the interface between the fluid grid and the solid grid, the meshes can be discontinuous as shown in figure 3.1 for a typical mismatched grid. Square elements are used for simplicity but any type of linear element is supported at the CHT interface.

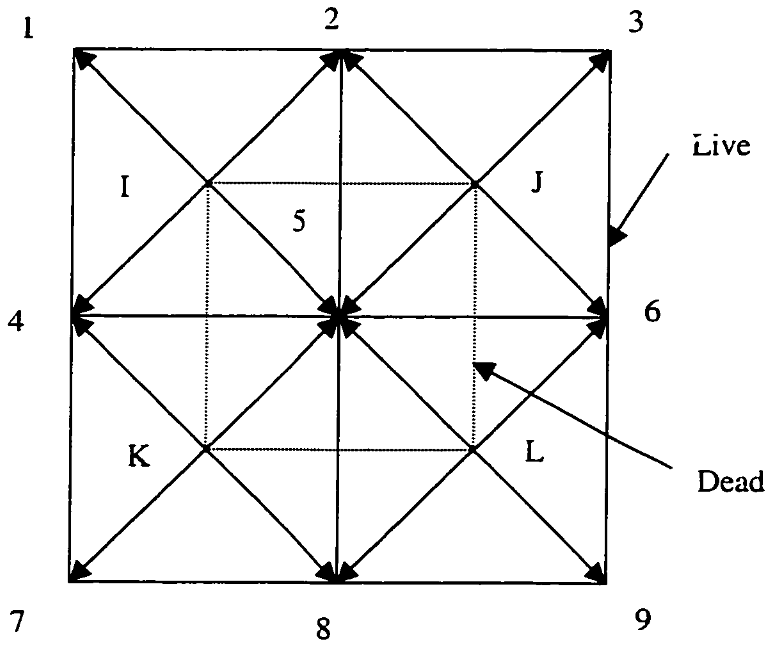

Figure 3.1: Mismatched Grids at the CHT Interface [27]

The initial approach investigated in this thesis was to distribute the contributions of the energy equation residual and matrix terms in a consistent manner. Basically, the live solid nodes (nodes 1 to 9) have a direct representation in the matrix solver and so, the finite element solution at the nodes is updated through the iterative solver. However, dead nodes (nodes I to L) have an indirect representation in the matrix solver since their contributions are distributed, based upon their physical location with respect to the live elements, to the live nodes.

For example, nodes I, J, K and, L lie in the middle of the four node elements: 2-5-4-1, 3-6-5-2, 6-9-8-5 and, 5-8-7-4, respectively. Assembly of the live elements is carried out using the standard finite element method. A different approach is taken in the assembly of the dead elements. The contributions of the dead node I are distributed to nodes 1, 2, 5, and 4, according to the value of the finite element shape functions at node I, as shown in table 1. The same procedure applies to nodes J, K, and L. [27]

Local Nodes	1	2	3	4
Global Nodes	2	5	4	1
Weight	0.25	0.25	0.25	0.25

Table 3.1: Contributions of the Dead Node I into the Live Nodes [27]

A Dirichlet boundary condition is imposed at node I, and therefore, it has no equation number. However, it is still assembled in the matrix and the residual. The contributions of equation I are distributed into the equations of the global nodes 2, 5, 4, and 1. At the end of the iteration, the temperature at node I can be written as:

$$T_I = \sum_{m=1}^{ndperl} N_m T_m \tag{3.3}$$

Thus, the temperature at node I is updated through the solution at nodes 2, 5, 4, and 1. The same procedure applies for nodes J, K, and L. By doing so, the residual and the solution at node I are computed in a consistent manner. Note that this method is consistent when the grids are matching at the interface, and leads to the common finite element assembly procedure as for any internal node. However, this approach necessitates close grid densities at the interface between the solid and the fluid grids. [27] If this condition is not met, then the redistribution of the residuals will become non-conformal and the conservation of the internal flux contribution will no longer be met. This is a fundamental principle for a discretized problem in finite elements. One might say that most of the time, the solid grid at the interface will be coarser than the fluid grid and the residual contributions will remain consistent. However, if the reverse were true, as might be the case when mesh adaptation is present, then the redistribution of the residuals will become inconsistent, as some nodes in the live grid will not receive any contributions for the residuals during the assembly. This is referred to hanging nodes, and if they appear, the scheme becomes non-conservative. Residuals are already area-weighted in the elements, so redistributing the residual contributions using some sort of area averaging was thought of but the implementation of this idea led to an ambiguous finite element procedure. Thus, a new method to redistribute the residuals or, a new interpretation of the discussed method has been devised to handle the general non-matching grids at the interface.

In the case of the matrix terms, it is less critical because the iterative matrix is not the total matrix but a preconditioning matrix. Thus, a non-conservative approach is still valid since it will keep the dominant matrix terms in the FEM formulation to enhance the stability of the iterative procedure. Not keeping these matrix terms lead to possible breakdown of the iterative CHT procedure and will not be discussed further. Besides, any other implementation of the matrix terms in a conservative manner was ambiguous.

Let us look at the residual contributions for the fluid and solid energy equations. The weak-Galerkin linearized fluid energy equation residual is:

$$\mathfrak{R}_i^f = -\oiint W_i \left[\frac{1}{\mathrm{Re}_\infty \mathrm{Pr}_\infty (\gamma_\infty - 1) M_\infty^2} \left(\kappa_{eff} \frac{\partial T}{\partial x_i} \right) \right] dS \tag{3.4}$$

$$+ \iiint \left[W_i \left(\frac{\rho c_p}{(\gamma_\infty - 1) M_\infty^2} \frac{DT}{Dt} - \frac{Dp}{Dt} - \frac{1}{\mathrm{Re}_\infty} \Phi \right) + \frac{\partial W_i}{\partial x_k} \left(\frac{1}{\mathrm{Re}_\infty \mathrm{Pr}_\infty (\gamma_\infty - 1) M_\infty^2} \frac{\partial}{\partial x_i} \left(\kappa_{eff} \frac{\partial T}{\partial x_i} \right) \right) \right] dV$$

The weak-Galerkin linearized solid energy equation residual is:

$$\mathfrak{R}_i^s = -\oiint W_i \left[\frac{1}{\mathrm{Re}_\infty \mathrm{Pr}_\infty (\gamma_\infty - 1) M_\infty^2} \left(\kappa_s \frac{\partial T}{\partial x_i} \right) \right] dS \tag{3.5}$$

$$+ \iiint \left[W_i \left(\frac{\rho_s c_s}{(\gamma_\infty - 1) M_\infty^2} \frac{\partial T}{\partial t} \right) + \frac{\partial W_i}{\partial x_k} \left(\frac{1}{\mathrm{Re}_\infty \mathrm{Pr}_\infty (\gamma_\infty - 1) M_\infty^2} \frac{\partial}{\partial x_i} \left(\kappa_s \frac{\partial T}{\partial x_i} \right) \right) \right] dV$$

When assembling the finite element equations, a usual assumption to make is to neglect the surface integral contributions in the residuals for internal nodes. That is, it is assumed that their contributions cancel out from both sides of neighboring elements. Thus, the remaining terms for the interface fluid residual are:

$$\mathfrak{R}_i^f = \iiint \left[W_i \left(\frac{\rho c_p}{(\gamma_\infty - 1) M_\infty^2} \frac{DT}{Dt} - \frac{Dp}{Dt} - \frac{1}{\mathrm{Re}_\infty} \Phi \right) + \frac{\partial W_i}{\partial x_k} \left(\frac{1}{\mathrm{Re}_\infty \mathrm{Pr}_\infty (\gamma_\infty - 1) M_\infty^2} \frac{\partial}{\partial x_i} \left(\kappa_{eff} \frac{\partial T}{\partial x_i} \right) \right) \right] dV \tag{3.6}$$

The remaining terms for the interface solid residual are:

$$\mathfrak{R}_i^s = \iiint \left[W_i \left(\frac{\rho_s c_s}{(\gamma_\infty - 1)M_\infty^2} \frac{\partial T}{\partial t} \right) + \frac{\partial W_i}{\partial x_k} \left(\frac{1}{Re_\infty Pr_\infty (\gamma_\infty - 1)M_\infty^2} \frac{\partial}{\partial x_i} \left(\kappa_s \frac{\partial T}{\partial x_i} \right) \right) \right] dV \qquad (3.7)$$

The residual terms in equations 3.6 and 3.7 correspond to the right-hand-side contributions of Gresho's heat flux for the fluid and solid domains, respectively, as demonstrated in equation 2.44 for the fluid domain.

Taking a closer look at what we have done, we can see that:

$$\oiint_{A_f} W_i \left[\frac{1}{Re_\infty Pr_\infty (\gamma_\infty - 1)M_\infty^2} \left(\kappa_{eff} \frac{\partial T}{\partial x_i} \right) \right] dS = \oiint_{A_s} W_i \left[\frac{1}{Re_\infty Pr_\infty (\gamma_\infty - 1)M_\infty^2} \left(\kappa_s \frac{\partial T}{\partial x_i} \right) \right] dS \qquad (3.8)$$

Replacing the temperature gradient terms by the heat flux in the surface integrals we get:

$$\oiint_{A_f} W_i \left[\frac{1}{Re_\infty Pr_\infty (\gamma_\infty - 1)M_\infty^2} q_f \right] dS = \oiint_{A_s} W_i \left[\frac{1}{Re_\infty Pr_\infty (\gamma_\infty - 1)M_\infty^2} q_s \right] dS \qquad (3.9)$$

Removing the non-dimensionalization terms for clarity, we get:

$$\oiint_{A_f} W_i q_f dS = \oiint_{A_s} W_i q_s dS \qquad (3.10)$$

Thus, redistributing the dead fluid energy equation residual terms to the live solid nodes at the interface ensures that the heat flux across the interface is area-conserved if done consistently. The solution at the interface advances at each iteration where the temperature is the variable being solved in the solid domain, but the heat fluxes across the interface are forced to be identical due to the implicit treatment of the calculation. Therefore, the proposed method for the interface treatment is to redistribute the fluid matrix terms using a non-conservative approach at the element level, but to redistribute the fluid residuals at the end of the assembly by breaking them down to heat fluxes beforehand and reconstructing the corresponding solid residual terms as a second step. The methodology used to ensure that the heat flux contributions are area-conservative will be described in the next section through the use of a master grid concept. The master grid at the CHT interface is generated by splitting all edges between the fluid faces and the solid faces to create a triangular grid where both the fluid grid and solid grid are subsets of the master grid.

The CHT algorithm can be described as follows:

A. During the assembly for a live element (fluid or solid elements):
   1. Create the local energy matrix terms and the local energy residual terms.
   2. Create the local heat flux matrix terms and the local heat flux right-hand-side terms.
   3. Assemble the local energy matrix terms and the local energy residual terms into the global energy matrix and the global energy residual vector according to the element connectivity.
   4. Assemble the local heat flux matrix terms and the local heat flux right-hand-side into the global heat flux matrix and the global heat flux right-hand-side vector according to the element connectivity.

B. During the assembly for a dead element (fluid elements only):

   1. Create the local energy matrix terms and the local energy residual terms.
   2. Create the local heat flux matrix terms and the local heat flux right-hand-side terms.
   3. Assemble the local energy matrix terms into the global energy matrix. For the live nodes, use the element connectivity. For the dead nodes at the interface, redistribute the terms to the live nodes using the shape functions of the live elements. Assemble the local energy residual terms in the global energy residual vector only for the live nodes using the element connectivity.
   4. Assemble the local heat flux matrix terms and the local heat flux right-hand-side into the global heat flux matrix and the global heat flux right-hand-side vector according to the element connectivity.

C. After the assembly:

   1. Solve for the heat fluxes for the fluid domain.
   2. Map the fluid heat fluxes at the interface from the dead nodes to the master grid nodes.
   3. Assemble the "delta" residual contributions of the dead nodes to the live nodes by recreating the right-hand-side surface integral of equation 3.9 for all the master grid faces in the live elements faces. Redistribute the contributions into the live nodes by using the weight of the shape function in the live element (to be explained in the next section).

4. Solve the energy equation using a direct or iterative solver.
5. Update the temperature variable for all the live nodes in the usual manner. For the dead nodes, update the temperature by interpolating the temperatures of the live nodes in the live element face where the dead nodes are found.

The method is consistent and general to handle any type of grid mismatch and any type of linear elements on both sides of the CHT interface with relevant ease. The solution is as accurate as the fluid and solid grids discretization accuracy since there is minimal discretization error involved in the coupling algorithm.

The non-matching grid handling for the residuals (heat fluxes) is achieved through the use of a virtual grid (master grid) concept developed by Lepage. [28, 29] Figure 3.2 shows the fluid and solid grids for a square region at the CHT interface. The coarseness of the grids is intended for visualization purposes. Usually, the fluid mesh is much finer than the solid grid. [29]

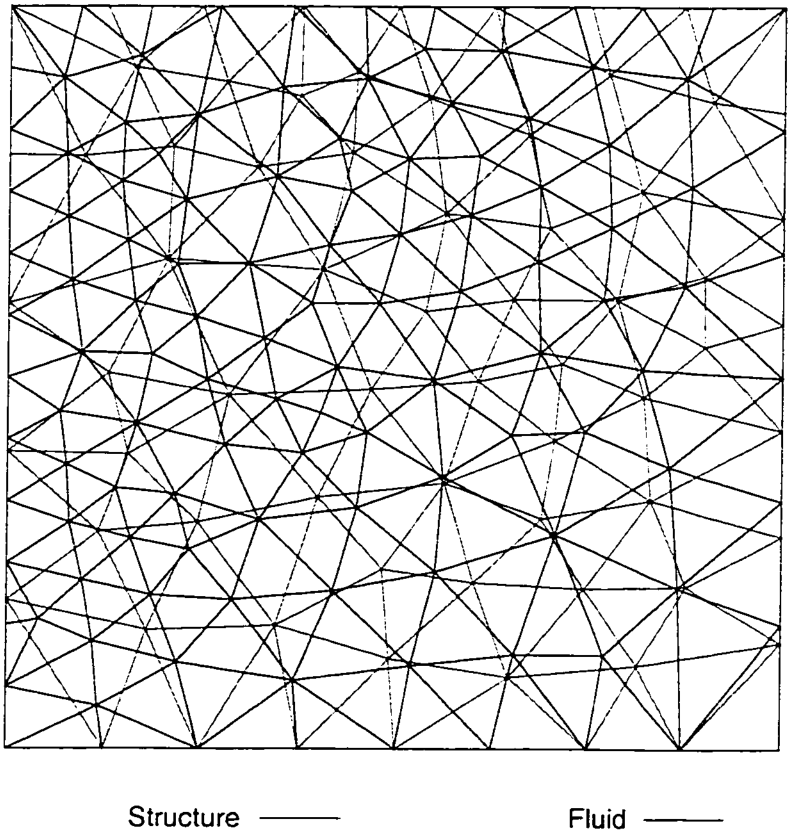

Figure 3.2: Fluid and Solid Grids at the CHT Interface [29]

The virtual grid is generated by splitting all edges between the fluid faces and solid faces to create a 2D triangular grid where the square symbols identify the solid nodes and the triangle symbols identify the fluid nodes, as shown in figure 3.3. The virtual grid is built in such a way that all the nodes and edges of both the solid and fluid grids appear as nodes and edges on the virtual grid; some additional nodes (and corresponding edges) also appear in the virtual grid in order to allow the construction of a 2D triangular grid, as shown in figure 3.3. [29]

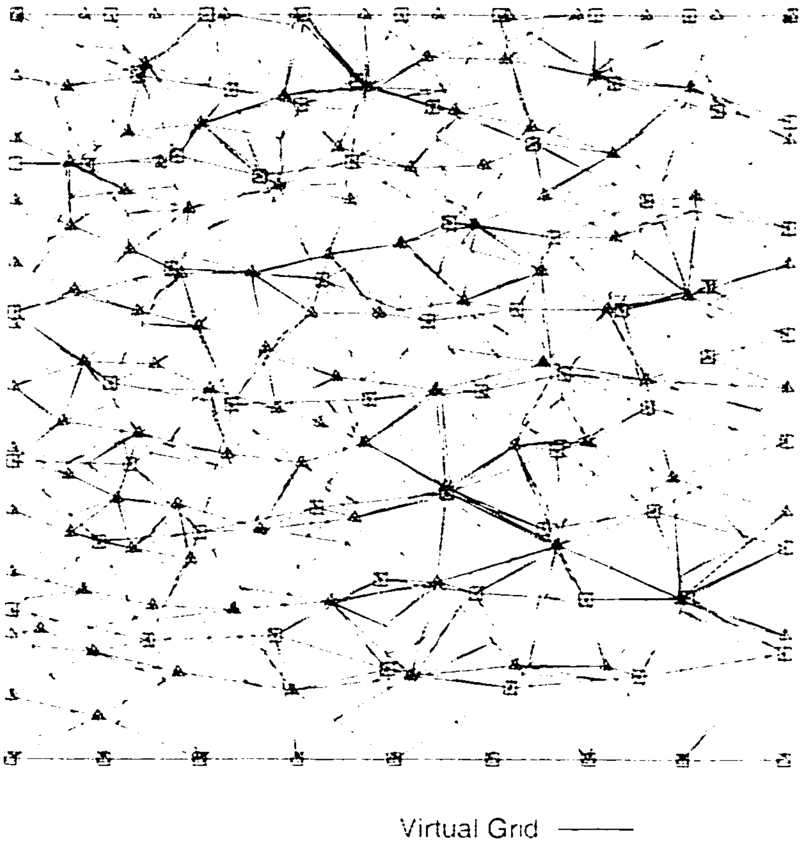

Figure 3.3: Virtual Grid at the CHT Interface [29]

The virtual grid contains both the fluid and the solid grids at the interface. They are subsets of this master grid. The poor appearance of the virtual grid, caused by the thin skewed elements, is purely of cosmetic concern. All elements are used for the interpolation process only and not during the solution process of the CFD code. [29]

The temperatures, defined at the nodes of the solid grid, are transferred to the matching nodes on the virtual grid. The temperatures at the other nodes of the virtual grid are obtained using linear interpolation over the triangular faces of the virtual grid and are transferred directly to the nodes of the fluid grid at the end of the energy equation iteration.

Now, from equation 3.10 we want to recreate the surface integral at the end of the assembly procedure:

$$\oiint_{A_s} W_i q_s dS \tag{3.11}$$

by using the nodal heat flux values coming from the fluid grid at the interface. This will close the energy equation system. The nodal heat fluxes are transferred to the matching nodes on the virtual grid. The heat fluxes at the other nodes of the virtual grid are obtained using linear interpolation over the triangular faces of the virtual grid. Computing the surface integral in equation 3.11 directly over the solid face by using the heat fluxes at the solid nodes would not respect the heat balance across the CHT interface as required by equation 3.10. The method would be non-conservative for the heat balance. Instead, the evaluation of the surface integral is broken down as:

$$\oiint_{A^{(s)}} W_i q_s dS = \sum_{v \subset S} \oiint_{A^{(v)}} W_i q_f^{(v)} dS \tag{3.12}$$

as illustrated in figure 3.4. The solid face is made up of eleven virtual faces.

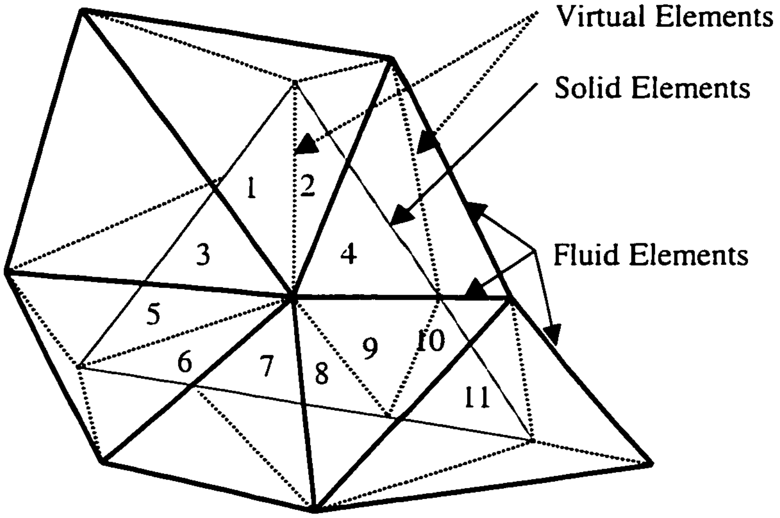

Figure 3.4: Evaluation of a Surface Integral on the Virtual Grid [29]

Each face of the virtual grid is totally contained within the face of the fluid grid and a face of the solid grid. With this geometric decomposition, it is possible to integrate the heat fluxes exactly over each face of the virtual grid and satisfy the desired conservation properties, both locally and globally. [29] In our case, these are the residual contributions.

The integrals are evaluated using Gauss-Legendre integration, such as for q:

$$\oiint_{A^{(v)}} \overline{W}_i q_f^{(v)} dS = \sum_{k=1}^{ngaus} q_f^{(v)}(\varepsilon_k, \eta_k) \overline{W}_i(\bar{\varepsilon}_k, \bar{\eta}_k) |J_k| \omega_k \tag{3.13}$$

where, $$\bar{\xi}_k = \sum_j N_j(\xi_k, \eta_k) \bar{\xi}_j \tag{3.14}$$

and, $$\bar{\eta}_k = \sum_j N_j(\xi_k, \eta_k) \bar{\eta}_j \tag{3.15}$$

with $(\bar{\xi}_i,\bar{\eta}_i)$ being the local coordinates of the nodes of the virtual face $A^{(v)}$ in terms of the local coordinates system of the solid face $A^{(s)}$, and N_j and $\overline{N}_j$ are the shape functions for the virtual face $A^{(v)}$ and solid face $A^{(s)}$, as shown in figure 3.5. Since Gresho's heat fluxes are node based, a 3-4 Gauss point integration is needed over the triangular faces to exactly calculate the contribution of the heat fluxes on the virtual face $A^{(v)}$ to each node of the solid face $A^{(s)}$.

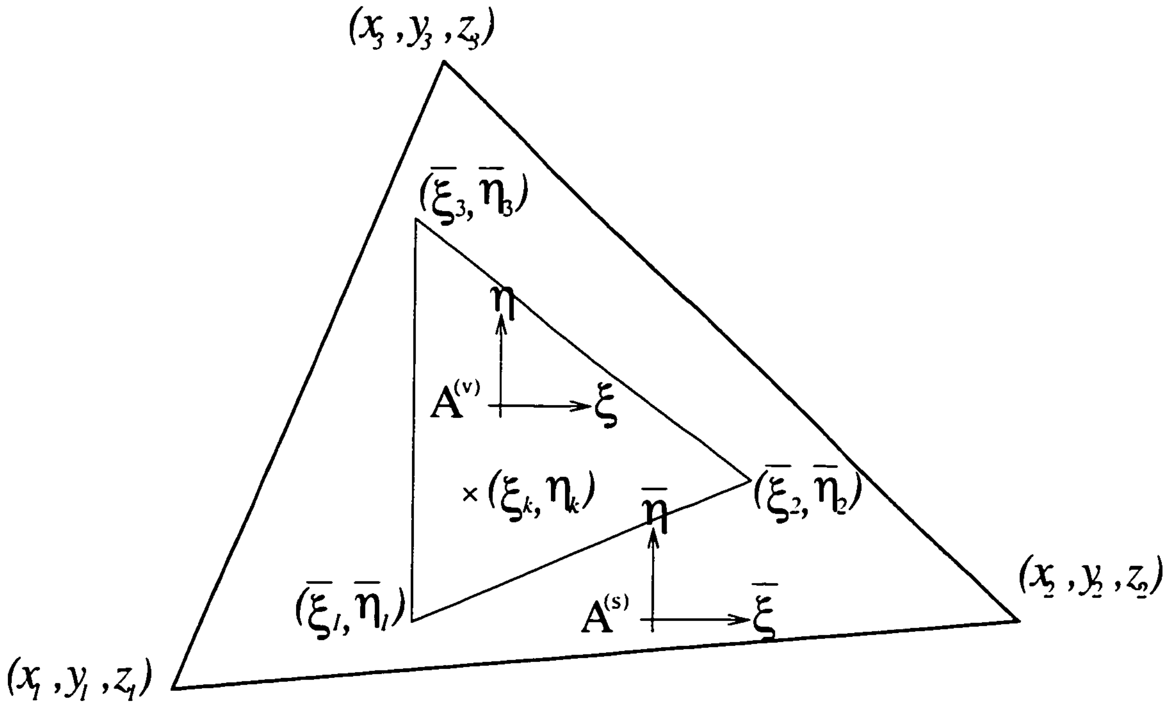

Figure 3.5: Local Coordinates Systems for $A^{(v)}$ and $A^{(s)}$ [29]

4. Heat Transfer Validation of FENSAP

4.1. Introduction

The CFD Lab is active in the field of aircraft icing prediction. Before undergoing any CHT implementation and validation to deal with anti-icing problems, some baseline heat transfer validation must be conducted. The heat transfer validation of FENSAP for both laminar and turbulent flow is conducted in this thesis through a series of 2D test cases with special interest to fluid flow that applies in the aircraft industry. For each test case, the results are compared to available empirical correlations and/or numerical/experimental results from the open literature when available. The 2D test cases are simulated in FENSAP with two planes in the z-direction since FENSAP is a 3D code. One plane imposes a symmetry condition, while the other plane imposes a periodic condition.

For the laminar test cases, grid sensitivity studies were performed through anisotropic mesh adaptation using OptiMesh^{TM}. For the turbulent test cases, a couple of refined grids were created to verify the near-wall grid spacing for proper turbulence modeling. Only the results from the best grid are presented, unless stated otherwise. Each test case was initialized with freestream conditions. The simulations were performed until the absolute combined residuals for the continuity, momentum and energy equations was below a value of 10^{-8} or, that this maximum normalized residual was reduced by 3 orders of magnitude (10^{-3}).

4.2. Laminar Flow

During the course of this thesis work, FENSAP has changed formulations for the energy equation from a conservative form for total enthalpy to a non-conservative form for static temperature. Heat transfer validation was needed for the laminar flow regime since there is no modeling assumption for the temperature profile, i.e. the shape function uses a linear element in the first element on the wall. The validation was conducted with the following two test cases:

1. 2D Flat Plate
2. 2D NACA0012 Aerofoil

The flat plate test case should have been run with the incompressible assumption but since FENSAP is a compressible code this can only be achieved by running with a low Mach number, say around 0.10 in most test cases. Thus, the condition of zero-divergence flow is not necessarily imposed but the error involved is minimal.

4.2.1. 2D Flat Plate

4.2.1.1. Introduction

The flow being modeled is the incompressible laminar flow over a smooth flat plate. The local Nusselt number distribution along the plate can be compared with that of the well-known correlation of Eckert [30].

4.2.1.2. Problem Definition

The geometry for the flat plate is shown in figure 4.1 and has been non-dimensionalized for a flat plate of length L. The inlet is placed 1-L upstream of the plate leading edge. A symmetry condition is imposed upstream of the plate while the far-field boundary condition, 2.5-L above the plate, was fixed at free stream values. The exit is downstream of the plate.

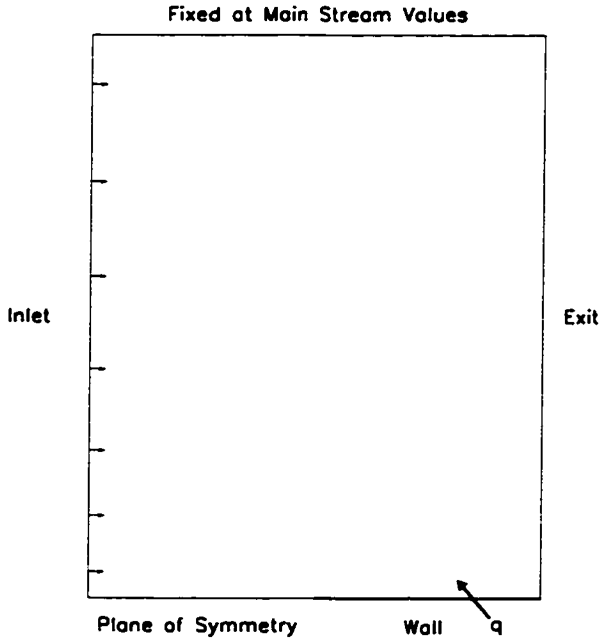

Figure 4.1: Computational Domain for the Laminar Flow over a Flat Plate

4.2.1.3. Boundary Conditions

The boundary conditions for the flow analysis are as follows:

Inlet: Mach Number, $M_\infty = 0.10$

Static Temperature, $T_\infty = 288$ K

Reynolds Number, $Re_L = 1{,}000$

Exit: Static Pressure, $p_\infty = 101.325$ kPa

Plate: Wall Temperature, $T_w = 293$ K

The inlet velocity profile was uniform at the inlet. The Reynolds number is based on the freestream conditions and the plate length, as follows:

$$Re_L = \frac{\rho_\infty U_\infty L}{\mu_\infty} \tag{4.1}$$

4.2.1.4. Computational Grid

The test case used an unstructured grid. Through anisotropic mesh adaptation, the best grid was obtained for a specified target number of nodes. The variable used for the adaptation error estimation was the Mach number. The final grid has 2,748 nodes, as shown in figure 4.2 with a close-up view in figure 4.3. The initial grid was not available for comparison since the adapted grid was not generated in the course of this thesis. Notice how the mesh adaptation clustered the grid points near the leading edge of the plate, as shown in figure 4.3, to resolve the flow gradients.

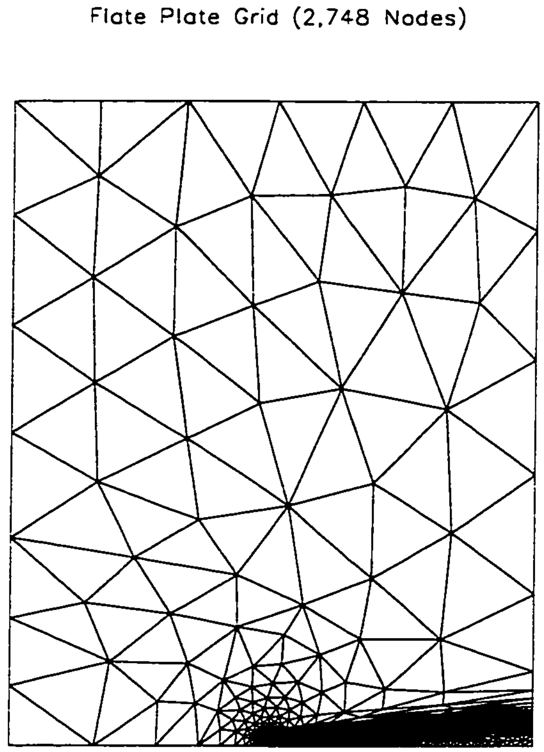

Figure 4.2: Grid for the Laminar Flow over a Flat Plate

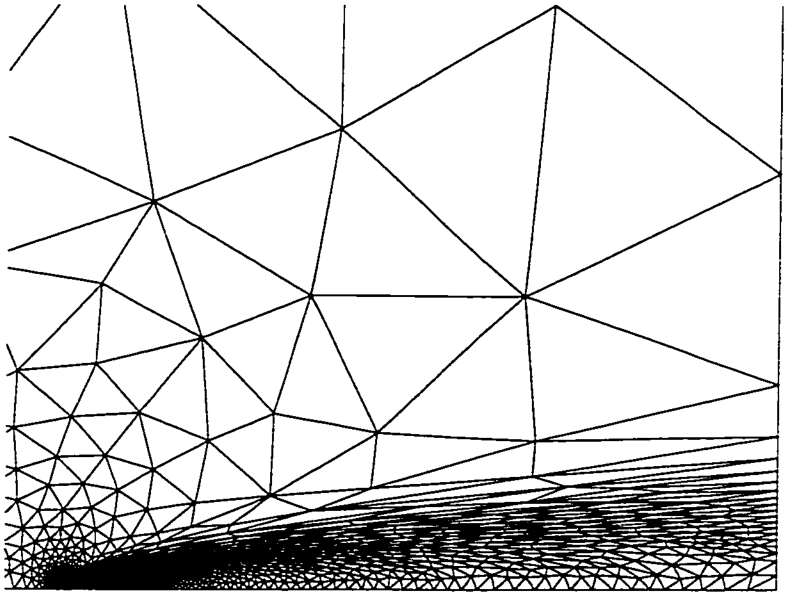

Figure 4.3: Grid for the Laminar Flow over a Flat Plate (close-up)

4.2.1.5. Results & Discussion

The convergence of this test case is shown in figure 4.4. To prove the robustness of FENSAP, the test case was started from no initial solution on the adapted grid with 3 cycles of artificial dissipation since the adapted grid had very skewed elements. The final cycle exceeded the residual reduction of 3 orders of magnitude and, converged to an absolute value of 10^{-8}.

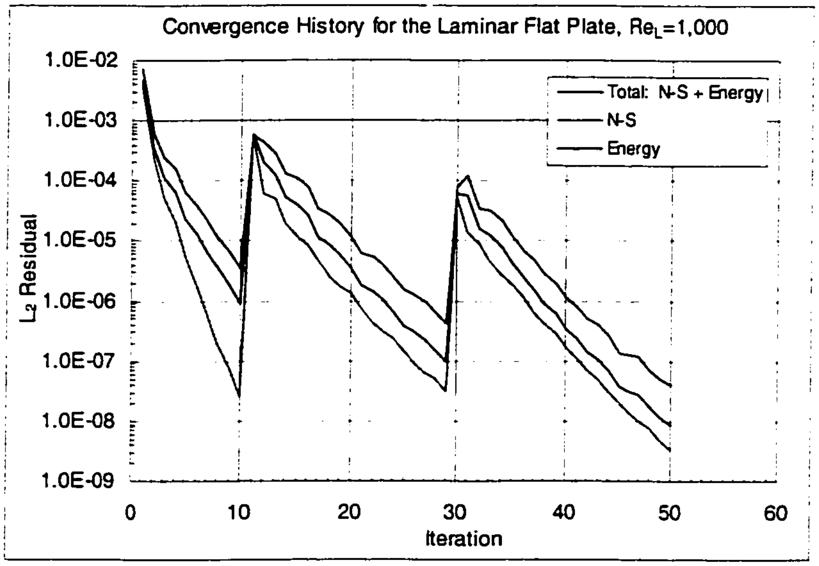

Figure 4.4: Convergence History for the Laminar Flow over a Flat Plate

The Mach number and static temperature along the flat plate are shown in figures 4.5 and 4.6, respectively. From figure 4.3 it can be seen that the grid is aligned with the Mach number and static temperature field.

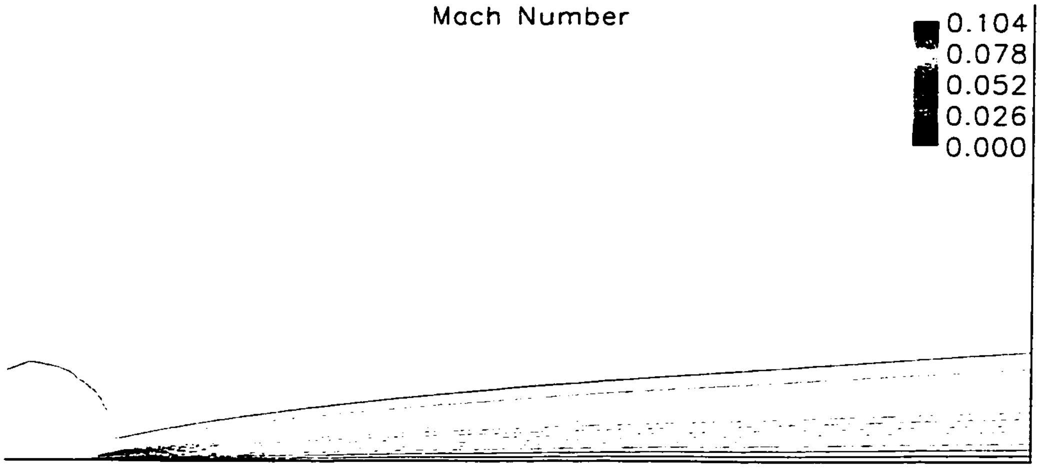

Figure 4.5: Mach Number Distribution along the Plate

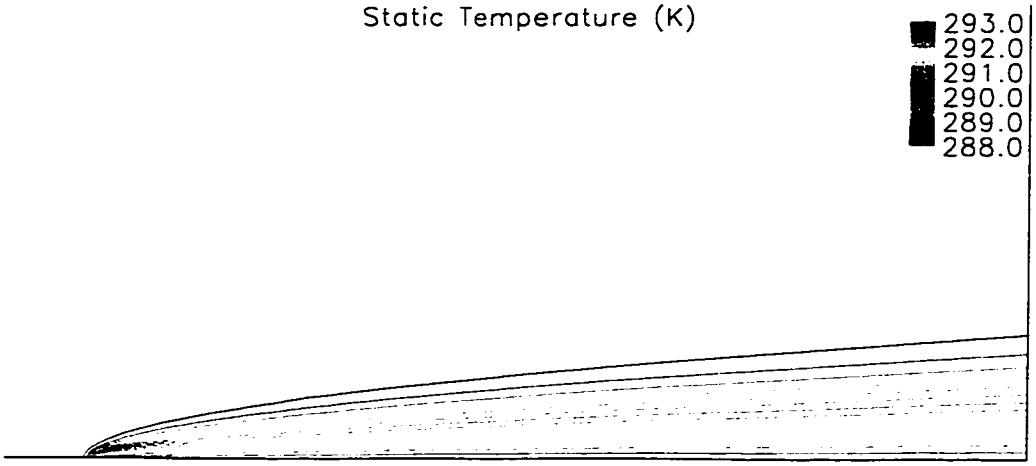

Figure 4.6: Static Temperature Distribution along the Plate

To evaluate the accuracy of the heat transfer prediction, the computed local Nusselt number is compared with that of the well-known correlation of Eckert [30]. The local Nusselt number is defined as:

$$Nu = \frac{qL}{k(T_w - T_{aw})} \qquad (4.2)$$

where q is the heat flux, L is the plate length, T_w is the wall temperature, T_{aw} is the adiabatic wall temperature, and k is the thermal conductivity of the air. The analytical Nusselt number is given by [30]:

$$Nu = 0.333\sqrt[3]{Pr}\sqrt{Re_x}\,\frac{L}{x} \tag{4.3}$$

The results of this comparison are shown in figure 4.6. The computed and analytical results are nearly identical, where the computed Nusselt number at the end of the plate under-predicts from the analytical value by only 0.6%.

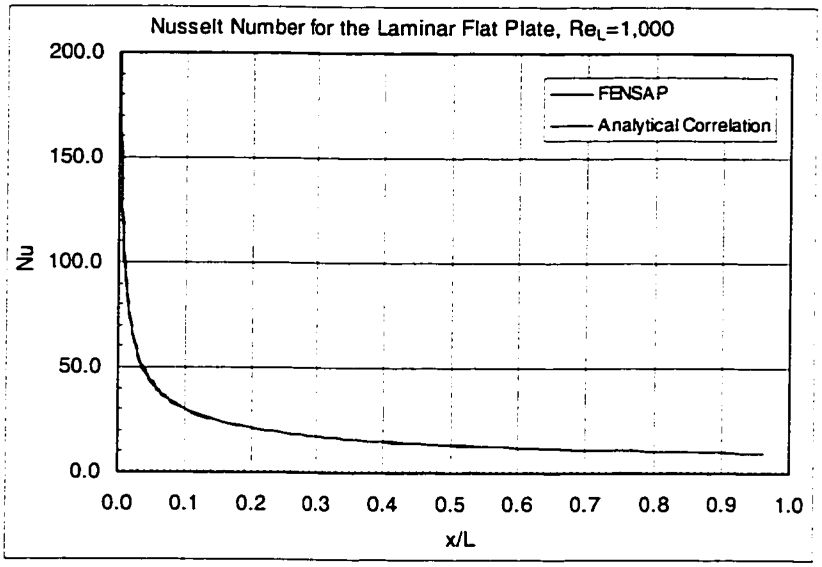

Figure 4.7: Nusselt Number for the Laminar Flow over a Flat Plate

4.2.2. 2D NACA0012 Aerofoil

4.2.2.1. Introduction

The flow being modeled is the compressible laminar flow over a NACA0012 aerofoil at 10-degrees angle of attack. This test case was proposed by Dadone for the different research units in Italian universities. [31] The local heat transfer coefficient distribution along the aerofoil is compared with the computational results from Dadone & De Palma. [32]

4.2.2.2. Problem Definition

The geometry for the aerofoil is shown in figure 4.8 and the geometry has been non-dimensionalized for an aerofoil chord of length c. The inlet is placed 4-c upstream of the aerofoil leading edge, while the exit is placed 6-c downstream of the aerofoil trailing edge. The far-field boundary condition, 7-c above and below the aerofoil, was fixed at free stream values.

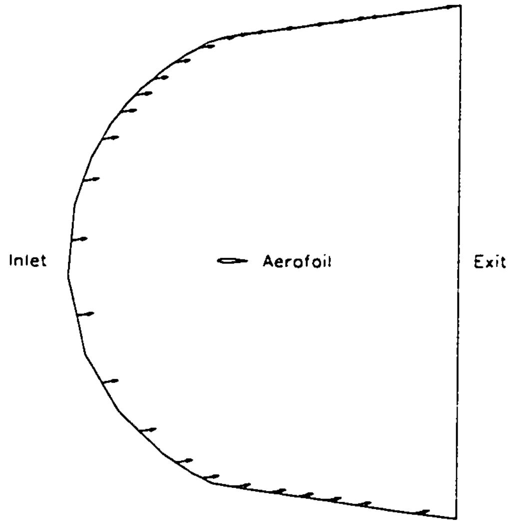

Figure 4.8: Computational Domain for the Laminar Flow over a NACA0012 Aerofoil

4.2.2.3. Boundary Conditions

The boundary conditions for the flow analysis are as follows:

Inlet:	Mach Number, $M_\infty = 0.80$
	Static Temperature, $T_\infty = 288$ K
	Reynolds Number, $Re_c = 500$
Exit:	Static Pressure, $p_\infty = 100.0$ kPa
Aerofoil:	Wall Temperature, $T_w = 324.864$ K

The inlet velocity profile was uniform at the inlet and angled at 10-degrees angle of attack. The wall temperature on the aerofoil was set to the inlet total temperature. The Reynolds number is based on the free stream conditions and the chord, as follows:

$$Re_c = \frac{\rho_\infty U_\infty c}{\mu_\infty} \tag{4.4}$$

4.2.2.4. Computational Grid

The test case used an unstructured grid. Through anisotropic mesh adaptation, the best grid was obtained for a specified target number of nodes. The variable used for the adaptation error estimation was the Mach number. The initial grid had 13,342 nodes, as shown in figure 4.9, while the final adapted grid had 14,896 nodes, as shown in figure 4.10 with a close-up view in figure 4.11. Notice how the mesh adaptation clustered the grid points near the leading edge of the aerofoil and at the wake after the trailing edge of the aerofoil, as shown in figure 4.11, to resolve the flow gradients.

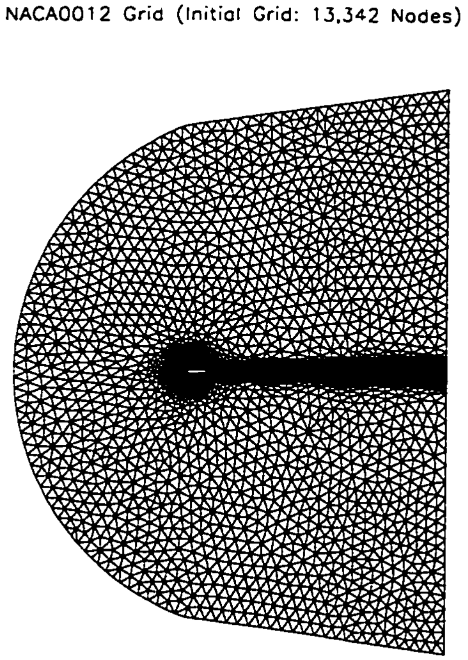

Figure 4.9: Initial Grid for the Laminar Flow over a NACA0012 Aerofoil

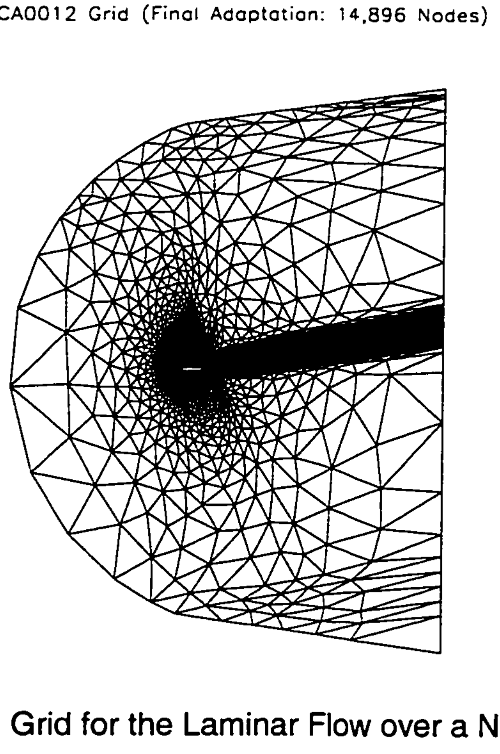

Figure 4.10: Adapted Grid for the Laminar Flow over a NACA0012 Aerofoil

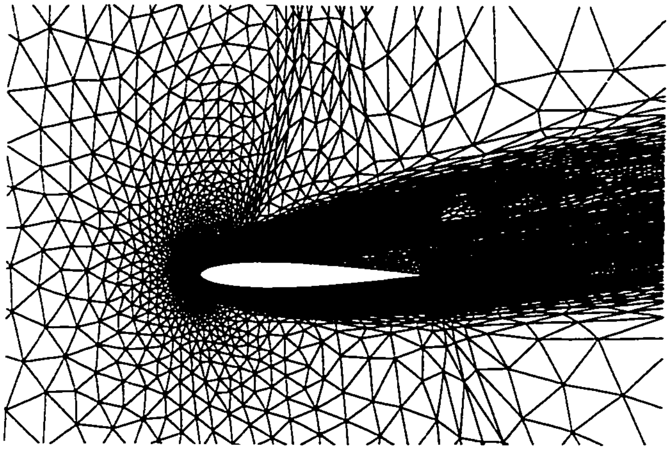

Figure 4.11: Adapted Grid for the Laminar Flow over a NACA0012 Aerofoil (close-up)

4.2.2.5. Results & Discussion

The convergence of this test case is shown in figure 4.12. To prove the robustness of FENSAP, the test case was started from no initial solution with 3 cycles of artificial dissipation since the adapted grid had very skewed elements. The final cycle exceeded the residual reduction of 3 orders of magnitude, and converged to an absolute value of 10^{-8}.

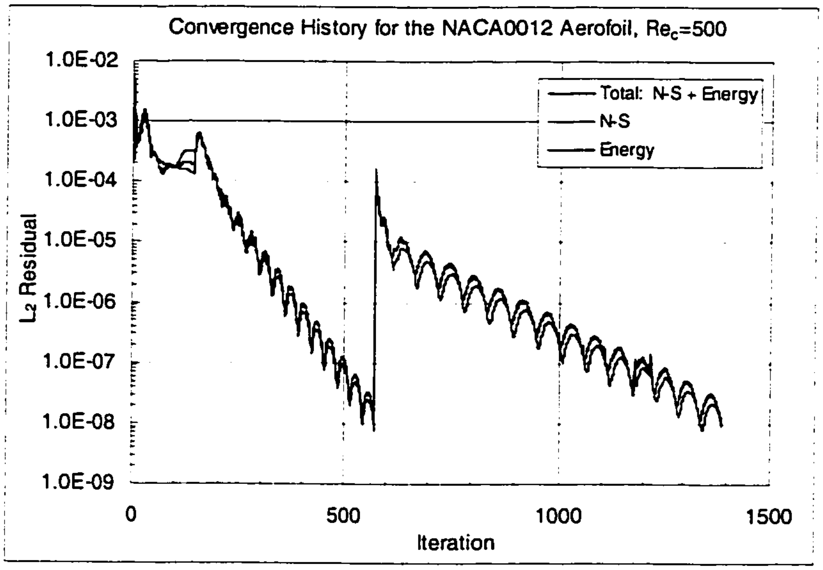

Figure 4.12: Convergence History for the Laminar flow over a NACA0012 Aerofoil

The Mach number and static temperature along the aerofoil are shown in figures 4.13 and 4.14, respectively. From figure 4.11 we can see that the grid at the trailing edge wake is aligned with the Mach number and static temperature field.

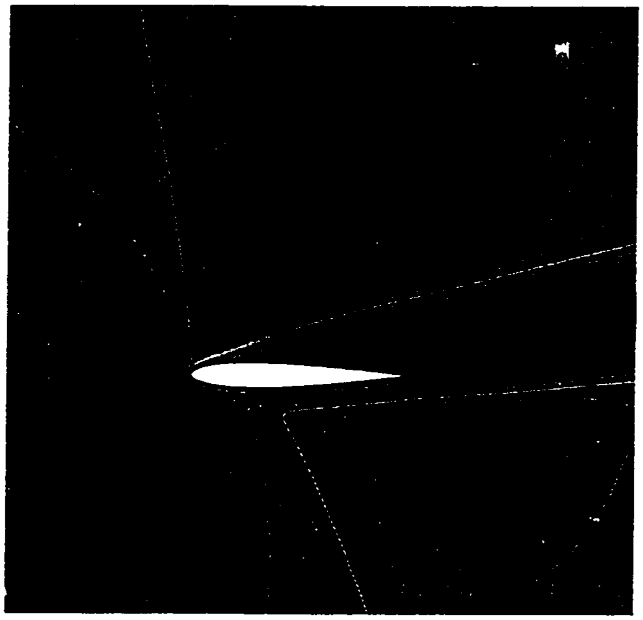

Figure 4.13: Mach Number Distribution along the Aerofoil

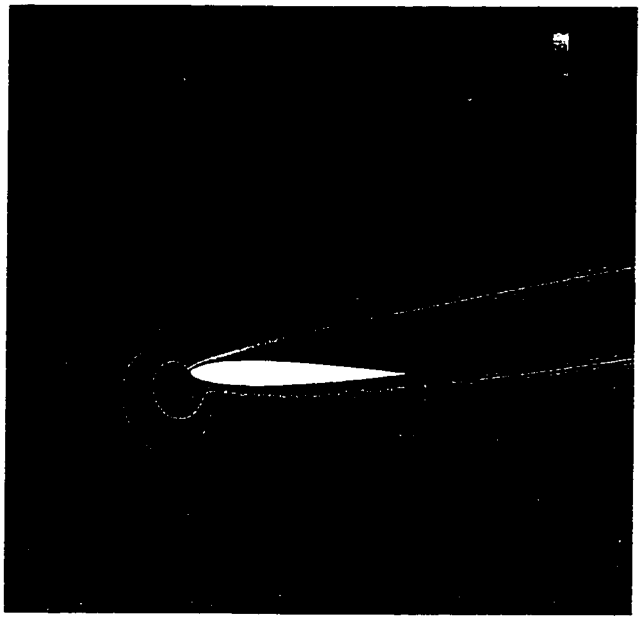

Figure 4.14: Static Temperature Distribution along Aerofoil

To evaluate the accuracy of the heat transfer prediction, the computed local heat transfer coefficient is compared with that computed by Dadone & De Palma. [32] The local heat transfer coefficient is defined as:

$$C_h = \frac{2q}{\rho_\infty U_\infty^3} \tag{4.5}$$

where q is the heat flux, ρ_∞ is freestream air density and, U_∞ is the air freestream velocity.

The results of this comparison are shown in figure 4.15 and the agreement is quite evident. Some of the differences are attributed to the fact that FENSAP is a FEM code, while Dadone & De Palma's is a FVM code, and both CFD codes use a different artificial dissipation scheme. Also, the results from Dadone & De Palma come from a body-fitted structured grid with clustering around the whole aerofoil while the results from FENSAP use anisotropic mesh adaptation to obtain the "converged" grid.

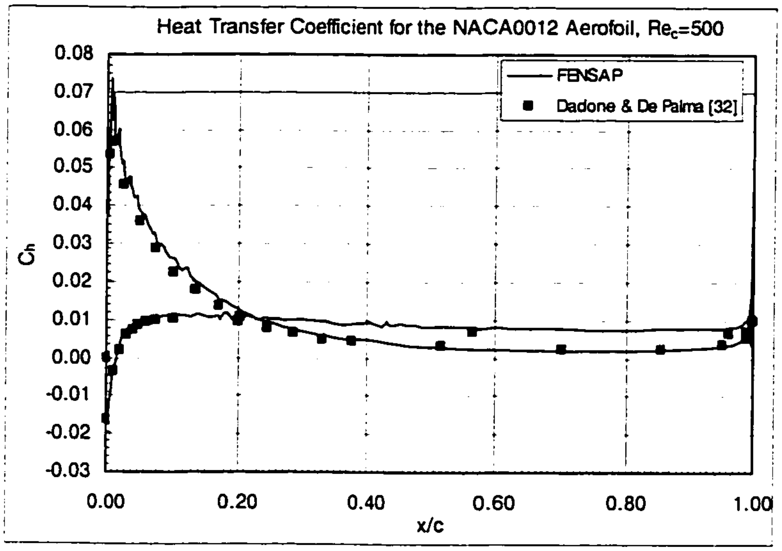

Figure 4.15: Heat Transfer Coefficient for the Laminar Flow over a NACA0012 Aerofoil

4.3. Turbulent Flow

Heat transfer validation was needed for the turbulent flow regime since FENSAP uses wall shape functions in the first element on the wall to integrate the velocity, temperature and, turbulent viscosity profiles, while using a high-Reynolds number $\kappa-\varepsilon$ turbulence model, as detailed in chapter 2. Some extra damping coefficients are added to the turbulence model for stability and to capture some of the low-Reynolds number effects.

To assess the accuracy of the turbulence modeling for heat transfer in FENSAP, the following three test cases, as proposed by Heyerichs and Pollard, were tested [33]:

1. 2D Flat Plate (high-Reynolds number flow)
2. 2D Backward Facing Step (low-Reynolds number flow)
3. 2D Impinging Jet (low-Reynolds number flow)

The test cases should have been run with the incompressible assumption, but since FENSAP is a compressible code this can only be achieved by running with a low Mach number, say around 0.10 in most test cases. Thus, the condition of zero-divergence flow is not necessarily imposed but the error involved is minimal.

4.3.1. 2D Flat Plate

4.3.1.1. Introduction

The flow being modeled is the incompressible turbulent flow over a smooth flat plate. This test case evaluates the modeling assumptions for boundary layer flows. The local Nusselt number distribution along the plate is compared with the correlation presented by Schlicting [30]. Velocity and turbulent kinetic energy profiles are compared to the experimental data of Klebanoff found in Jones & Launder. [34, 17]

4.3.1.2. Problem Definition

The geometry for the flat plate is shown in figure 4.16 and has been non-dimensionalized for a flat plate of length L.

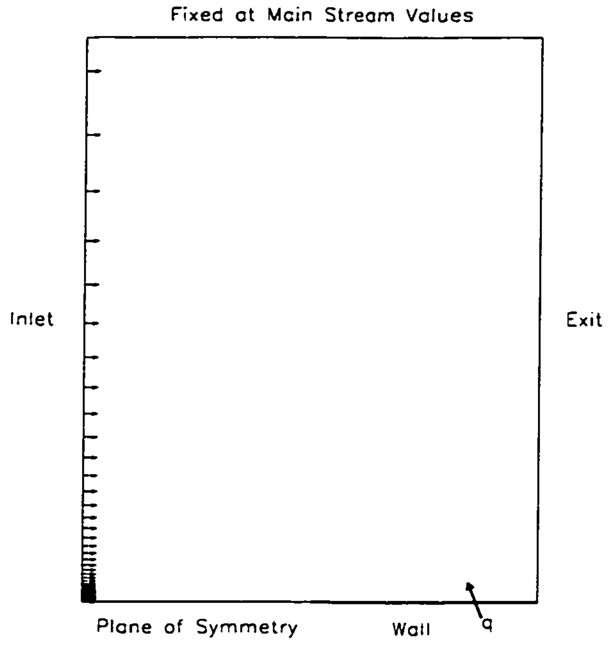

Figure 4.16: Computational Domain for the Turbulent Flow over a Flat Plate

The inlet is placed 1-L upstream of the plate leading edge. A symmetry condition is imposed upstream of the plate, while the far-field boundary condition, 2.5-L above the plate was fixed at free stream values. The exit is downstream of the plate.

4.3.1.3. Boundary Conditions

The boundary conditions for the flow analysis are as follows:

Inlet: Mach Number, $M_\infty = 0.044$
Static Temperature, $T_\infty = 288$ K
Reynolds Number, $Re_L = 4.2\text{x}10^6$
Turbulence Intensity, $i_\infty = 0.04\%$
Turbulent Viscosity Ratio, $\mu_{t\infty} / \mu_{l\infty} = 1.0$
Exit: Static Pressure, $p_\infty = 101.325$ kPa
Plate: Wall Temperature, $T_w = 293$ K

The inlet velocity profile was uniform at the inlet. The Reynolds number is based on the freestream conditions and the plate length, as follows:

$$Re_L = \frac{\rho_\infty U_\infty L}{\mu_\infty} \tag{4.6}$$

The Reynolds number for this test case corresponds closely to the experimental data of Klebanoff found in Jones & Launder. [34, 17] The Mach number was deduced from ambient conditions to respect the experimental plate length. The wall temperature was set not too high from the free stream temperatures since the original test (for the flow field data) was probably run for an adiabatic wall.

4.3.1.4. Computational Grid

The test case used a structured hexahedral grid with 126 nodes in the axial direction, 51 nodes in the normal direction, and 2 nodes in the z-direction, thus the grid had 12,852 nodes. The grid was clustered in the normal direction to the wall to resolve the boundary layer and was also packed in the streamwise direction near the leading edge of the plate to resolve the flow gradients there, as shown in figure 4.17.

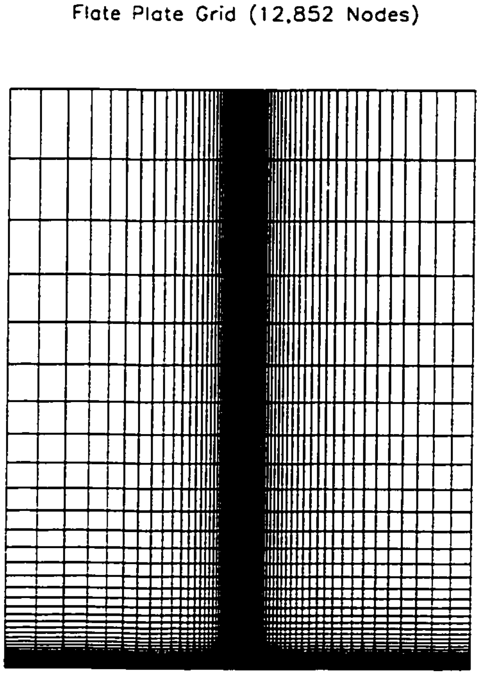

Figure 4.17: Grid for the Turbulent Flow over a Flat Plate

To verify the influence of the first element height normal to the wall, a series of four grids were generated with four different grid spacing for the height of the first element off the wall. This provided a y^+ study for this test case. The grid details are reported in non-dimensional form, y_p/L, as listed in table 4.1.

	y_p/L	Average y^+
Grid 1	0.00005	10
Grid 2	0.00015	28
Grid 3	0.00025	42
Grid 4	0.00050	88

Table 4.1: Grid Sensitivity Study for the Turbulent Flow over a Flat Plate

4.3.1.5. Results & Discussion

The convergence of this test case is shown in figure 4.18, only for grid 3. The other grids converged to the same residual levels but with a different number of iterations. The test case was started from no initial solution with 3 cycles of artificial dissipation. The final cycle exceeded the residual reduction of 3 orders of magnitude, and converged to an absolute value of 10^{-9}.

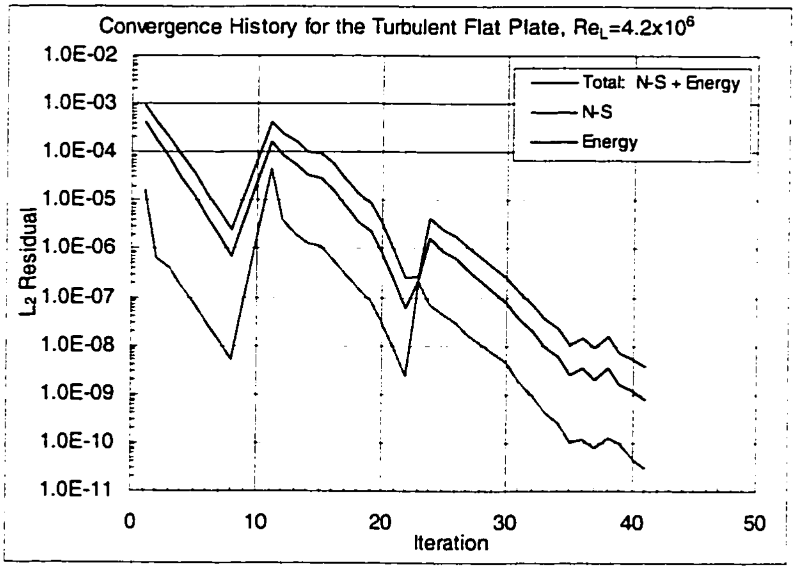

Figure 4.18: Convergence History for the Turbulent Flow over a Flat Plate

The Mach number and static temperature along the flat plate are shown in figures 4.19 and 4.20, respectively. Notice the thin boundary layer since the Reynolds number is of the order of 10^6.

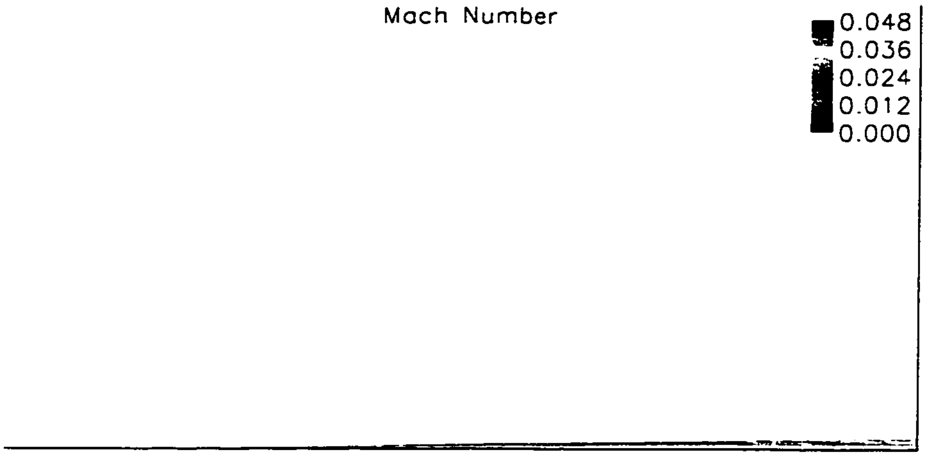

Figure 4.19: Mach Number Distribution along the Plate

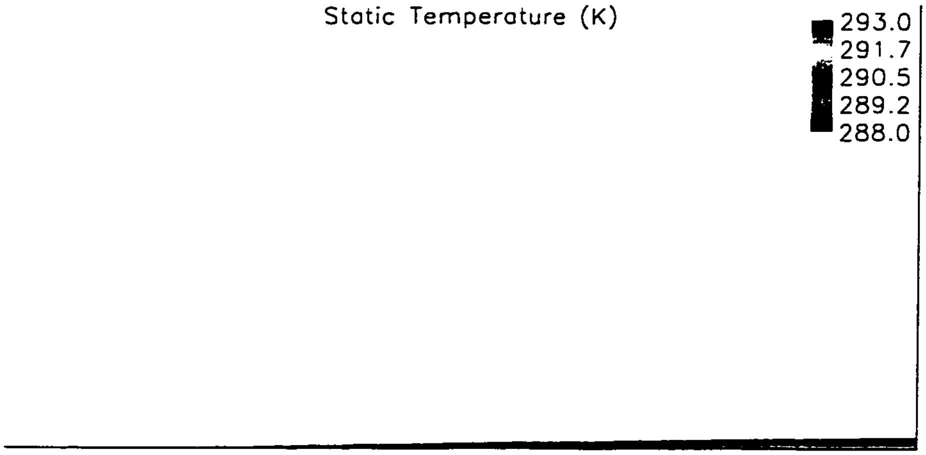

Figure 4.20: Static Temperature Distribution along the Plate

The profiles of turbulence kinetic energy and of mean velocity normal to the plate at x = L are compared to the data of Klebanoff as shown in figures 4.21 and 4.22, respectively. [34] The agreement is quite evident for grids 2, 3, and 4 since the turbulence at the wall is correctly set off, i.e. the y^+ values are in a valid range for the $\kappa-\varepsilon$ Dirichlet boundary conditions. The turbulence kinetic energy is over-predicted, while the mean velocity profile is under-predicted for grid 1.

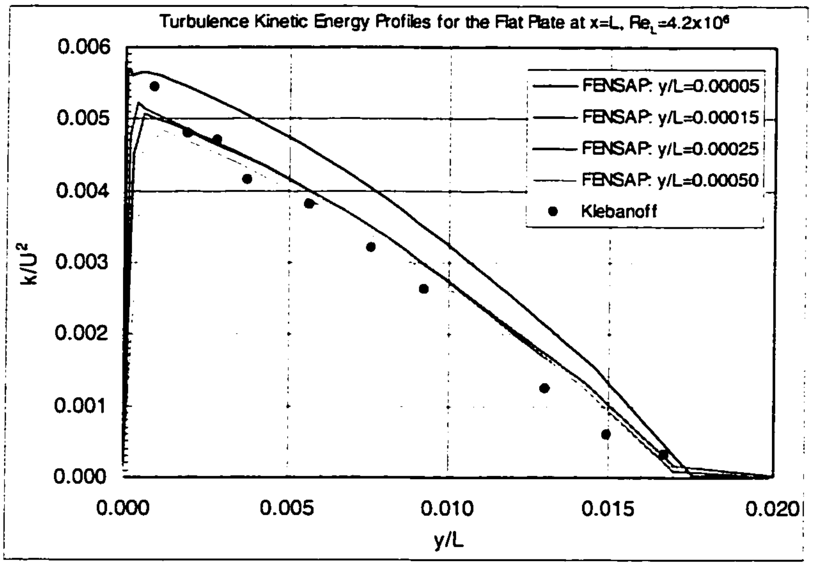

Figure 4.21: Turbulent Kinetic Energy Profiles for the Turbulent Flow over a Flat Plate

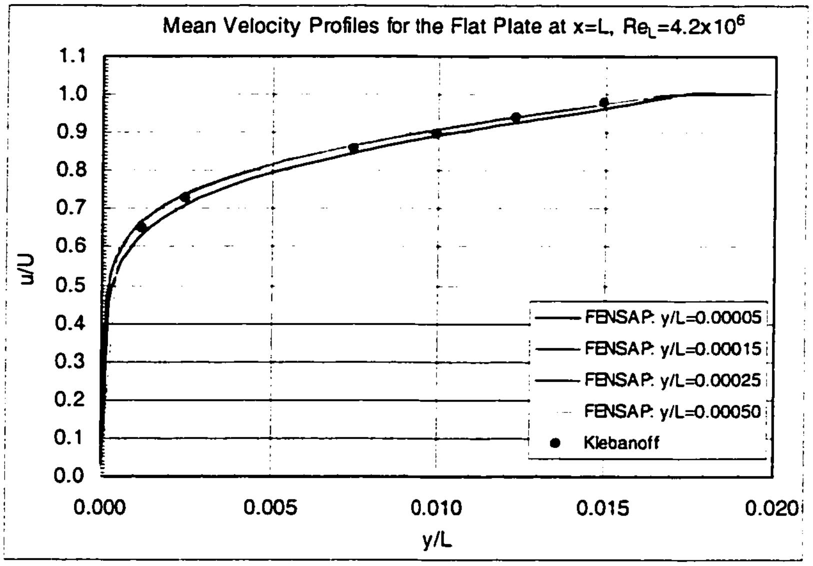

Figure 4.22: Mean Velocity Profiles for the Turbulent Flow over a Flat Plate

To evaluate the accuracy of the heat transfer prediction, the computed local Nusselt number distribution along the plate is compared with the correlation presented by Schlichting [30]. The local Nusselt number is defined as:

$$Nu = \frac{qL}{k(T_w - T_{aw})} \qquad (4.7)$$

where q is the heat flux, L is the plate length, T_w is the wall temperature, T_{aw} is the adiabatic wall temperature, and k is the thermal conductivity of the air. The empirical Nusselt number is given by [30]:

$$Nu = 0.0296\,Pr^{1/3}\,Re_x^{4/5}\,\frac{L}{x} \qquad (4.8)$$

The results of this comparison are shown in figure 4.23. The computed and empirical results are nearly identical for grids 2, 3, and 4. This is not the case for grid 1 where it clearly over-predicts the heat transfer on the wall. Since the turbulence kinetic energy is over-predicted next to the wall for this grid, then the convective heat transfer is over-predicted, as shown in figure 4.23.

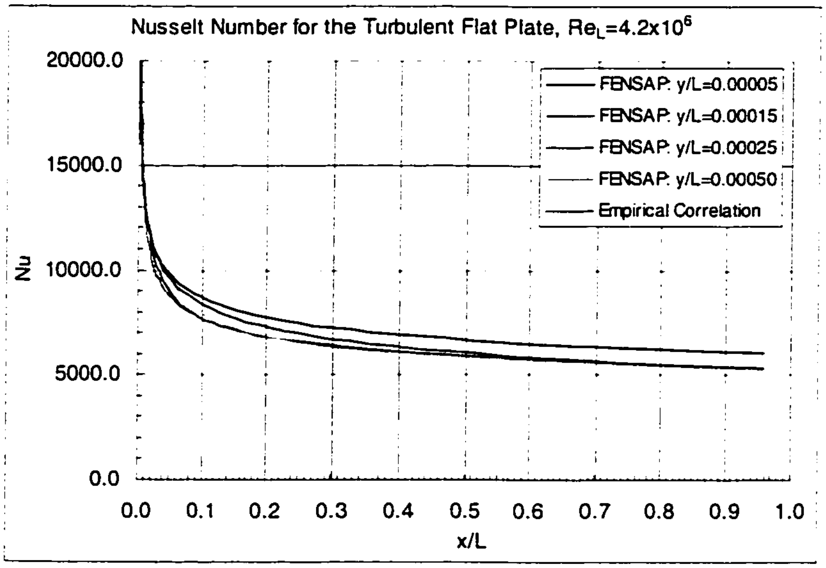

Figure 4.23: Nusselt Number for the Turbulent Flow over a Flat Plate

A comparison of the Nusselt number at x = L is presented in table 4.2 for the four grids tested.

	y_p/L	**Average y^+**	**% Error on Nu**
Grid 1	0.00005	10	+13.3
Grid 2	0.00015	28	+0.6
Grid 3	0.00025	42	-1.0
Grid 4	0.00050	88	-1.7

Table 4.2: Nusselt Number Sensitivity Study for the Turbulent Flow over a Flat Plate

The values presented in table 4.2 confirm the usual practice of positioning the first node-off-the-wall at a $30 < y^+ < 100$ to obtain meaningful results for wall bounded turbulent flows. FENSAP has shown that it can predict these types of flows reasonably well.

4.3.2. 2D Backward Facing Step

4.3.2.1. Introduction

The flow being modeled is the incompressible turbulent flow over a backward facing step. This test case evaluates the modeling assumptions for a flow that involves a reattachment of a separated turbulent boundary layer. The local Stanton number distribution along the impingement plate will be compared with the experimental data from Vogel and Eaton. [35]

4.3.2.2. Problem Definition

The geometry for the backward facing step is shown in figure 4.24, as suggested by Heyerichs and Pollard. [33] The geometry has been non-dimensionalized for a step height H. There is no wall region upstream of the step, i.e. the inlet is placed at the step face. The inlet height is 3.1-H, the exit is located 35-H downstream of the step face, and the far-field boundary condition was fixed at main stream values.

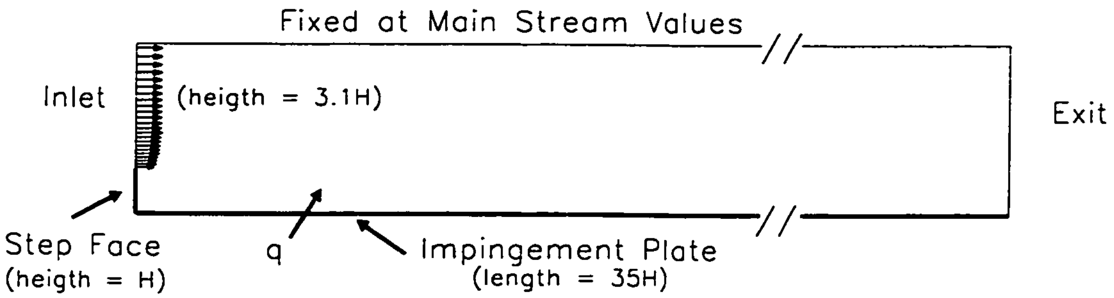

Figure 4.24: Computational Domain for the Turbulent Flow over a Backward Facing Step

4.3.2.3. Boundary Conditions

The boundary conditions for the flow analysis are as follows:

Inlet: Mach Number, $M_\infty = 0.10$

Static Temperature, $T_\infty = 300$ K

Reynolds Number, $Re_H = 28{,}000$

Turbulence Intensity, $i_\infty = 1.0\%$

Turbulent Viscosity Ratio, $\mu_{t\infty} / \mu_{l\infty} = 33.95$

Exit: Static Pressure, $p_\infty = 100$ kPa

Impingement Plate: Wall Heat Flux, $q_w = 270\ \mathrm{W/m^2}$

Step Face: Wall Temperature, $T_w = 300$ K

Since the inlet starts at the step face, the velocity profile was comprised of two regions: a uniform core region and a boundary layer region, as detailed in Heyerichs and Pollard. [33] The inlet height is 3.1-H where the boundary layer height is 1.1-H and the core region height is 2.0-H. The turbulence inlet quantities, however, were imposed uniformly at the inlet. The Reynolds number is based on the freestream conditions and the step height, as follows:

$$Re_H = \frac{\rho_\infty U_\infty H}{\mu_\infty} \tag{4.9}$$

4.3.2.4. Computational Grid

The test case used a structured hexahedral grid with 175 nodes in the axial direction, 50 nodes in the normal direction, and 2 nodes in the z-direction, for a total of 17,500 nodes, as shown in figure 4.25. The grid size in the x and y directions are as specified in Heyerichs and Pollard. [33] The grid was clustered in the normal direction to the impingement plate to resolve the recirculation, reattaching, and redeveloping near wall flow. It was also packed in the streamwise direction after the step face to resolve the flow gradients there, but was not clustered at the top of the step face since there was no wall region at the inlet. A grid study was quickly assessed by changing the first node-off-the-wall height and, only the optimal grid is shown here. The resulting average y^+ for this grid was 7.0, which is below the usual wall function range, but FENSAP can still resolve the near-wall gradients. For the specified grid size in the normal direction, a higher y^+ would result in missing the redeveloping boundary layer.

Backward Facing Step Grid (17,500 Nodes)

Figure 4.25: Grid for the Turbulent Flow over a Backward Facing Step

4.3.2.5. Results & Discussion

The convergence of this test case is shown in figure 4.26. The test case was started from no initial solution with only 1 cycle of artificial dissipation. The final cycle exceeded the residual reduction of 3 orders of magnitude and, converged to an absolute value of 10^{-8}.

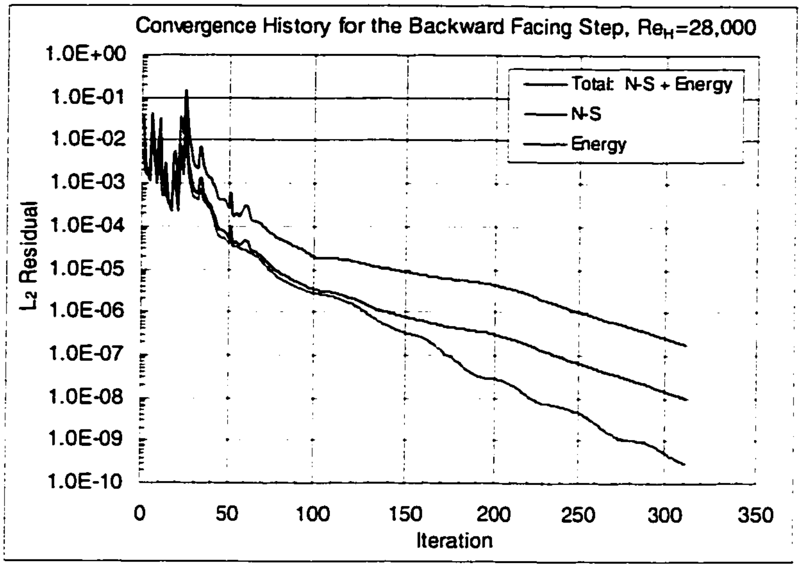

Figure 4.26: Convergence History for the Turbulent Flow over a Backward Facing Step

The Mach number and static temperature downstream of the step face are shown in figures 4.27 and 4.28, respectively. Notice the recirculation pattern in the Mach number field after the step face.

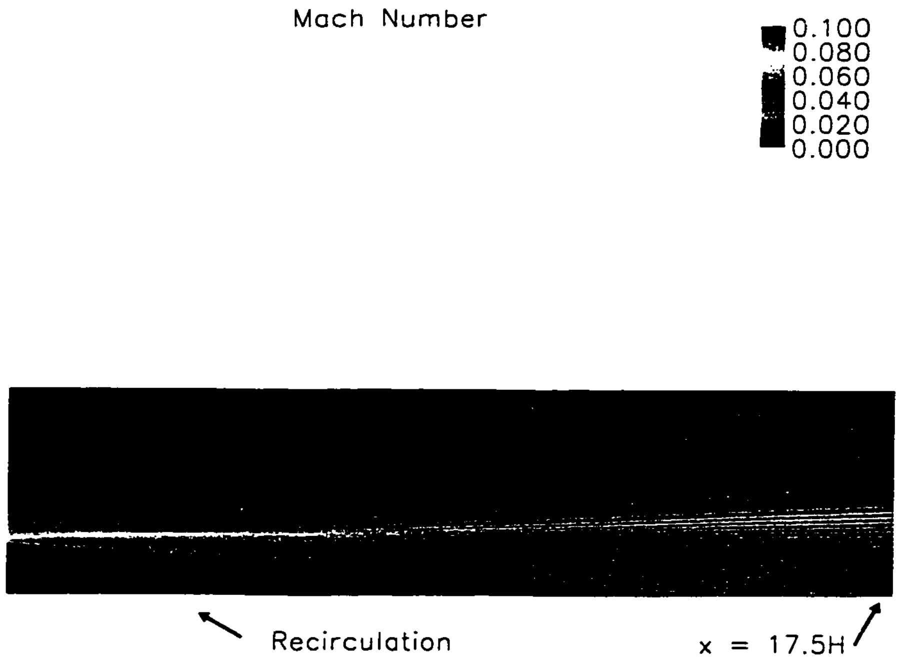

Figure 4.27: Mach Number Distribution Downstream of the Step Face

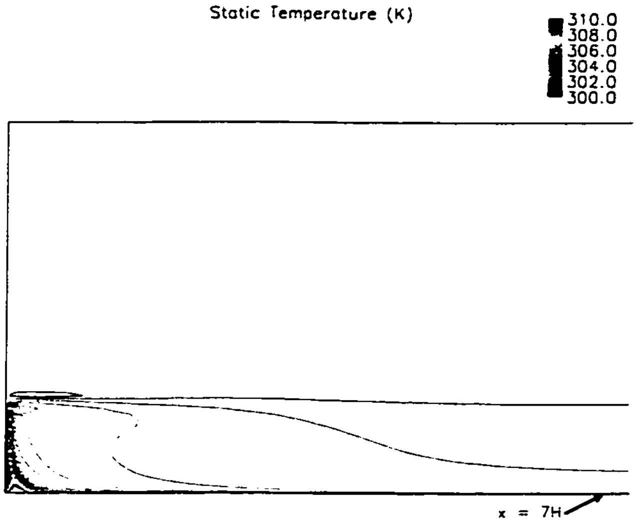

Figure 4.28: Static Temperature Distribution Downstream of the Step Face

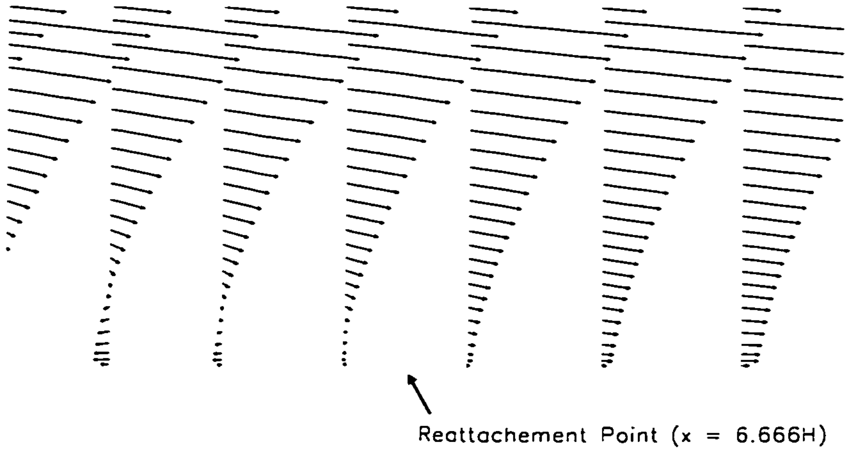

Figure 4.29: Velocity Vectors near the Reattachment Point

To evaluate the accuracy of the heat transfer prediction, the computed local Stanton number distribution along the impingement plate is compared with the data of Vogel and Eaton. [35] The local Stanton number is defined as:

$$\mathrm{St} = \frac{h}{U_\infty \rho_\infty c_{p\infty}} = \frac{q}{(T_w - T_\infty) U_\infty \rho_\infty c_{p\infty}} \tag{4.10}$$

where h is the heat transfer coefficient, q is the heat flux, T_w is the wall temperature, T_∞ is the freestream temperature, U_∞ is the freestream velocity, ρ_∞ is the freestream density, and $c_{p\infty}$ is the freestream specific heat of the air.

The comparison is shown in figure 4.30. FENSAP seems to pick up the global trend, as mentioned about similar wall function turbulence models tested in Heyerichs and Pollard. [33]

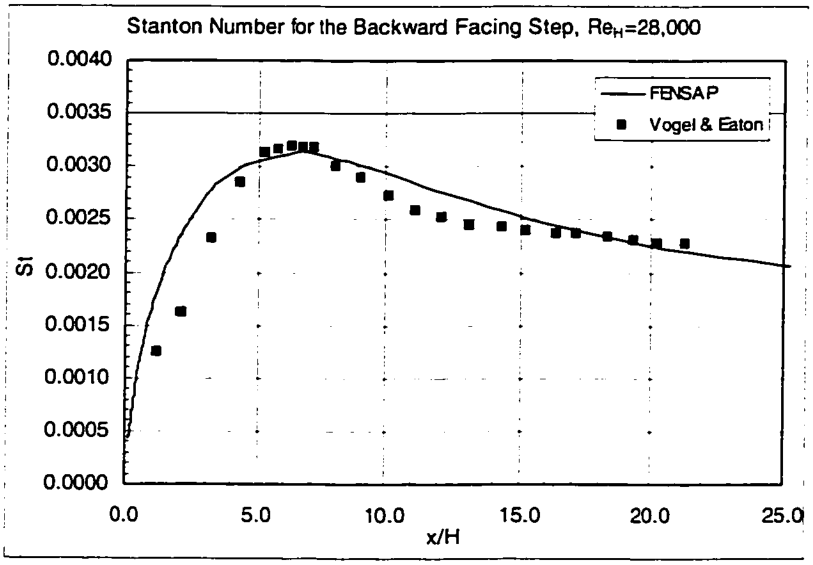

Figure 4.30: Stanton Number for the Turbulent Flow over a Backward Facing Step

In order to quantify and rank each turbulence model, Heyerichs and Pollard suggest comparing four results: maximum St, location of the maximum St, the value of St downstream of reattachment at x/H = 20, and the point of reattachment (x/H). [33] The experimental data of Vogel and Eaton are [35]:

1. $St_{max} = 0.0032$
2. x/H, $St_{max} = 6.00$

3. At x/H =20, St = 0.00229
4. $x/H_{reatt} = 6.67$

Turbulence Model	$\mathbf{St_{max}}$	**x/H,** $\mathbf{St_{max}}$	**St, x/H=20**	$\mathbf{X/H_{reatt}}$
FENSAP	-1.7	10.9	-1.3	-0.2
WF1, 1 layer [33]	1.6	-17.8	0.6	-10.5
WF2. 2 layer [33]	-5.2	-17.8	0.6	-9.9
WF3, 2 layer+ [33]	5.3	-11.7	14.3	-15.6
Chien [33]	175.6	34.7	61.7	-10.2
Lam & Bremhost [33]	93.5	-7.6	53.9	-16.5
Launder & Sharma [33]	469.0	-7.6	30.7	-16.8
Launder et al. [33]	37.6	-7.6	3.8	-6.3
Myong & Kasagi [33]	151.8	-26.8	31.8	9.9
Wolfshtein, Chen & Patel [33]	-28.7	-22.9	-10.5	6.0
Wilcox [33]	-2.5	4.0	-0.7	11.3

Table 4.3: Percentage Errors for the Turbulent Flow over a Backward Facing Step

The results in table 4.3 indicate that FENSAP behaves closely to a wall function model for this type of flow, and is a better match to the data then most of the low-Reynolds turbulence models. As mentioned in Heyerichs and Pollard, using a low-Reynolds number model for this type of flow does not necessarily lead to better results if the near-wall functions are based on friction velocity or distance from the wall. [33]

4.3.3. 2D Impinging Jet

4.3.3.1. Introduction

The flow being modeled is the incompressible turbulent flow for an impinging jet. This test case evaluates the near-wall modeling assumptions. The local Nusselt number distribution along the impingement plate will be compared with the experimental data from Van Heiningen. [36]

4.3.3.2. Problem Definition

The geometry for the impinging jet is shown in figure 4.31 as suggested by Heyerichs and Pollard. [33] The geometry has been non-dimensionalized for an inlet width W. Due to symmetry conditions, only half of the geometry is solved. Thus, the inlet width is W/2. The exit is located 49 W downstream of the inlet centerline. The gap between the confinement plate and the impingement plate is of height H where H/W = 2.6.

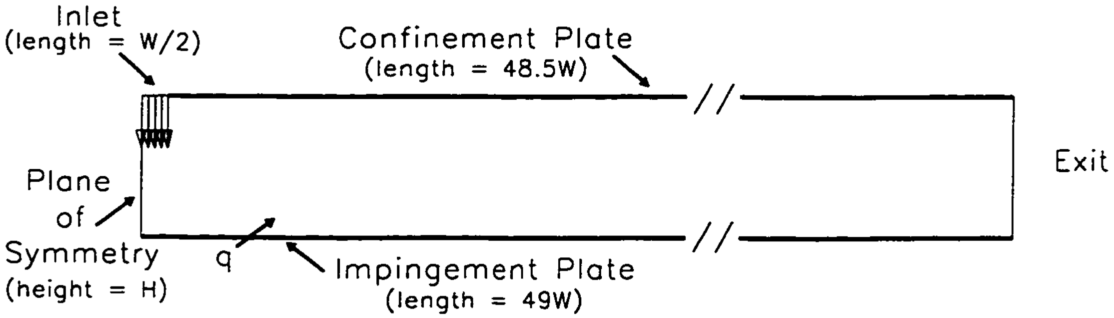

Figure 4.31: Computational Domain of the Turbulent Flow from an Impinging Jet

4.3.3.3. Boundary Conditions

The boundary conditions for the flow analysis are as follows:

Inlet: Mach Number, $M_\infty = 0.10$

Static Temperature, $T_\infty = 300$ K

Reynolds Number, $Re_w = 10{,}000$

Turbulence Intensity, $i_\infty = 0.5\%$

Turbulent Viscosity Ratio, $\mu_{t\infty} / \mu_{l\infty} = 2.76$

Exit: Static Pressure, $p_\infty = 100$ kPa

Impingement Plate: Wall Temperature, $T_w = 310$ K

Confinement Plate: Wall Temperature, $T_w = 300$ K

The inlet velocity profile was uniform, as well as the inlet turbulence quantities. The Reynolds number is based on the freestream conditions and the inlet width, as follows:

$$Re_W = \frac{\rho_\infty U_\infty W}{\mu_\infty} \tag{4.11}$$

4.3.3.4. Computational Grid

The present test case used a structured hexahedral grid with 92 nodes in the axial direction, 30 nodes in the normal direction, and 2 nodes in the z-direction, for a total of 5,520 nodes, as shown in figure 4.32. The grid size in the x and y directions are as specified in Heyerichs and Pollard. [33] The grid was clustered in the normal direction to the impingement plate to resolve the impingement and developing near wall flow. It was also packed in the streamwise direction around and after the inlet region, to resolve the flow gradients there. Minimal grid clustering was done on the confinement plate since the flow in that region was of no interest for this study. A grid study was quickly assessed by changing the first node-off-the-wall height, and only the optimal grid is shown here. The resulting average y^+ for this grid was 1.5, which is below the usual wall function range but FENSAP can still resolve the near wall gradients. For the specified grid size in the normal direction, a higher y^+ would result in missing the developing boundary layer.

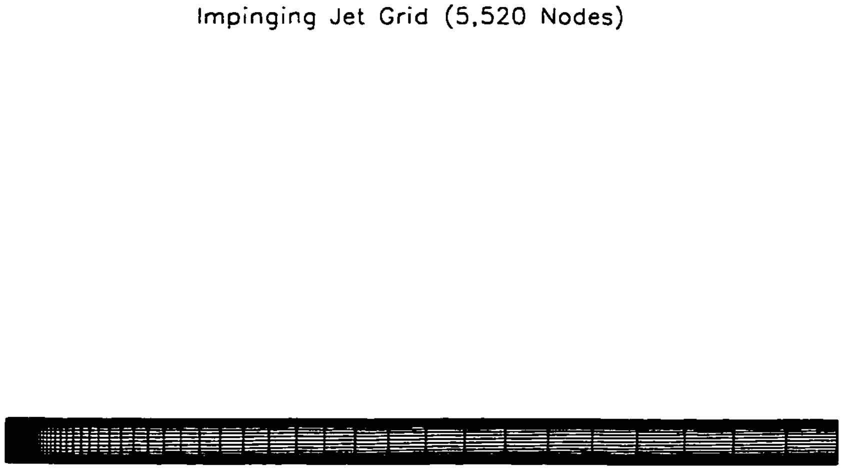

Figure 4.32: Grid of the Turbulent Flow from an Impinging Jet

4.3.3.5. Results & Discussion

The convergence of this test case is shown in figure 4.33. The test case was started from no initial solution with only 1 cycle of artificial dissipation. The final cycle exceeded the residual reduction of 3 orders of magnitude, and converged to an absolute value of 10^{-8}. Some minor convergence problems were observed in the energy equation but nonetheless the solution is still valid.

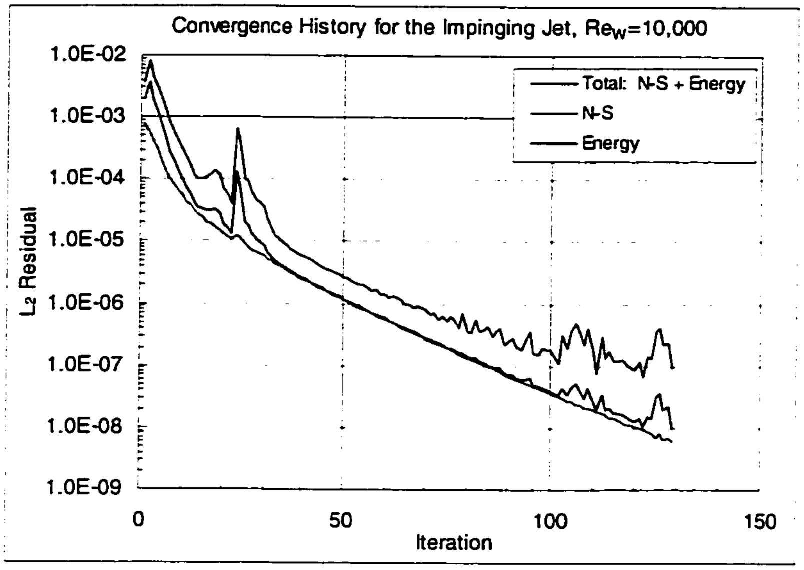

Figure 4.33: Convergence History of the Turbulent Flow from an Impinging Jet

The Mach number and static temperature in the confined region are shown in figures 4.34 and 4.35, respectively. Notice the complex interaction between the impinging jet, the stagnation region, and the developing boundary layer. The recirculation pattern around the confinement plate after the inlet is also evident.

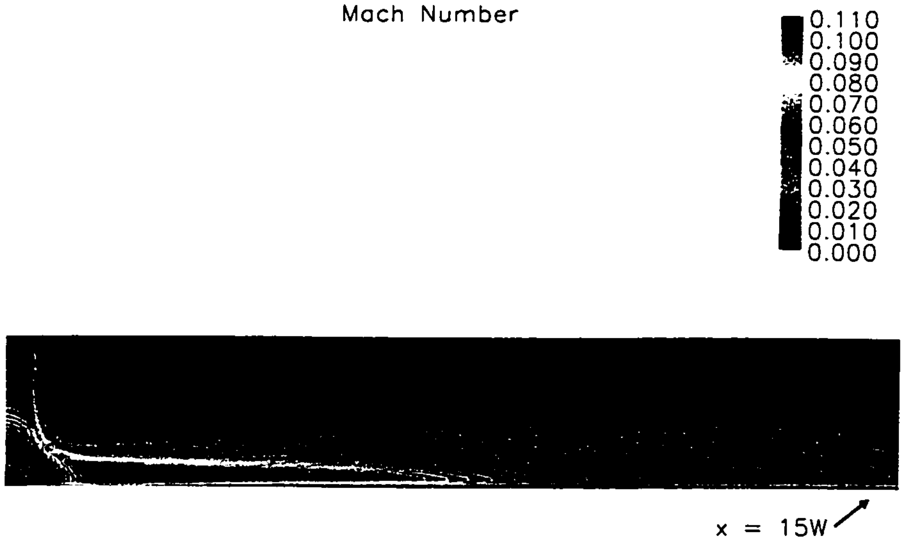

Figure 4.34: Mach Number Distribution in the Confined Region

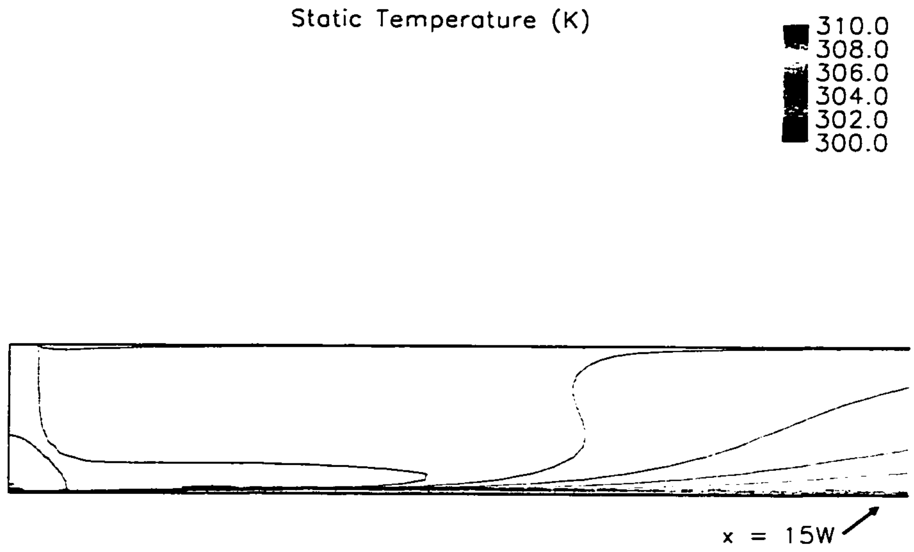

Figure 4.35: Static Temperature Distribution in the Confined Region

To evaluate the accuracy of the heat transfer prediction, the computed local Nusselt number distribution along the impingement plate is compared with the data of Van Heiningen. [36] The local Nusselt number is defined as:

$$Nu = \frac{hW}{k} = \frac{qW}{k(T_w - T_\infty)} \tag{4.12}$$

where h is the heat transfer coefficient, q is the heat flux, W is the width of the inlet, T_w is the wall temperature, T_∞ is the inlet temperature, and k is the thermal conductivity of the air.

The comparison of the computed results with the experimental results is shown in figure 4.36. FENSAP seems to pick up the global trends but behaves differently than similar wall function turbulence models found in Heyerichs and Pollard. [33] Although not shown here, FENSAP behaves closer to the Launder &

Sharma and Launder et al. turbulence models but with a better match to the data than most of the low-Reynolds turbulence models. [33] Also, the secondary peak is observed farther downstream with FENSAP since the boundary layer development is predicted wrongly from what was observed in the experiment.

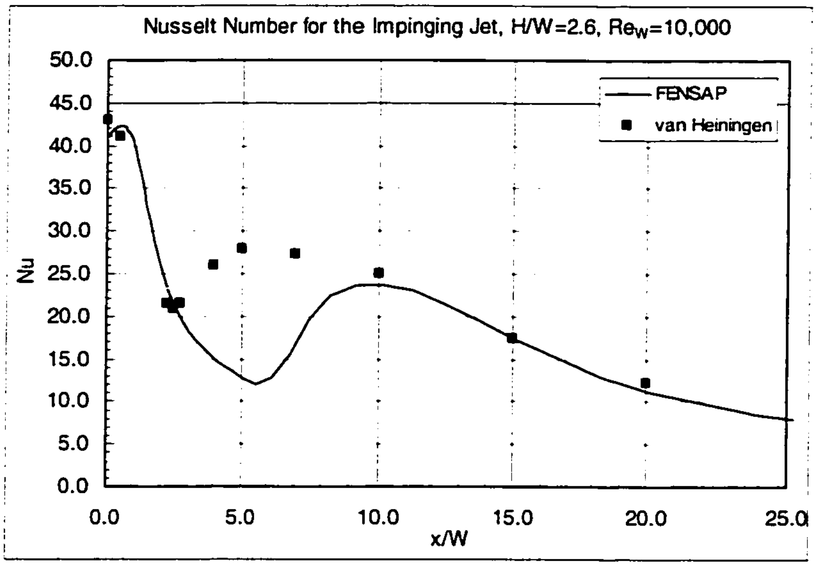

Figure 4.36: Nusselt Number of the Turbulent Flow from an Impinging Jet

In order to quantify and rank each turbulence model, Heyerichs and Pollard suggest comparing three results: maximum Nu at the stagnation region, maximum Nu in the secondary peak, and the value of Nu downstream of the inlet at x/W = 20. [33] The experimental data of van Heiningen [36]:

1. $Nu_{max1} = 43.0$
2. $Nu_{max2} = 27.0$
3. At x/W =20, Nu = 15.0

Turbulence Model	**Nu_{max1}**	**Nu_{max2}**	**Nu, x/W=20**
FENSAP	-1.6	-12.2	-5.8
WF1, 1 layer [33]	-27.8	32.0	9.6
WF2. 2 layer [33]	-21.5	34.9	18.0
WF3, 2 layer+ [33]	-21.6	38.4	25.8
Chien [33]	18.8	39.9	6.1
Lam & Bremhost [33]	12.5	49.1	8.0
Launder & Sharma [33]	5.0	26.1	18.6
Launder et al. [33]	4.9	25.3	-3.6
Myong & Kasagi [33]	30.6	-4.7	11.1
Wolfshtein, Chen & Patel [33]	12.8	not present	-30.5
Wilcox [33]	9.9	19.5	-13.0

Table 4.4: Percentage Errors for the Turbulent Flow for the Impinging Jet

The results in table 4.4 further indicate that FENSAP does not behave like a wall function model for this type of flow. As mentioned in Heyerichs and Pollard, using a wall function or low-Reynolds number model for this type of flow does not necessarily lead to better results if the near-wall turbulence is based on friction velocity or distance from the wall; it is not even recommended. [33] However, FENSAP behaves like a combination of a wall function and low-Reynolds turbulence models for this type of flow.

5. Conjugate Heat Transfer Validation of FENSAP

5.1. Introduction

The conjugate heat transfer validation of FENSAP for both laminar and turbulent flows is conducted in this thesis through the following 3 test cases:

1. 2D Laminar Flow over a Flat Plate with a Blunt Leading Edge
2. 3D Fully-developed Laminar Pipe Flow
3. 3D Turbulent Flow over a Nacelle Lip equipped with a Piccolo Tube System

The first test case was used to test the coupling algorithm and the interpolation routines. The metal conductivity of the plate being so high (10^4 times the air conductivity) caused the temperature variation through the metal to be very low, i.e. the plate was nearly isothermal. The second test case was a true test of the CHT algorithm, since it closely couples the Navier-Stokes and Energy equations, of both the fluid and solid domains. This was accomplished by setting the metal to air conductivity ratio in the orders of 1 to 10. The results of the first two test cases are compared to available empirical correlations and/or open literature numerical results. Finally, the last test case involved the complex 3D anti-icing flow interaction of a piccolo tube system impinging on a model nacelle lip placed in a wind tunnel. [37, 38] This last test case also tested the conservative coupling methodology (because of extensive anisotropic mesh adaptation in the fluid domain). The results are compared to available open literature experimental results from Scarsi. [38]

The 2D test cases are simulated in FENSAP with two planes in the z-direction since FENSAP is a 3D code. One plane imposes a symmetry condition, while the other plane imposes a periodic condition.

For test cases 1&3, grid sensitivity studies were performed through anisotropic mesh adaptation using OptiMesh™. For test case 2, a couple of refined grids were created to verify the near-wall grid spacing and the inlet region spacing to capture the temperature variations. Only the results from the best grids are presented unless stated otherwise.

Each test case was initialized with freestream conditions. The simulations were performed until the absolute combined residual for the continuity, momentum and energy equations was below a value of 10^{-8} or, that this maximum normalized residual was reduced by 3 orders of magnitude (10^{-3}). The overall CHT residual is also tracked at all the interfaces. The CHT residual is a L_2 norm of the temperature variable from iteration to iteration at all the interfaces.

5.2. 2D Laminar Flow over a Flat Plate with a Blunt Leading Edge

5.2.1. Introduction

The flow being modeled is the laminar flow over a smooth flat plate with a blunt leading edge as tested by Imlay et al., and by Kao et al. [6, 12] The local Nusselt number distribution along the plate can be compared with that of the well-known correlation of Eckert for an isothermal wall. [30]

5.2.2. Problem Definition

The geometry for the flat plate is shown in figure 5.1 and has been non-dimensionalized for a flat plate of length L. The inlet is placed 2-L upstream of the plate leading edge. A symmetry condition is imposed upstream of the plate while the far-field boundary condition, 2-L above the plate, was fixed at main stream values. The exit is downstream of the plate. The plate thickness was set to 0.0025-L. The close-up view of the flat plate geometry is shown in figure 5.2.

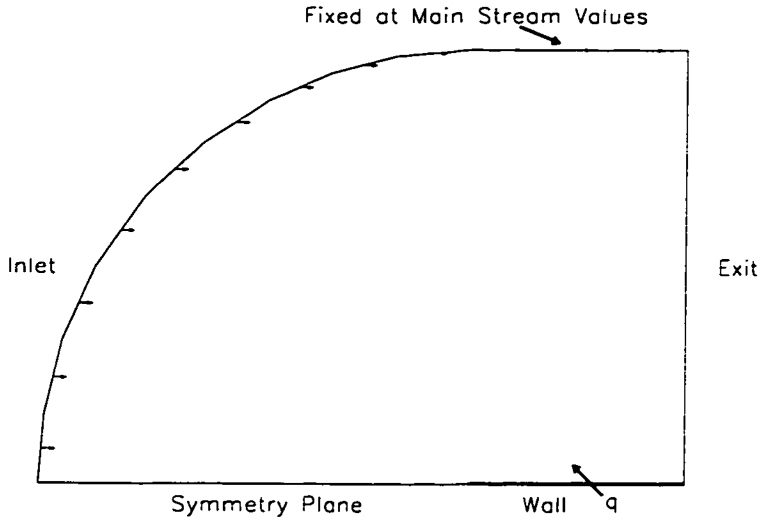

Figure 5.1: Computational Domain for the Flat Plate with a Blunt LE

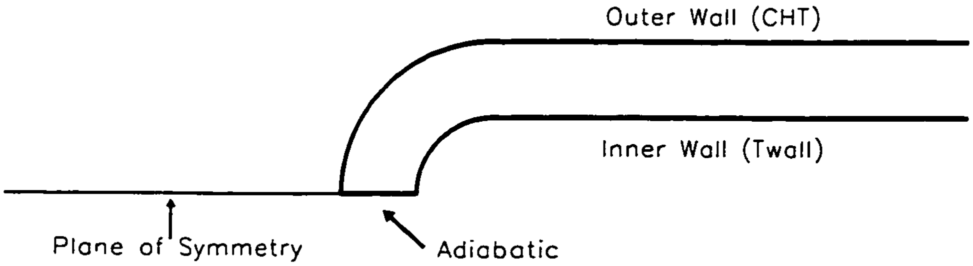

Figure 5.2: Computational Domain for the Flat Plate with a Blunt LE (close-up)

5.2.3. Boundary Conditions

The boundary conditions for the flow domain are as follows:

Inlet: Mach Number, $M_\infty = 0.30$

Static Temperature, $T_\infty = 300$ K

Reynolds Number, $Re_L = 10{,}000$

Exit: Static Pressure, $p_\infty = 100$ kPa

Outer Wall: Conjugate Heat Transfer

The inlet velocity profile was uniform at the inlet. The Reynolds number is based on the freestream conditions and the plate length, as follows:

$$Re_L = \frac{\rho_\infty U_\infty L}{\mu_\infty} \tag{5.1}$$

The boundary conditions for the solid domain are as follows:

Outer Wall: Conjugate Heat Transfer

Inner Wall: Wall Temperature, $T_w = 280$ K

Plate Ends: Adiabatic

The wall metal is aluminum, with the following constant properties:

Density, $\rho_s = 2{,}700$ kg/m^3

Thermal Conductivity, $k_s = 211$ W/m-K

Specific Heat, $c_s = 900$ W-s/kg-K

5.2.4. Computational Grids

The test case used an unstructured grid for the fluid domain and a structured grid for the solid domain. Through anisotropic mesh adaptation, the best fluid grid was obtained for a specified target number of nodes. The variable used for the adaptation error estimation was the Mach number. The initial fluid grid had 22,146 nodes, as shown in figure 5.3, while the final adapted fluid grid had 8,182 nodes, as shown in figure 5.4.

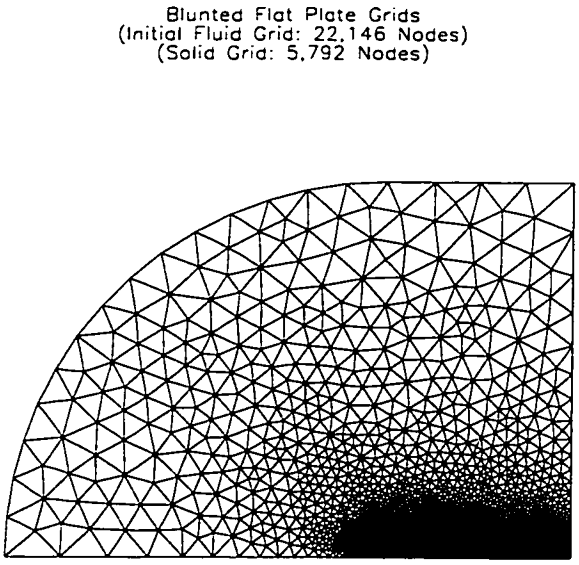

Figure 5.3: Initial Grids for the Flat Plate with a Blunt LE

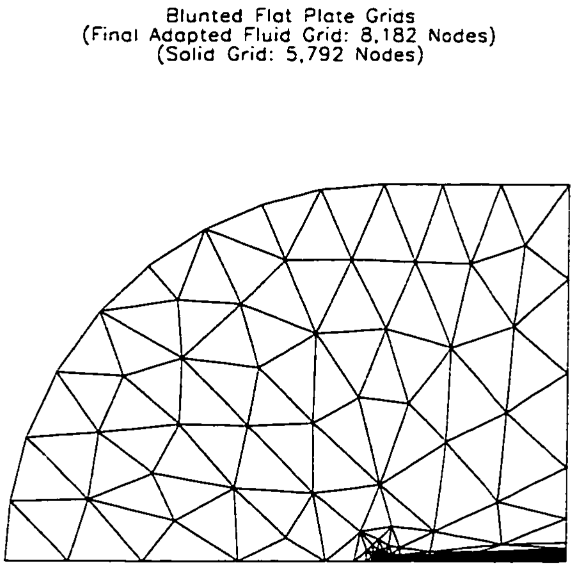

Figure 5.4: Adapted Grids for the Flat Plate with a Blunt LE

A close-up view of the grids is shown in figure 5.5. Notice how the mesh adaptation clustered the grid points near the leading edge of the plate and along the plate to resolve the flow gradients present in the boundary layer, as shown in figure 5.5. The solid grid had 5,792 nodes and was not adapted. The interface between the fluid grid and the solid grid had non-matching node connectivity, as shown in figure 5.5.

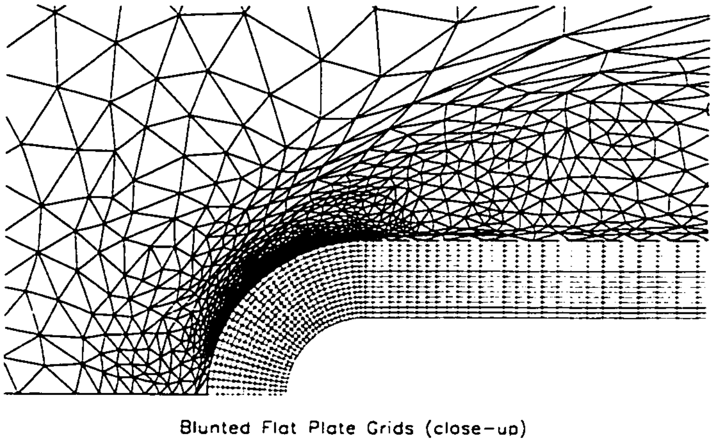

Figure 5.5: Adapted Grids for the Flat Plate with a Blunt LE (close-up)

5.2.5. Results & Discussion

The convergence of this test case is shown in figure 5.6. To prove the robustness of FENSAP, the test case was started from no initial solution with 2 cycles of artificial dissipation since the adapted grid had very skewed elements. The final cycle exceeded the residual reduction of 3 orders of magnitude, and converged to an absolute value of 10^{-8}. Although the Energy equation residual was not reduced by 3 orders of magnitude nor was it below 10^{-8} it was judged to have achieved convergence.

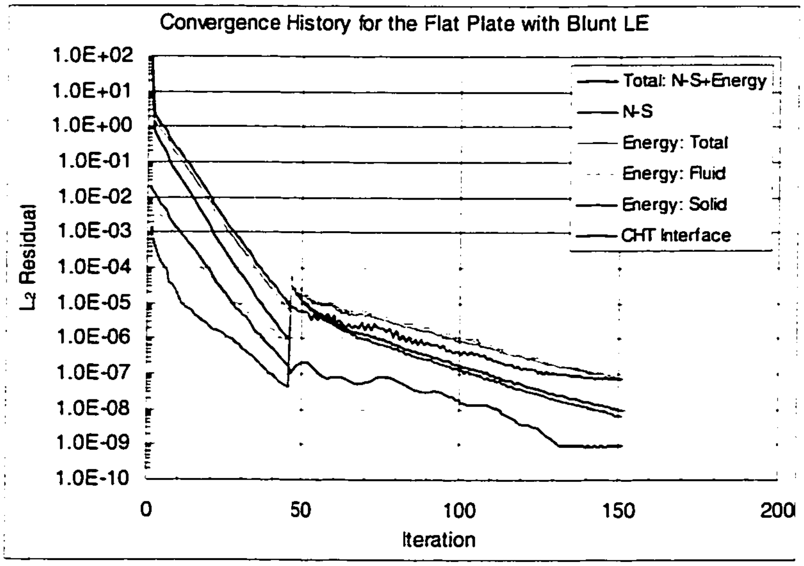

Figure 5.6: Convergence History for the Flat Plate with a Blunt LE

The Mach number and static temperature along the flat plate are shown in figures 5.7 and 5.8, respectively. From figure 5.5, 5.7, and 5.8 we can see that the fluid grid is aligned with the Mach number and static temperature field.

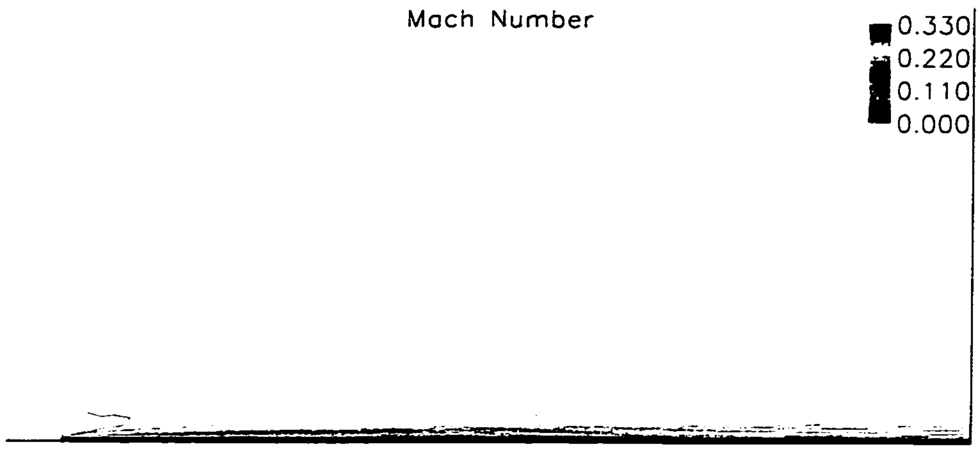

Figure 5.7: Mach Number Distribution along the Plate

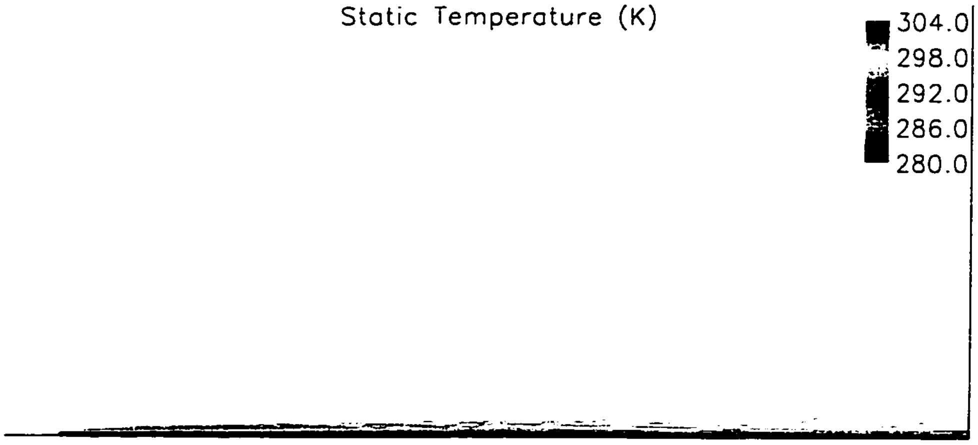

Figure 5.8: Static Temperature Distribution along the Plate

The metal conductivity of the plate being 10^4 orders of magnitude higher than the air conductivity caused the temperature variation through the metal to be very low, i.e. the plate was isothermal. Therefore, the computed local Nusselt number can be compared with that of the well-known correlation of Eckert for isothermal wall. [30] The local Nusselt number is defined as:

$$Nu = \frac{qL}{k(T_w - T_{aw})} \qquad (5.2)$$

where q is the heat flux, L is the plate length, T_w is the wall temperature, T_{aw} is the adiabatic wall temperature, and k is the thermal conductivity of the air. The analytical Nusselt number is given by [30]:

$$Nu = 0.333\sqrt[3]{Pr}\sqrt{Re_x}\frac{L}{x} \tag{5.3}$$

The results of this comparison are shown in figure 5.9. The computed and analytical results are nearly identical everywhere except at the leading edge, where the analytical results are not valid because of the blunt geometry. Note how the solution at the interface is identical. At the end of the plate, the Nusselt number is under-predicted from the analytical value by 1.5%.

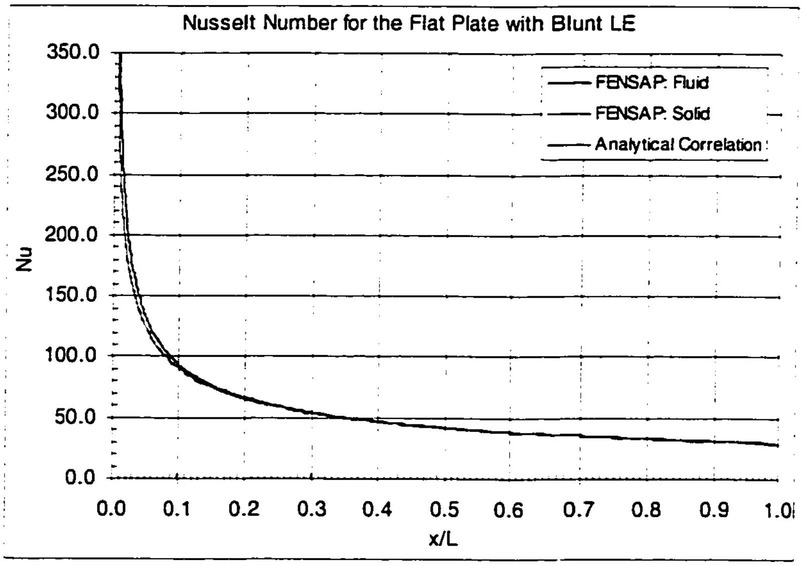

Figure 5.9: Nusselt Number for the Flat Plate with Blunt LE

5.3. 3D Fully-developed Laminar Pipe Flow

5.3.1. Introduction

The flow being modeled is the conjugate heat transfer in a fully-developed laminar pipe flow. It is a typical Graetz thermal entrance problem where exact solutions can be computed for isothermal pipe walls. This problem was analyzed analytically by Pozzi & Lupo, and numerically by Imlay et al. [39, 6] The local interface wall temperature along the pipe can be compared with the analytical results presented by Pozzi & Lupo. [39]

5.3.2. Problem Definition

The geometry for the pipe is shown in figure 5.10 with a close-up view in figure 5.11. The geometry has been non-dimensionalized for a pipe diameter D and has a pipe length of 20-D. The pipe thickness t was chosen to be 0.125-D. To ensure the minimum thermal entrance length for a Graetz type of problem the following formula can be used [40]:

$$\frac{L_{e,\text{thermal}}}{D} \approx 0.05\,\mathrm{Re}_D\,\mathrm{Pr} \qquad (5.4)$$

For the Reynolds number and Prandtl number chosen in this test case, a pipe length of 40-D would have been needed. However, since most of the data used for comparison is within the first D length of the pipe there was no need to extend the length of the pipe that far and so, half of this thermal length was chosen, i.e. 20-D. This value was also chosen in the analysis by Imlay et al. [6] The test case was run in a three-dimensional mode with only half of the pipe, since a symmetry condition existed there. The test case could have been run with axisymmetric conditions but the three-dimensional CHT modeling was tested instead for debugging purposes.

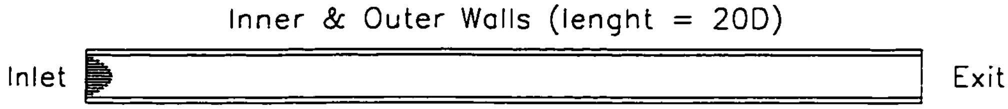

Figure 5.10: Computational Domain for the 3D CHT Pipe Flow

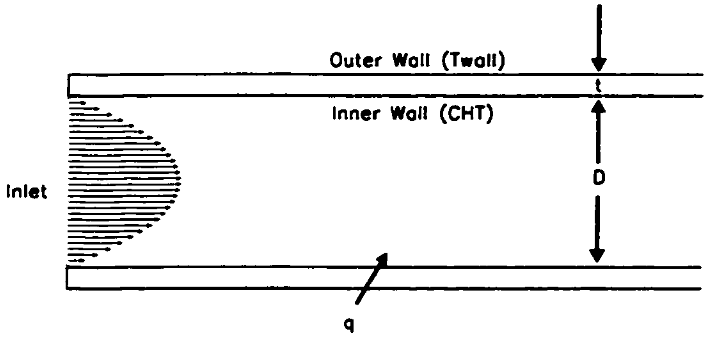

Figure 5.11: Computational Domain for the 3D CHT Pipe Flow (close-up)

5.3.3. Boundary Conditions

The boundary conditions for the flow domain are as follows:

Inlet: Mach Number, $M_\infty = 0.01$

Static Temperature, $T_\infty = 300$ K

Reynolds Number, $Re_D = 1{,}108$

Prandtl Number, $Pr = 0.72$

Thermal Conductivity, $k_f = 0.0259$ W/m-K

Exit: Static Pressure, $p_\infty = 101.325$ kPa

Pipe Inner Wall: Conjugate Heat Transfer

The inlet velocity profile was a three-dimensional fully-developed Poiseuille flow parabolic profile for pipes such as [40]:

$$\frac{u}{\bar{u}}=2\left(1-4\left(\frac{r}{D}\right)^2\right) \tag{5.5}$$

where $\bar{u}=U_\infty=0.5u_{max}$ is the average velocity at the inlet of the pipe, r is the radius in the pipe, and D is the diameter of the pipe. The inlet static temperature is uniform. The inlet Mach number is based on the average velocity and static temperature. The Reynolds number is based on the freestream conditions and the pipe diameter, as follows:

$$Re_D=\frac{\rho_\infty U_\infty D}{\mu_\infty} \tag{5.5}$$

The boundary conditions for the solid domain are as follows:

Pipe Outer Wall: Wall Temperature, $T_w=320$ K

Pipe Inner Wall: Conjugate Heat Transfer

Pipe End Walls: Adiabatic

Thermal Conductivity: $k_S = 0.0578$ W/m-K

This test case was run with fixed thermal conductivities for both the fluid and the solid, as assumed by Pozzi & Lupo. [39] The value for the solid thermal conductivity was chosen with the following formula [39]:

$$p=\frac{k_f}{k_s}Ln\left(1+\frac{2t}{D}\right) \tag{5.6}$$

where p is a ratio parameter for the thermal conductivities. The value chosen for the test case in this thesis is $p = 0.10$. Contrary to Pozzi & Lupo, the following test case:

- does NOT neglect dissipation in the fluid,
- does NOT neglect axial heat conduction in the pipe walls, and
- is NOT modeled with an incompressible flow.

The boundary conditions and geometry used in Imlay at al. are somewhat conflicting as they lead to a $Re_D = 1.11 \times 10^5$ whereas the assumption of laminar flow in a pipe is $Re_D < 2{,}000$! Thus, no comparison will be established with their computed results.

5.3.4. Computational Grids

The test case used structured grids for both the fluid and solid domains. The grid was clustered in the normal direction to the wall to resolve the boundary layer. It was also packed in the streamwise direction near the leading edge of the pipe to resolve the flow and temperature gradients there. Grid refinement studies were conducted to verify the above-mentioned grid criteria. Only the results from the best grids are presented here. For the half pipe geometry, the fluid grid had 74,841 nodes, while the solid grid had 50,096 nodes, as shown in figures 5.12 with a close view in figure 5.13. An axial view of the grids is also shown in figure 5.14. The interface between the fluid grid and the solid grid had matching node connectivity, as shown in figures 5.13 and 5.14.

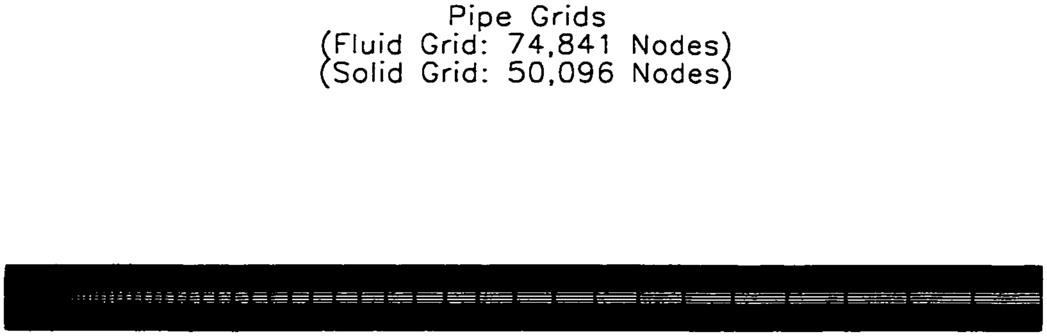

Figure 5.12: Grids for the 3D CHT Pipe Flow

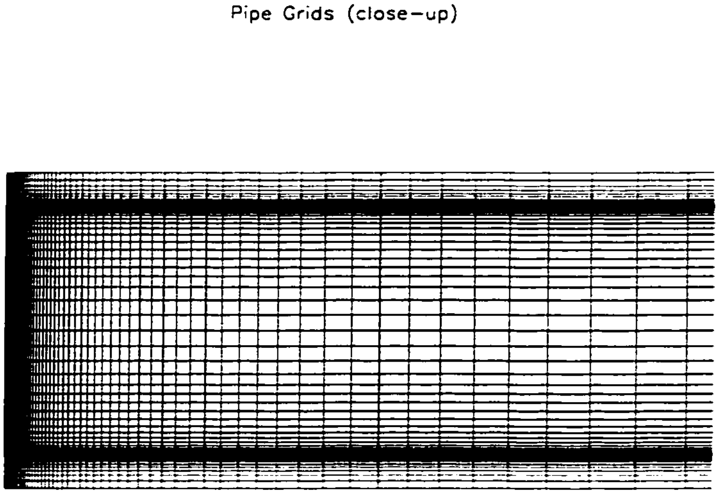

Figure 5.13: Grids for the 3D CHT Pipe Flow (close-up)

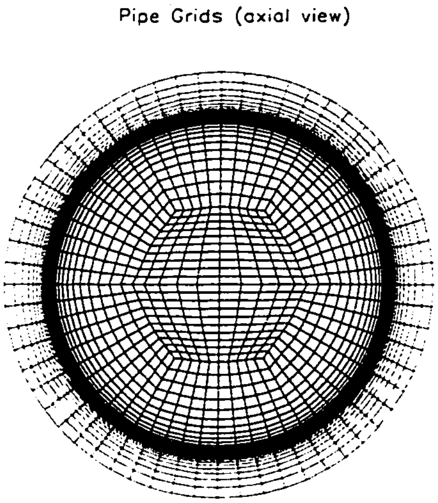

Figure 5.14: Grids for the 3D CHT Pipe Flow (axial view)

5.3.5. Results & Discussion

The convergence of this test case is shown in figure 5.15. The test case was started from no initial solution, with 2 cycles of artificial dissipation. The final cycle exceeded the residual reduction of 3 orders of magnitude and converged to an absolute value of 10^{-8}. Although the Energy equation residual was not below 10^{-8} it was reduced by 3 orders of magnitude and was judged to have converged.

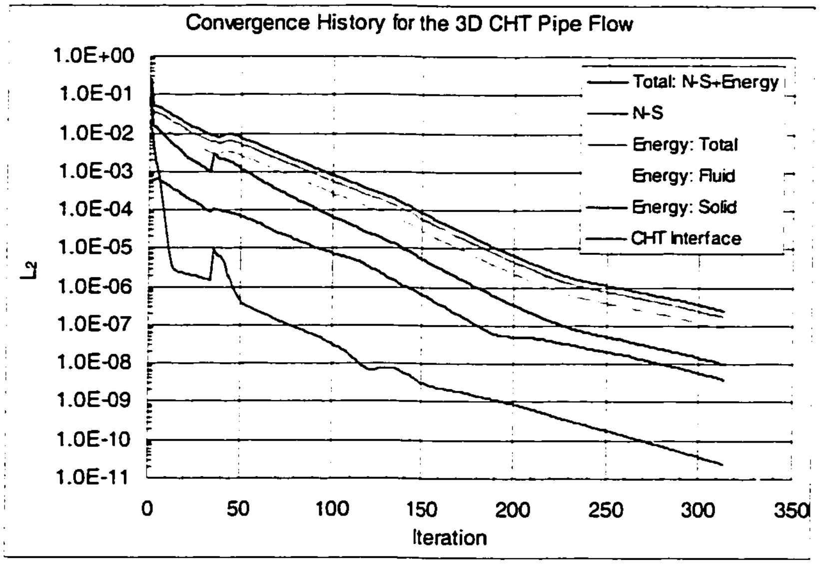

Figure 5.15: Convergence History for the 3D CHT Pipe Flow

Table 5.1 presents a comparison of the cost, in terms of iterations, to compute a CHT solution with the same level of convergence versus the following options:

1. adiabatic wall solution,
2. constant wall temperature solution,
3. adiabatic wall solution + 1-step CHT solution, and
4. constant wall temperature solution + 1-step CHT solution.

Solution Type	Total Number of Iterations
CHT	314
Adiabatic Wall	205
Constant Wall Temperature	187
Adiabatic Wall + CHT	478
Constant Wall Temperature + CHT	420

Table 5.1: Solution Cost versus Solution Type for the 3D CHT Pipe Flow

The results in table 5.1 show that the cost of a CHT solution is greater than an adiabatic or a constant wall temperature solution. However, the results in table 5.1 also show that the cost associated with computing a CHT solution from an initial converged solution is more costly than computing a CHT solution from the start. The robust CHT algorithm offers this advantage.

The convergence of the interface average wall temperature is shown in figure 5.16. It shows that essentially, the energy equation gets decoupled from the Navier-Stokes equation after 100 iterations. We knew ahead of time that the problem being solved is an incompressible flow where the thermal field is evolving while the dynamic field is fixed. Note that the residual level of the Navier-Stokes equations is reduced by 3 orders of magnitude after 100 iterations. Performing multiple Energy equation loops for every Navier-Stokes equation loop would speed up the overall convergence for this incompressible flow. This option was used in the test case but not to its full extent.

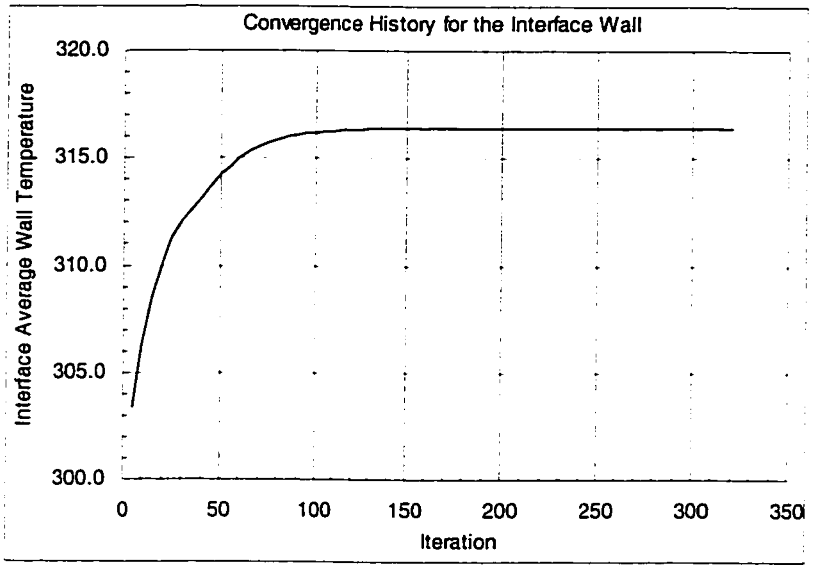

Figure 5.16: Convergence History for the CHT Interface Wall of the 3D Pipe

The Mach number and axial velocity along the mid-plane of the pipe are shown in figures 5.17 and 5.18, respectively. Notice how the fully-developed velocity profile is maintained in the streamwise direction, as expected. The thermal field has no effect on the dynamic field in this incompressible pipe flow.

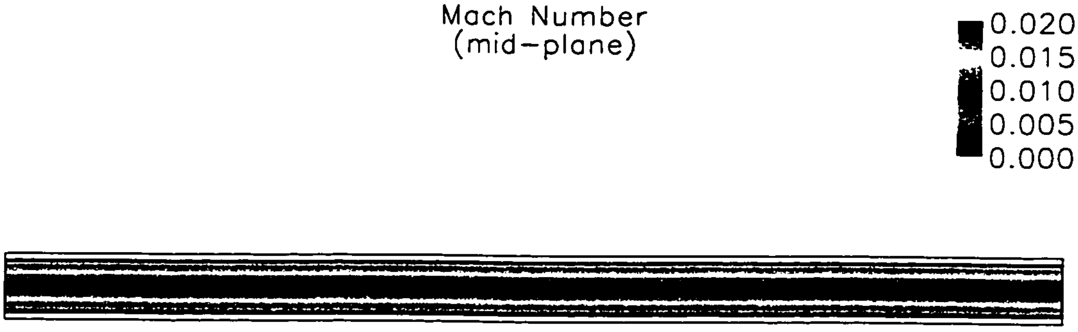

Figure 5.17: Mach Number along the mid-plane for the 3D CHT Pipe

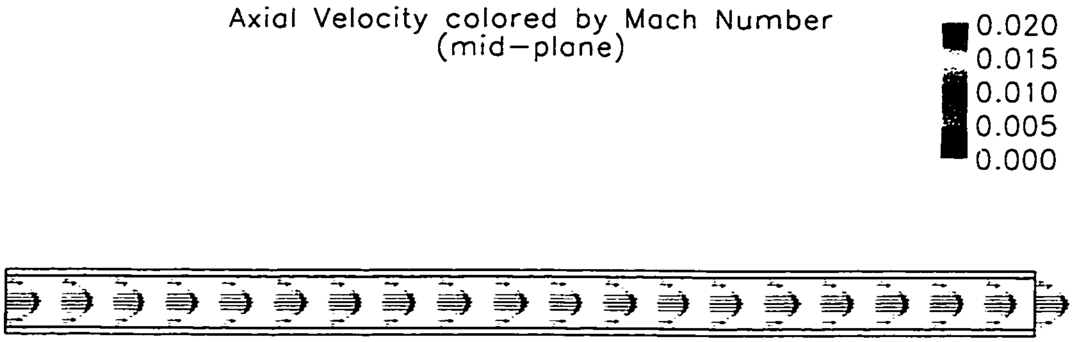

Figure 5.18: Axial Velocity along the mid-plane for the 3D CHT Pipe

The static temperature along the mid-plane of the pipe for both the fluid and solid domains is shown in figure 5.19. Notice how the temperature contours are continuous at the CHT interface as shown in a close-up view in figure 5.20. Figure 5.20 also shows that there is a temperature variation in the pipe walls because of the low thermal conductivity ratio (k_f/k_s=2.23). The inner pipe wall temperature is shown in figure 5.21, with a close-up view in figure 5.22. Notice how the wall temperature evolved rapidly around the inlet region, as expected for this Graetz thermal entrance problem. The wall temperature reaches a constant value around the half pipe length, as shown in figure 5.21.

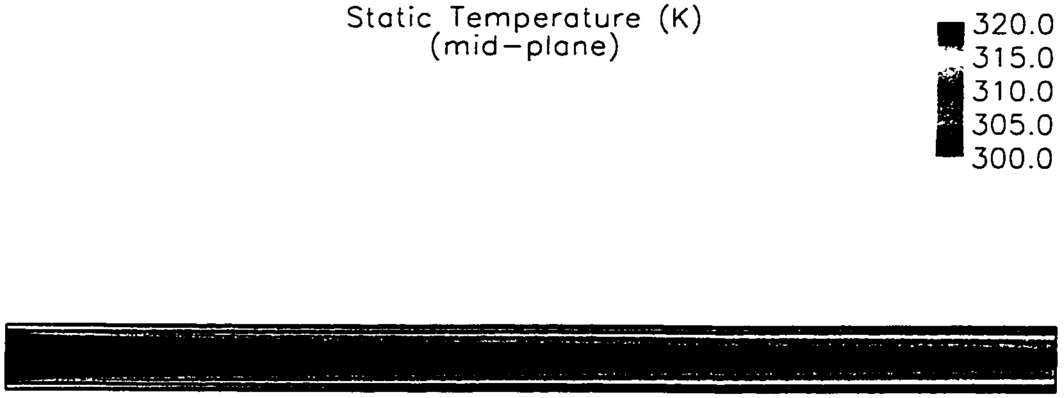

Figure 5.19: Static Temperature along the mid-plane for the 3D CHT

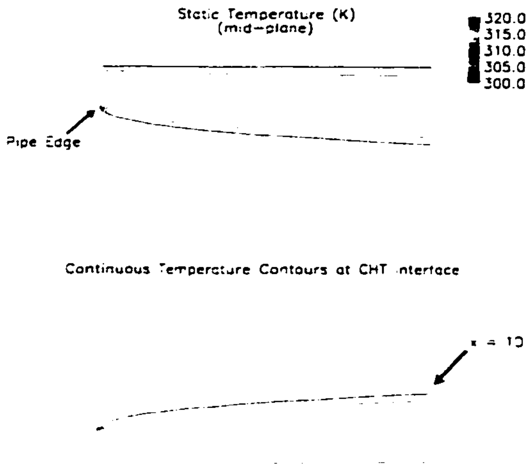

Figure 5.20: Static Temperature along the mid-plane for the 3D CHT (close-up)

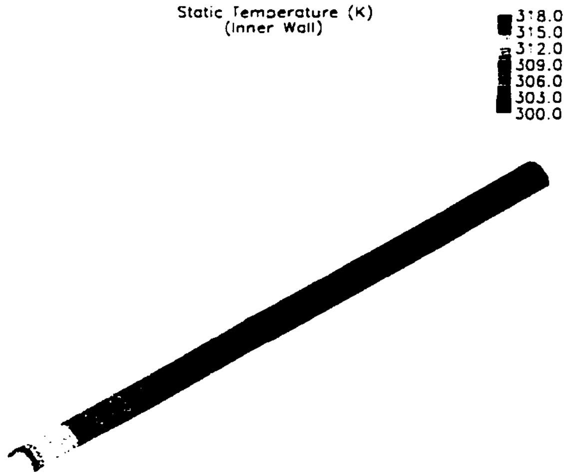

Figure 5.21: Pipe Inner Wall Temperature

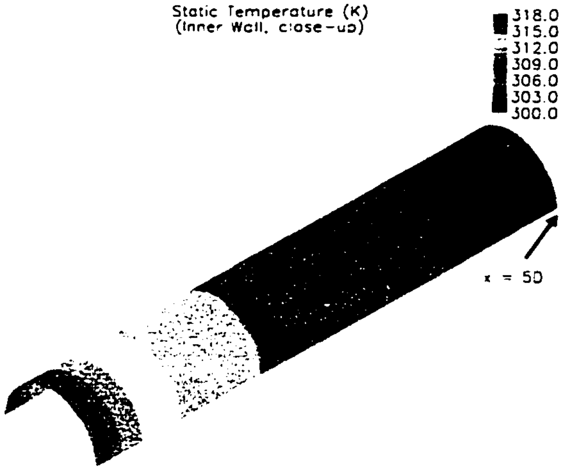

Figure 5.22: Pipe Inner Wall Temperature (close-up)

To verify the accuracy of the solution with the analytical results presented in Pozzi & Lupo [39], a non-dimensional wall temperature is computed at the pipe inner wall such as:

$$T^* = \frac{(T_{wi} - T_{in})}{(T_{wo} - T_{in})} \tag{5.7}$$

where T_{wi} is the pipe inner wall temperature, T_{wo} is the pipe outer wall temperature, and T_{in} is the inlet temperature. The results are plotted versus a non-dimensional streamwise coordinate such as:

$$x^* = \frac{(2x/D)}{Pe} = \frac{(2x/D)}{Re_D\,Pr} \tag{5.8}$$

The results of this comparison are shown in figure 5.23. The computed and analytical results agree within reasonable accuracy. The CHT implementation in FENSAP accurately computes the conjugate heat transfer for this test case.

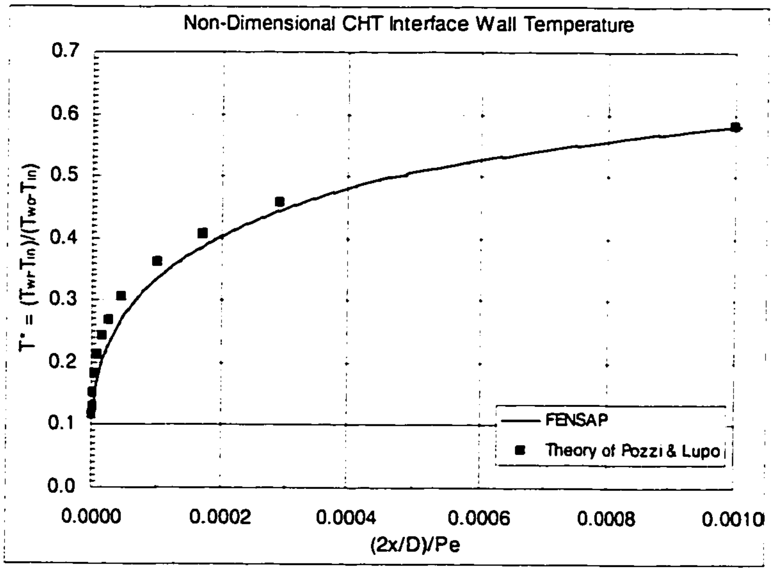

Figure 5.23: Non-dimensional CHT Interface Wall Temperature

5.4. 3D Turbulent Flow over a Nacelle Lip equipped with a Piccolo Tube System

5.4.1. Introduction

The test case involves the complex 3D anti-icing flow interaction of a piccolo tube system, impinging on a model D-duct nacelle lip placed in a low speed wind tunnel. The experimental tests were conducted in the low-speed wind tunnel ALN 1.2 x 0.9 m at Alenia-Torino. [37] These tests were part of a thesis conducted by Scarsi. [38] The computed external lip temperature distribution will be compared to the available experimental temperature distribution.

A typical business jet engine nacelle inlet is shown in figure 5.24. The full-size model tested in the wind tunnel was a simplified two-dimensional D-duct, as shown in figure 5.25, where the lip curvature effects were removed since it was judged to have minimal effect on the heat transfer distribution. The model has a span of 400 mm, a chord length of 100 mm, and a back face width of 160 mm.

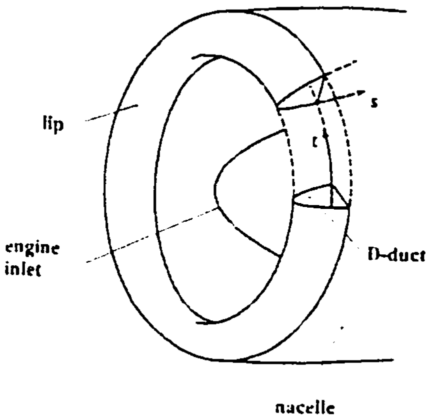

Figure 5.24: Business Jet Engine Nacelle Inlet [41]

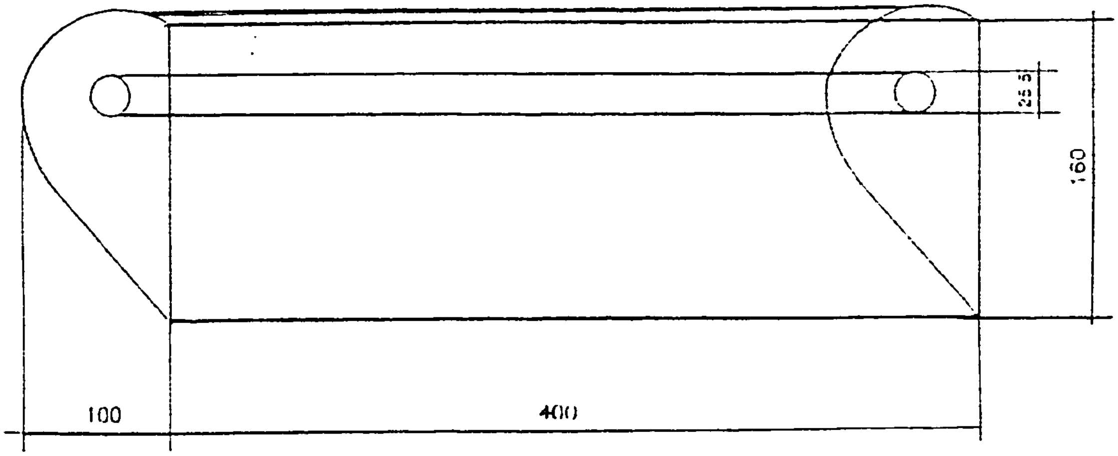

Figure 5.25: Simplified Two-Dimensional D-duct Experimental Model [38]

The piccolo tube, as shown in figures 5.25 and 5.26, has a diameter of 25.5 mm. It has one row of 25 evenly spaced holes with a pitch of 15.5 mm and a hole diameter of 3.5 mm. The impingement length of the piccolo tube holes to the internal lip skin is 47 mm.

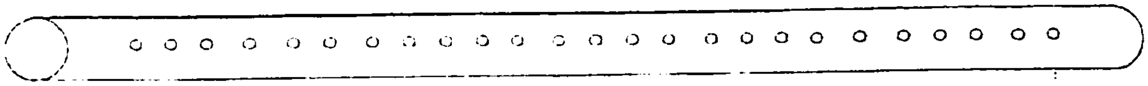

Figure 5.26: Piccolo Tube [38]

Three discharge holes with a pitch of 164 mm and a diameter of 14.6 mm are located on the back face of the D-duct, 17 mm from the top of the D-duct, as shown in figure 5.27.

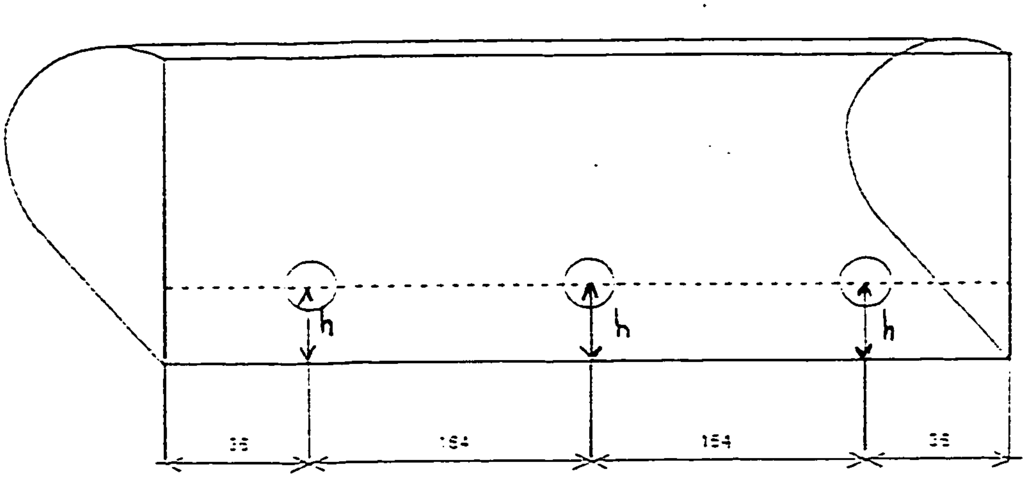

Figure 5.27: Discharge Holes Configuration [38]

The model has shielding walls after the D-duct lip to move the wake effects of the blunted model downstream of the measurement region. These walls extend downstream of the D-duct lip by 200 mm. An exploded view of the test model is shown in figure 5.28.

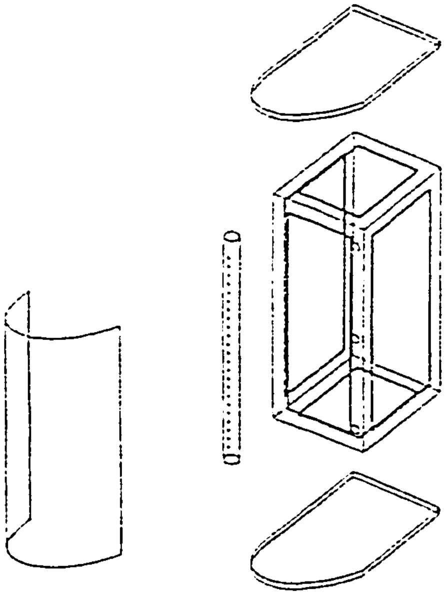

Figure 5.28: Exploded View of the Test Model [38]

The D-duct model is shown in figure 5.29 inside the Alenia low-speed wind tunnel. The range of the test conditions is:

1. Bleed Temperature: 333-403 K (± 1 K)
2. Lip Chamber Inlet Pressure: 100-400 kPa (± 10 kPa)
3. Wind Tunnel Mach Number: 0.00-0.15 (± 0.01)

To measure the lip skin external temperature, 22 thermocouples were placed on the unwrapped lip skin, as shown in figures 5.29-31. During the tests, it was noted that only thermocouples 4, 7, 12, 14, and 21 were operating normally. [38] Thus, no "real" spanwise averaging was available from the experimental results. However, the local external lip skin temperature distribution from the numerical model in this thesis will be compared with the experimental results presented by Scarsi. [38]

Figure 5.29: D-duct Model Installed in the Alenia Wind Tunnel [38]

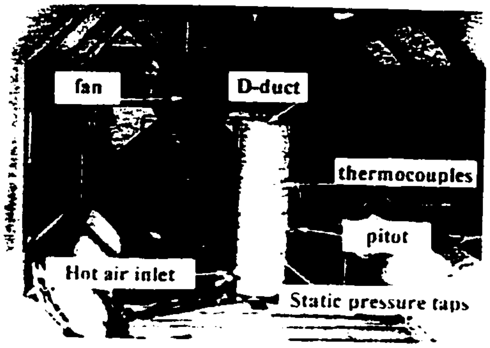

Figure 5.30: D-duct Instrumentation in the Alenia Wind Tunnel [38]

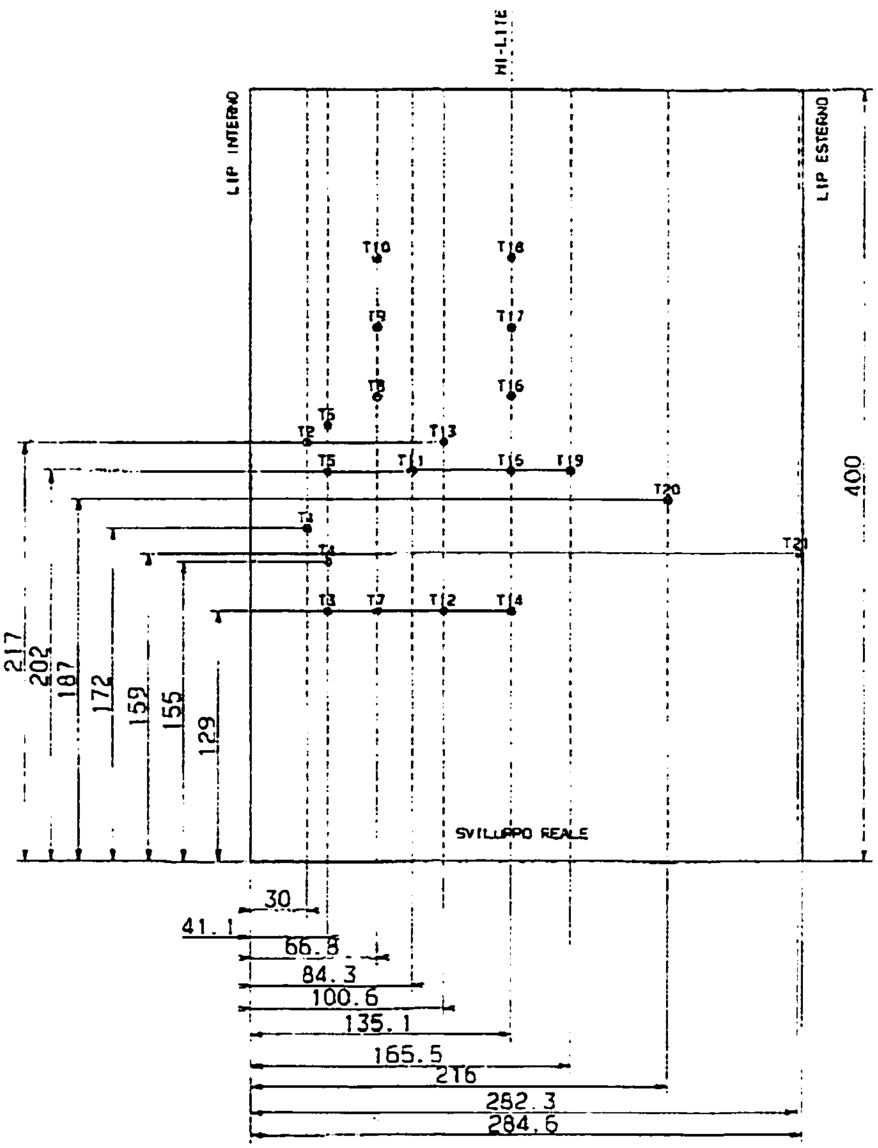

Figure 5.31: Thermocouple Locations on the External Lip Skin [38]

5.4.2. Problem Definition

The computational model presented in this thesis replicates the experimental model as closely as possible. The experimental model was placed close to the bottom half of the wind tunnel, and the downstream location is also unknown. For the computational model, it was judged to center the D-duct in the spanwise direction, since the bottom wall has minimal heat transfer effects, and to locate the back face of the D-duct at 1 m downstream of the inlet of the 2 m long wind tunnel. By taking advantage of the symmetry conditions, we can diminish the model size by half. However, a further assumption was used in the computational model: only one third of the experimental model was used (the middle part), with symmetry conditions being applied on either end of the nacelle lip geometry. The periodicity of the 25 piccolo holes to the 3 discharge holes is approximated by 8 piccolo holes and 1 discharge hole. Though this periodicity does not really exist since the discharge holes are not equally spaced between the side walls, as shown in figure 5.27, it was judged a good compromise without any scaling of the piccolo holes and the discharge holes. Next, the shielding walls downstream of the nacelle lip are continued until the exit of the wind tunnel for simplicity and to completely remove the wake interaction of a blunt object in a freestream flow. Finally, since no information on the wind tunnel wall boundary layer control was mentioned, the computational model was simulated with slip conditions on the wind tunnel walls by fixing them to wind tunnel inlet values, i.e. treating them as inlets. The computational D-duct model is shown in figure 5.32 with close-up views in figures 5.33-35.

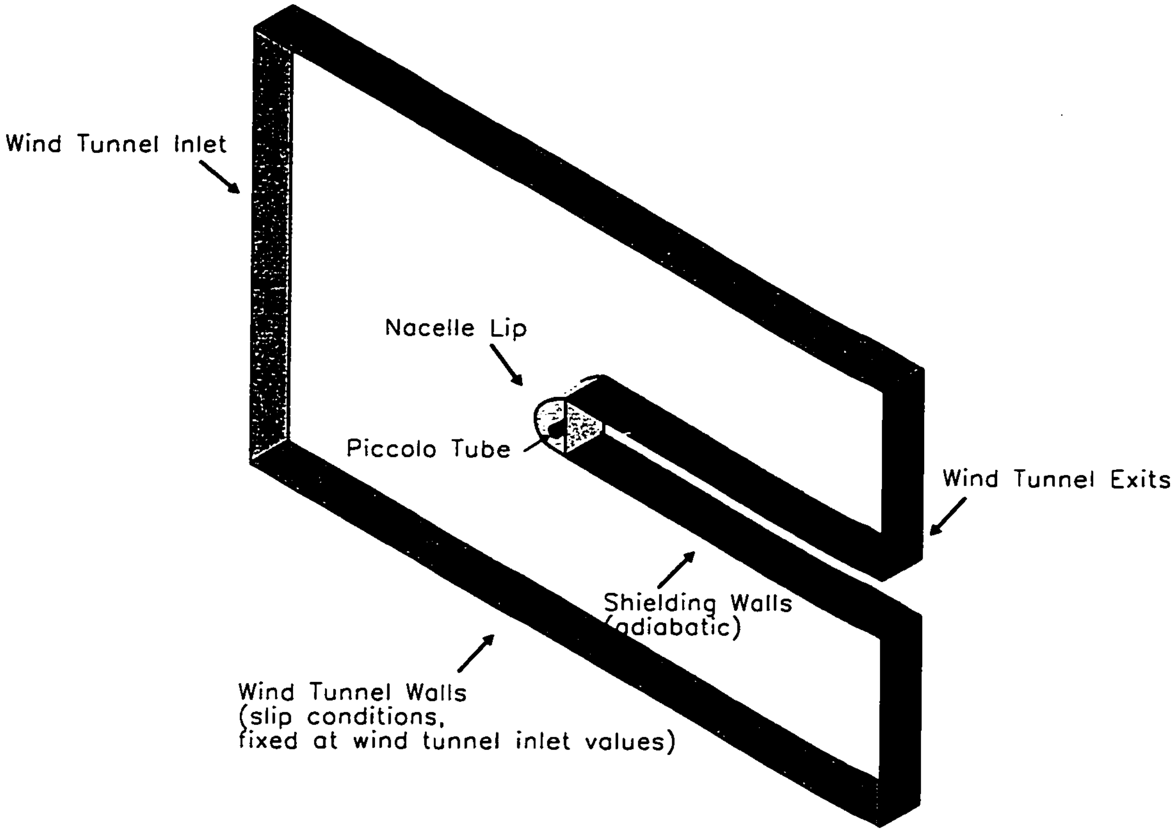

Figure 5.32: Computational Domain for the Nacelle Lip inside the Wind Tunnel

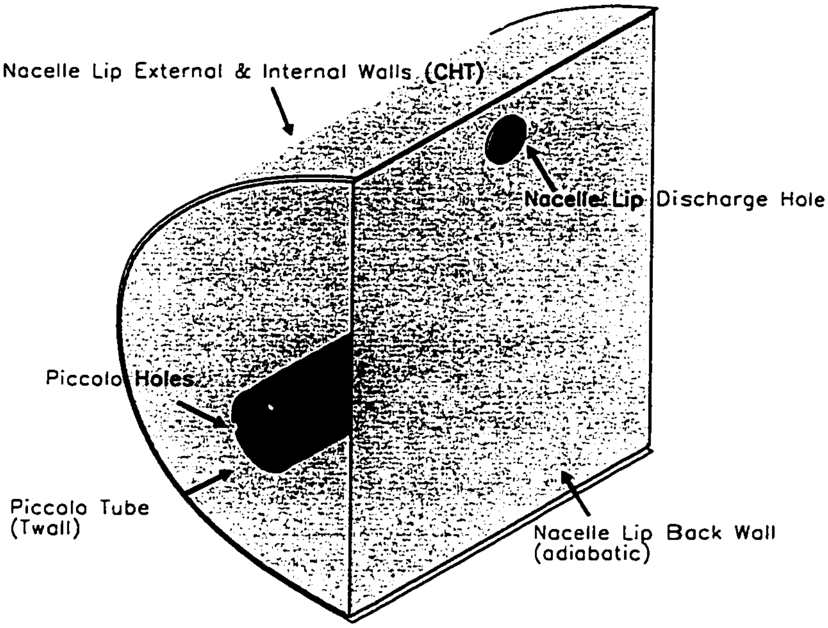

Figure 5.33: Nacelle Lip and Piccolo Tube (close-up 1)

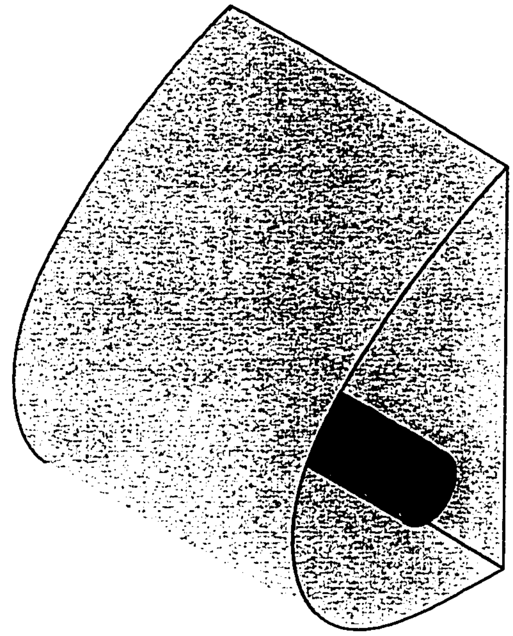

Figure 5.34: Nacelle Lip and Piccolo Tube (close-up 2)

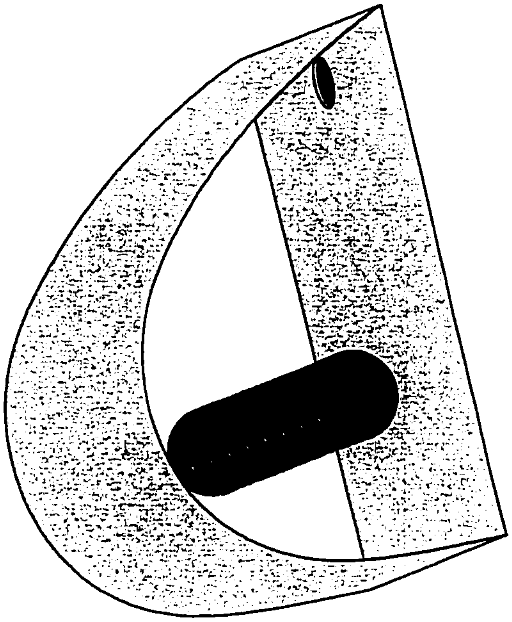

Figure 5.35: Nacelle Lip and Piccolo Tube (close-up 3)

Note that only the nacelle lip external and internal walls have CHT boundary conditions while the back face is treated as adiabatic. Thus, the solid model for the CHT computation only comprises the external and internal nacelle lip walls, and a back wall connecting them without the back face, as shown in figure 5.36. The wall thickness between the external and internal nacelle lip walls is 1.35 mm.

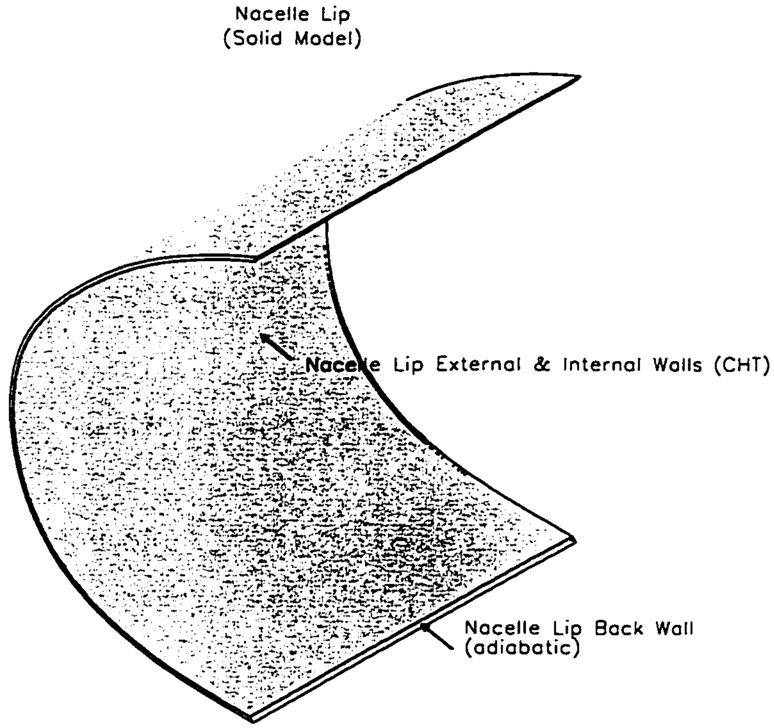

Figure 5.36: Computational Domain for the Nacelle Lip Structure

5.4.3. Boundary Conditions

It should be noted that the flow domains are disconnected in this model but are still modeled as one integral system for practicality.

The boundary conditions for the wind tunnel flow domain are as follows:

Inlet: Mach Number, $M_\infty = 0.15$

Static Temperature, $T_\infty = 288$ K

Reynolds Number, $Re_w = 5.6 \times 10^5$

Turbulence Intensity, $i_\infty = 0.5\%$

Turbulent Viscosity Ratio, $\mu_{t\infty} / \mu_{l\infty} = 1$

Exit: Static Pressure, $p_\infty = 101.325$ kPa

Wind Tunnel Walls: Slip condition, fixed at free stream inlet values

Shielding Walls: Adiabatic, no slip

Nacelle Lip External Wall: Conjugate Heat Transfer

The inlet velocity and temperature profiles in the wind tunnel are uniform, with typical wind tunnel turbulence levels. The Reynolds number is based on the free stream conditions and the back face width of the D-duct, as follows:

$$Re_W = \frac{\rho_\infty U_\infty W}{\mu_\infty} \tag{5.9}$$

The boundary conditions for the nacelle lip and piccolo tube flow domain are as follows:

Jets: Mach Number, $M_j = 1.00$

Static Temperature, $T_j = 335.8$ K

Reynolds Number, $Re_D = 7.8 \times 10^4$

Turbulence Intensity, $i_j = 3.0\%$

Turbulent Viscosity Ratio, $\mu_{tj} / \mu_{lj} = 100$

Discharge Hole: Static Pressure, $p_\infty = 101.325$ kPa

Nacelle Lip Internal Wall: Conjugate Heat Transfer

Piccolo Tube Wall: Wall Temperature, $T_w = 403$ K

The inlet velocity and temperature profiles for the piccolo jets are uniform with typical jet turbulence levels. The piccolo holes are assumed to be choked, thus, the temperature and pressure are deduced from the isentropic relations and the total quantities inside the tube, where: $T_{tj} = 403$ K and $p_{tj} = 200$ kPa for the test conditions used. Although the characteristics allow the pressure to be imposed at the piccolo holes, this was not done since the flow solver did not react properly to this boundary condition. Thus, the static pressure of the piccolo holes was not properly controlled but at convergence was only 8% above the isentropic value, but still within the experimental uncertainty of the pressure measurement. To reduce this inconsistency, the back pressure of the discharge hole could have been reduced but it was not since it cannot be below the back pressure of the wind tunnel. The piccolo tube wall temperature was set at the tube's total temperature since the flow inside the tube is very low and any convection effects from the recirculating flow around the exterior of the tube was neglected. Finally, no blockage effects were taken into account at the piccolo holes for the choked condition. The Reynolds number is based on the jet conditions and the piccolo hole diameter, as follows:

$$\mathrm{Re}_D = \frac{\rho_j U_j D}{\mu_j} \tag{5.10}$$

The boundary conditions for the solid domain are as follows:

Nacelle Lip External and Internal Walls: Conjugate Heat Transfer

Nacelle Lip Back Wall: Adiabatic

The wall metal is duralumin, with the following properties at 20°C:

Density, $\rho_s = 2{,}787$ kg/m^3

Thermal Conductivity, $k_s = 164$ W/m-K

Specific Heat, $c_s = 883$ W-s/kg-K

The wall thermal conductivity was actually modeled as a function of temperature, with a table provided as an input. The table values can be found in Holman. [42]

5.4.4. Computational Grids

The test case used an unstructured grid for the fluid domain and a structured grid for the solid domain. Through anisotropic mesh adaptation, the best fluid grid was obtained for a specified target number of nodes. The variable used for the adaptation error estimation was the Mach number. Mesh adaptation for this test case was essentially needed since the initial grid was very coarse and did not provide good convergence levels, but was only used to obtain a first guess adiabatic solution. The target number of nodes estimated was chosen to provide a good resolution of the effects while being able to obtain a solution with a reasonable computing time. Near-wall grid spacing was also evaluated during the mesh adaptation cycles to ensure a valid range of y^+ values at the first-node-off-the-wall. The external flow is a boundary layer flow with a stagnation point, while the internal flow is a constrained impingement flow. Nonetheless, the average y^+ is approximately 45 for the external flow, and approximately 25 for the internal flow, both in a reasonably valid range for near-wall turbulence modeling.

The initial fluid grid had 121,716 nodes, as shown in figure 5.37 with a close-up view in figure 5.38. The final adapted fluid grid had 250,444 nodes, as shown in figure 5.39, with close-up views in figures 5.40 and 5.41. Notice the piccolo jet resolution and the boundary layer resolution around the nacelle lip on the adapted grid, obtained through a series of 5 solution-adaptation global cycles (some adiabatic, some CHT). The solid grid had 23,205 nodes and was not adapted, but was clustered in the wrap direction near the impingement region.

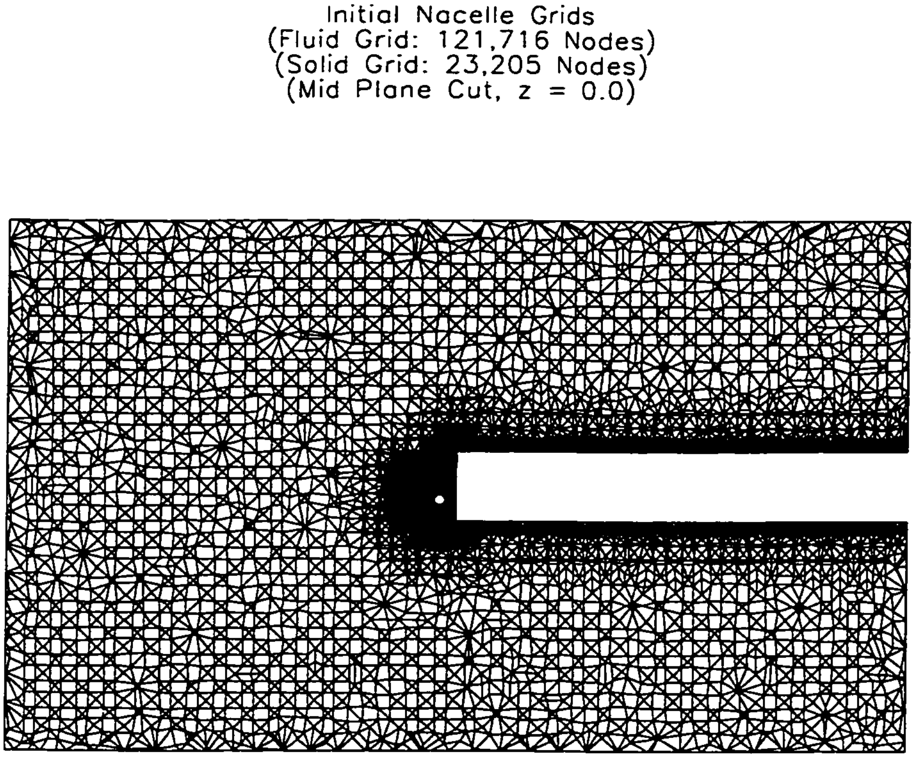

Figure 5.37: Initial Grids for the Nacelle Lip

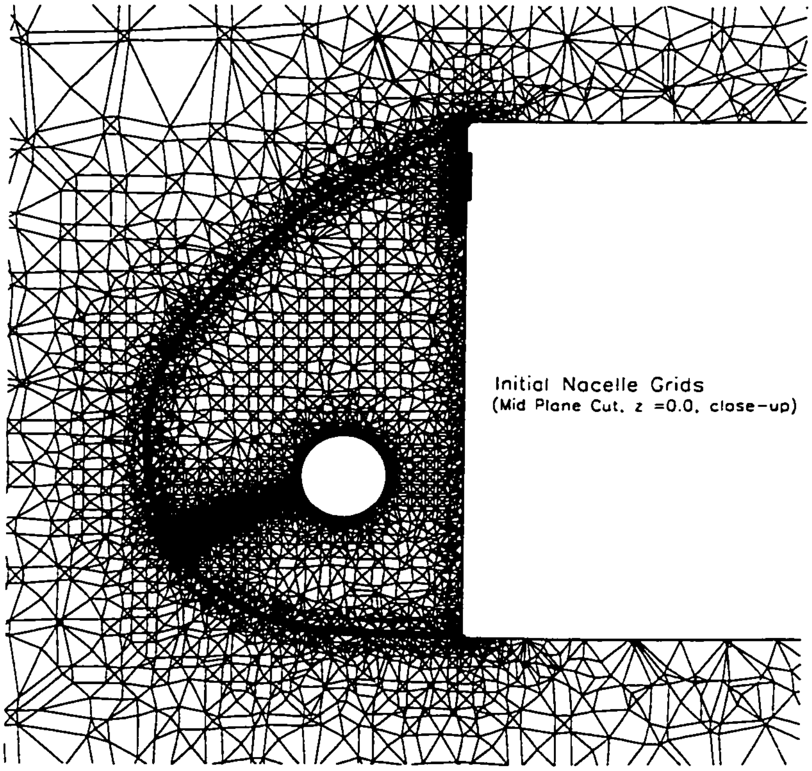

Figure 5.38: Initial Grids for the Nacelle Lip (close-up)

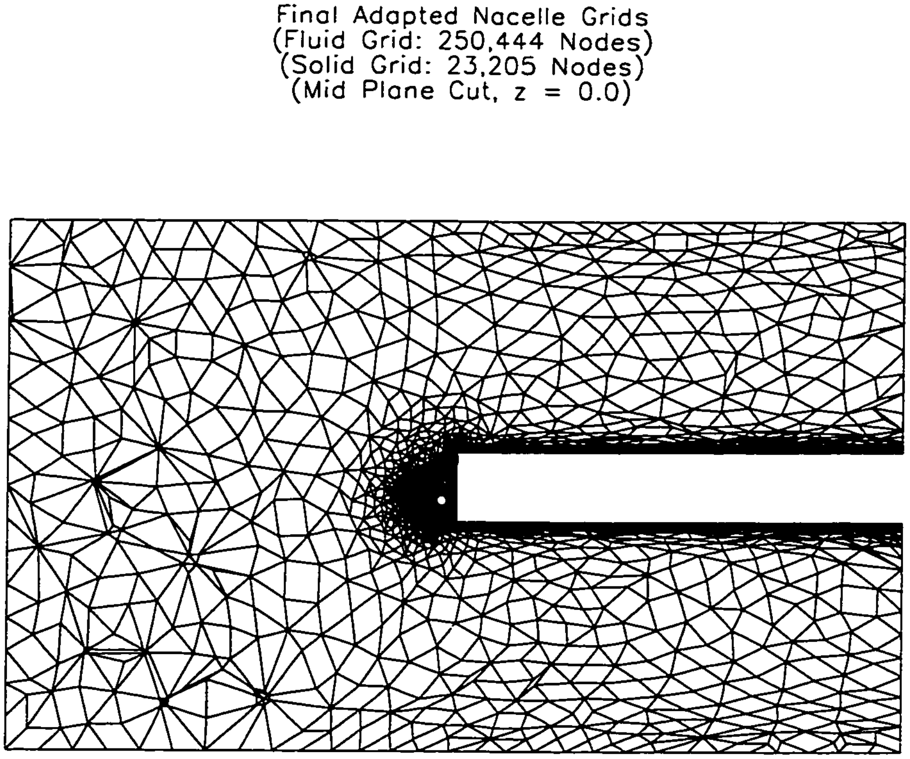

Figure 5.39: Final Adapted Grids for the Nacelle Lip

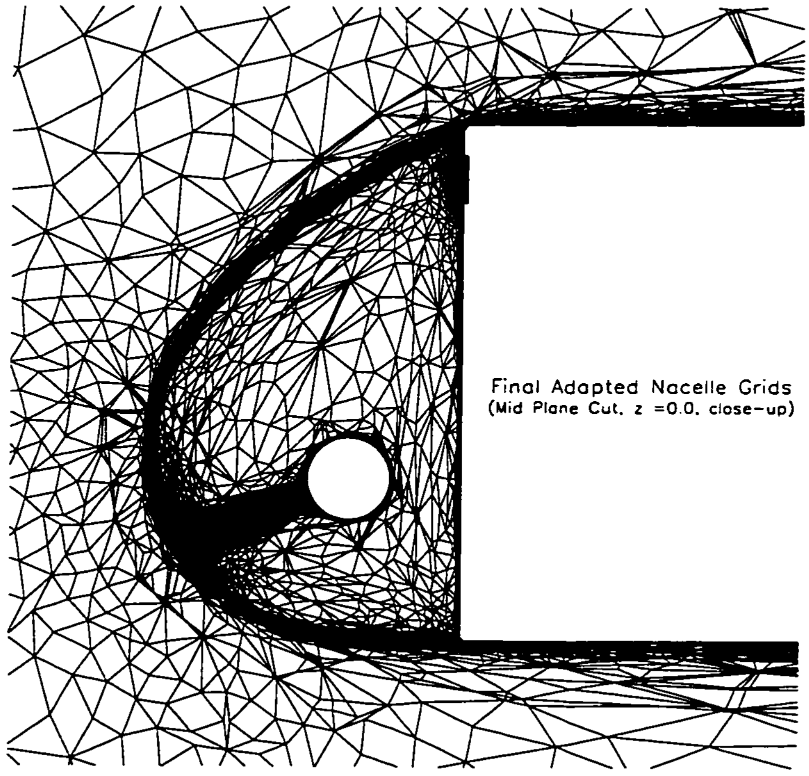

Figure 5.40: Final Adapted Grids for the Nacelle Lip (close-up 1)

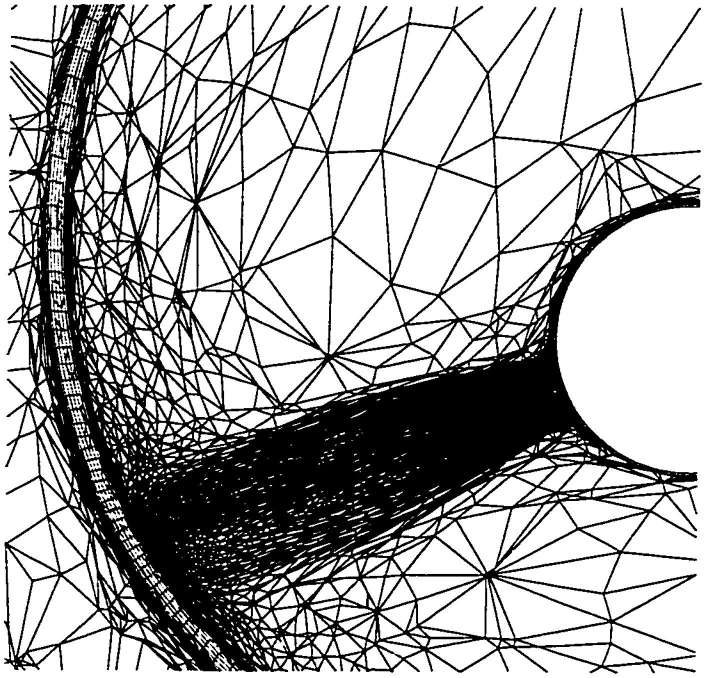

Figure 5.41: Final Adapted Grids for the Nacelle Lip (close-up 2)

The interface between the fluid grid and the solid grid had non-matching node connectivity, as shown in figure 5.41. The external surface fluid grid is stretched spanwise since there are not many gradients for this boundary layer flow along the surface, while the internal surface fluid grid picks up the impinging jet features. The grid densities of the final adapted fluid grid for the external and internal lip walls are shown in figures 5.42 and 5.43, respectively. The grid densities of the solid grid for the external and internal lip walls are nearly identical since it is a structured grid, thus only the internal lip wall grid is shown in figures 5.44. The grid densities on both sides of the interface are in the range of 1:1 for nodes but, 2:1 or 3:1 for faces. This grid density variation does not pose a problem for the CHT algorithm since the residual coupling is done consistently with the virtual grid routines. There is only an increase in the coupling time.

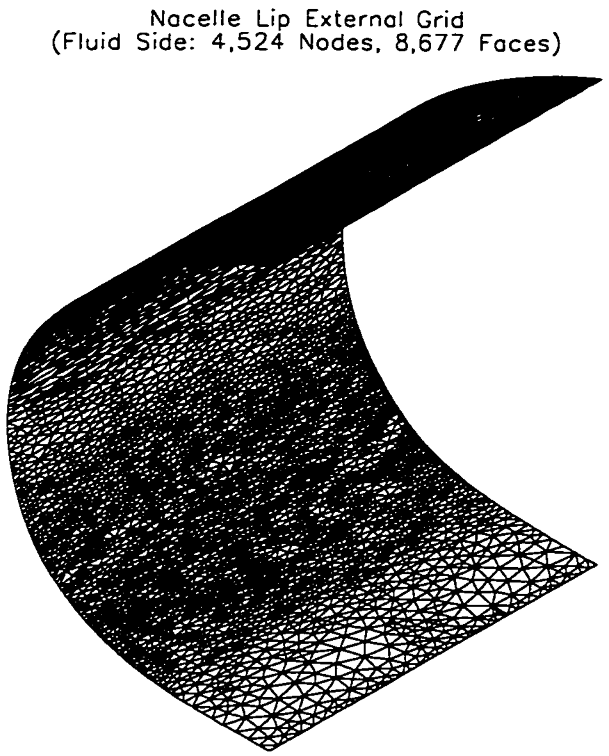

Figure 5.42: Nacelle Lip External Surface Fluid Grid

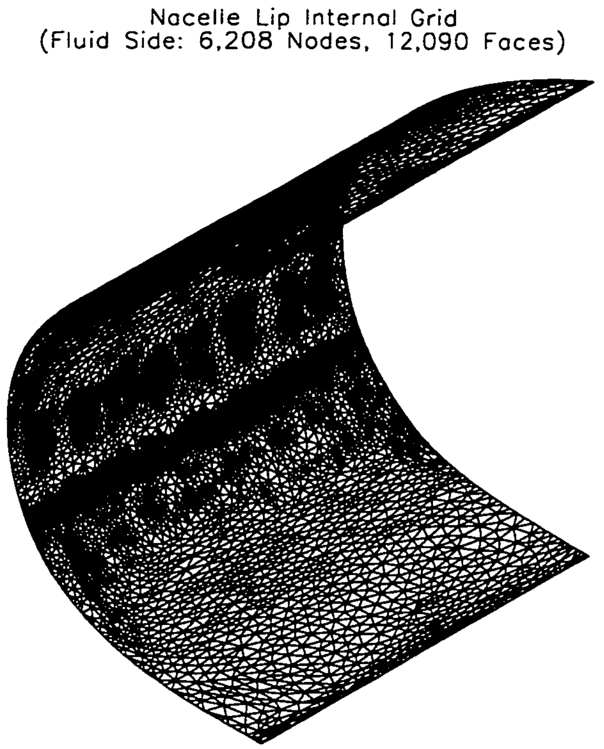

Figure 5.43: Nacelle Lip Internal Surface Fluid Grid

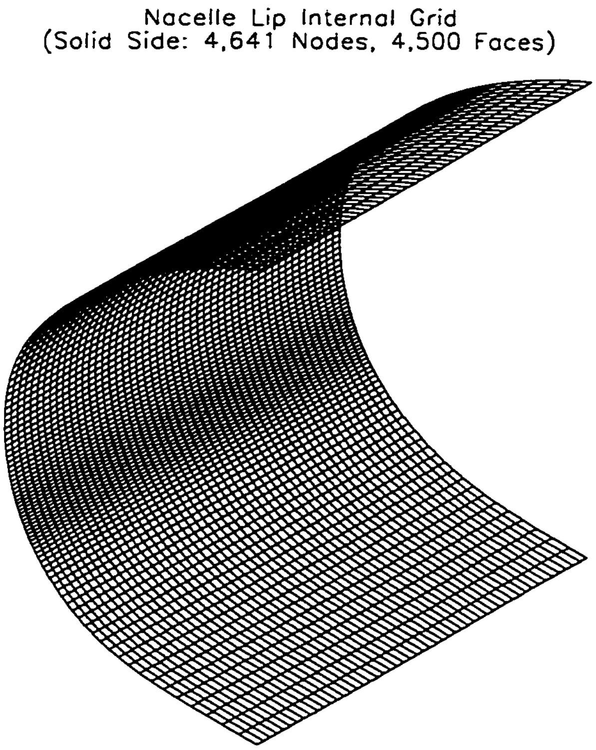

Figure 5.44: Nacelle Lip Internal Surface Structure Grid

5.4.5. Results & Discussion

The convergence of this test case is shown in figure 5.45. To prove the robustness of FENSAP, the test case was started from no initial solution with 4 cycles of artificial dissipation since the adapted grid had very skewed elements. The final cycle did not have a residual reduction of 3 orders of magnitude, but converged to an absolute value of 10^{-8} with a residual reduction close to 2 orders of magnitude. Although the Energy equation residual was not reduced by 3 orders of magnitude nor was it below 10^{-8}, it was still judged to be converged. The convergence of the external and internal lip average wall temperatures is shown in figure 5.46. The average wall temperatures have almost settled down and this concurs with the CHT L_2 norm being below 10^{-5}. While the energy equation residual exhibited some problems converging, the overall solution is good and it is believed that the problem is due to a local phenomenon. There is no need to continue iterating on the overall problem in such a case.

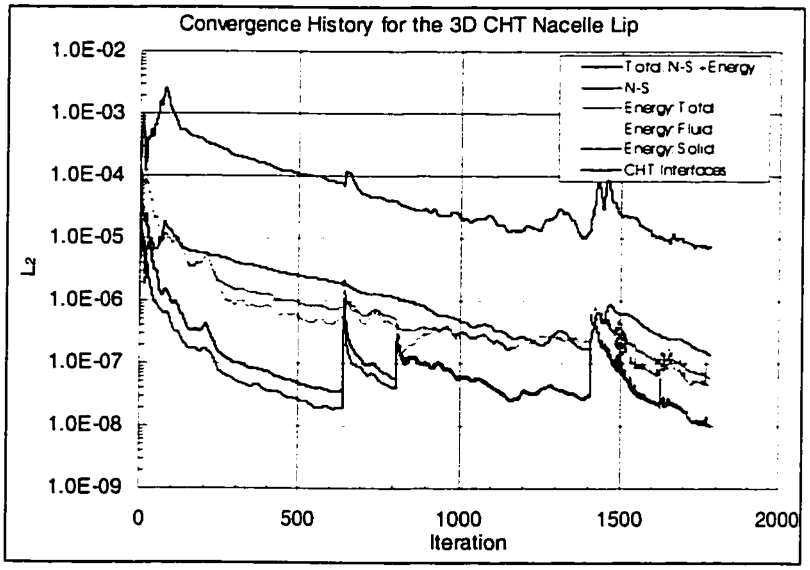

Figure 5.45: Convergence History for the 3D CHT Nacelle Lip

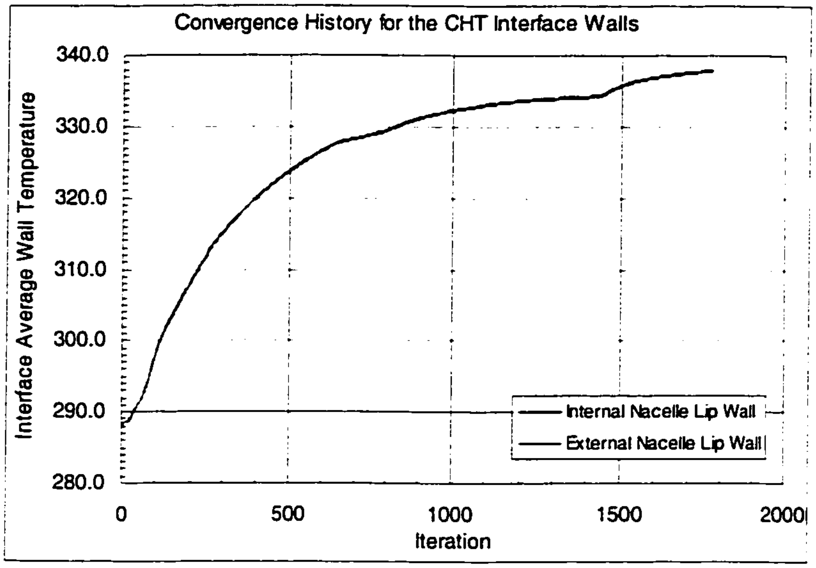

Figure 5.46: Convergence History for the CHT Interface Walls of the Nacelle Lip

The Mach number along the mid-plane in the nacelle lip is essentially low everywhere, except for the impinging jet core, as shown in figures 5.47 and 5.48. The flow structure in the nacelle lip coming from the impinging jets is highly complex and three-dimensional, but repeats closely at every jet. This is clearly shown through streamlines, colored by Mach number, originating from the piccolo holes as shown in figures 5.49 and 5.50. Regions of high Mach number are neighbored by regions of recirculation and low Mach number between the piccolo tube and the back wall. The interaction of the jets between themselves is another phenomenon found here. However, the impact is reduced since the piccolo holes are choked, closely spaced, and the L/D of the impinging jet is around 13.4 for this configuration, a relatively high value for heat transfer by impinging jets.

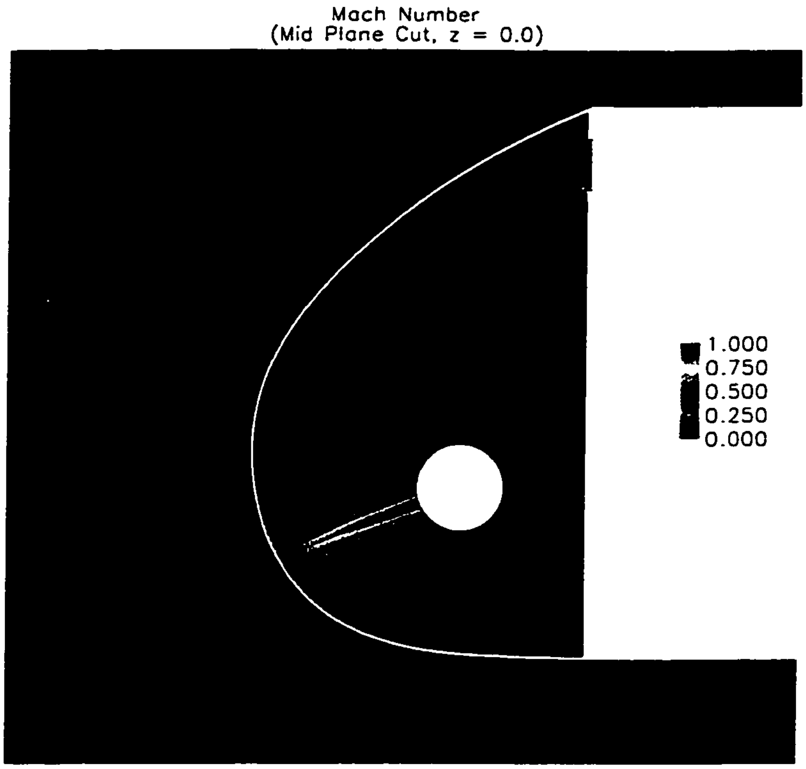

Figure 5.47: Mach Number along the mid-plane for the Nacelle Lip

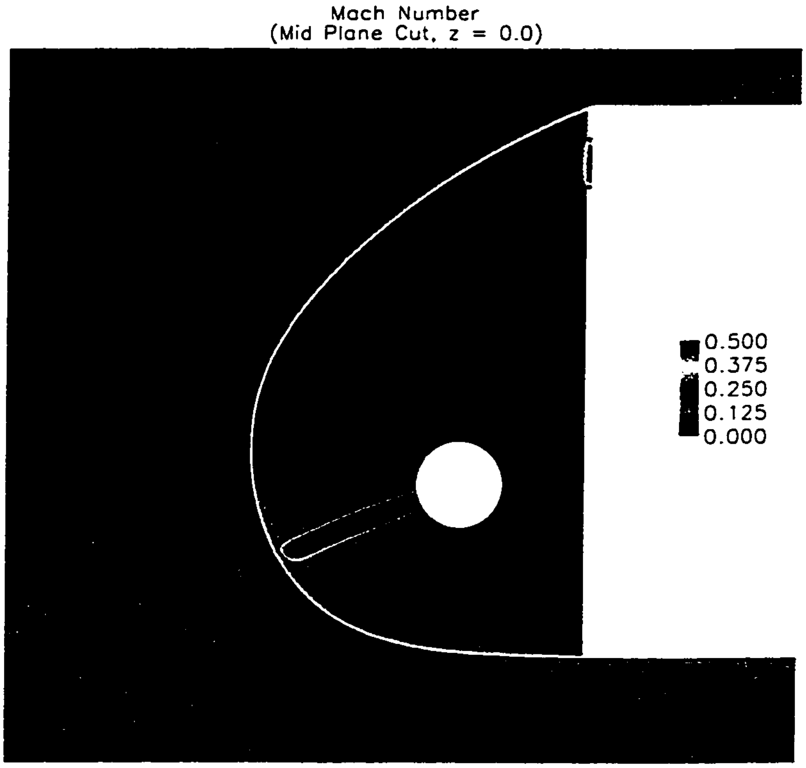

Figure 5.48: Mach Number along the mid-plane for the Nacelle Lip (reduced scale)

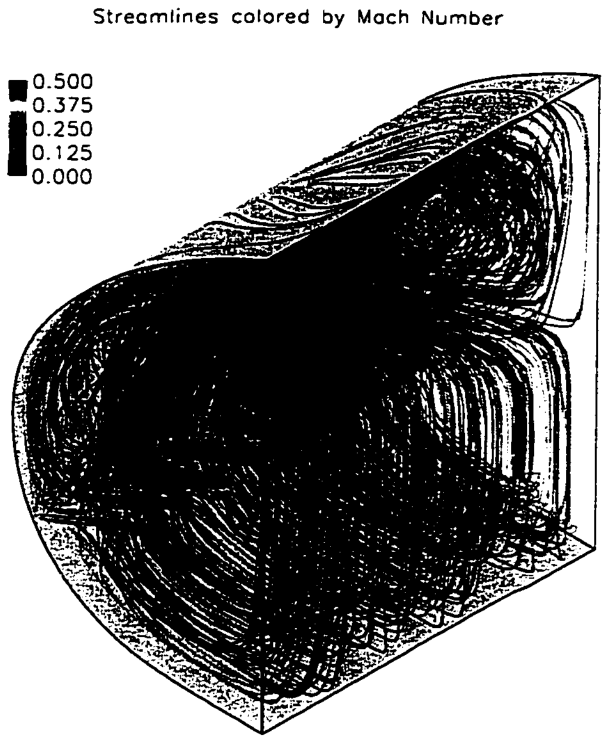

Figure 5.49: Streamlines colored by Mach Number for the Nacelle Lip (rear view)

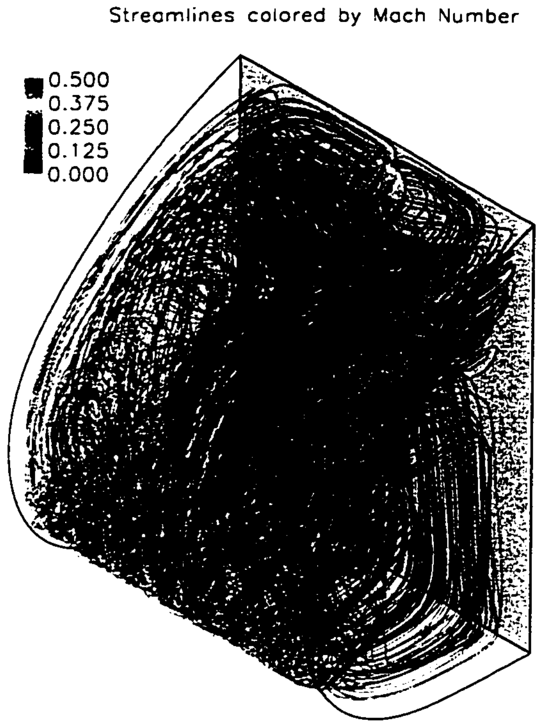

Figure 5.50: Streamlines colored by Mach Number for the Nacelle Lip (front view)

The static and total pressures along the mid-plane are shown in figures 5.51 and 5.52, respectively. The total pressure losses incurred during the free-shear portion of the expanding jet as it comes out of the piccolo holes are clearly shown in figure 5.52. What these two figures also show is that the pressure is nearly uniform in the nacelle lip after impingement.

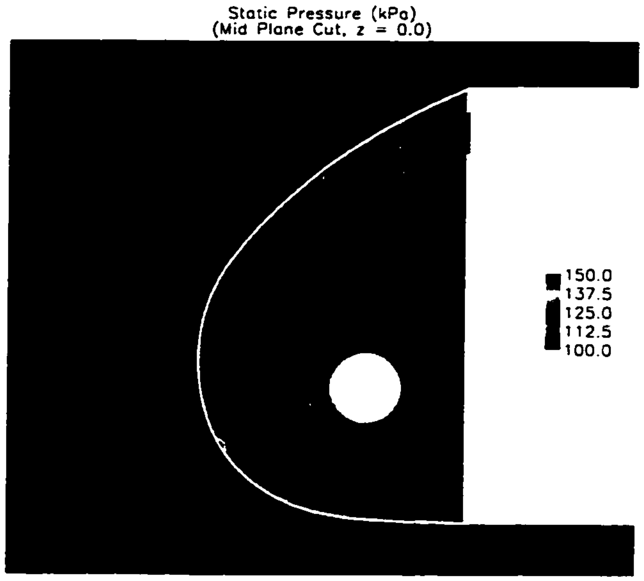

Figure 5.51: Static Pressure in the Nacelle Lip

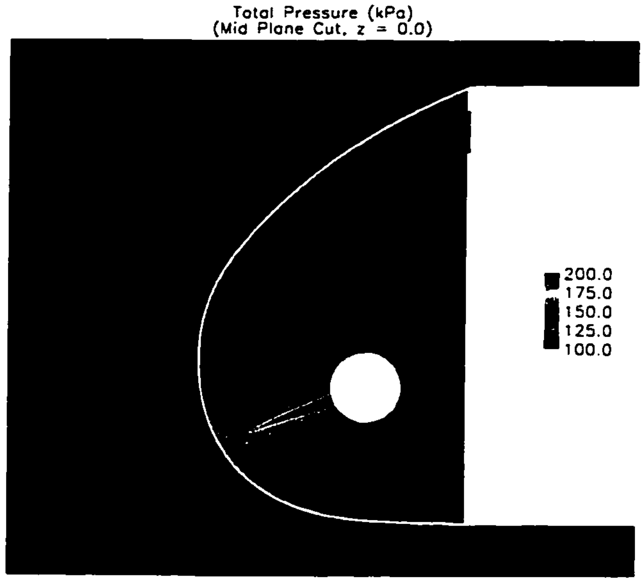

Figure 5.52: Total Pressure in the Nacelle Lip

The static and total temperatures along the mid-plane are shown in figures 5.53 and 5.54, respectively. Notice the total temperature decrease along the axis of the jet, typical for a free-shearing jet. The convection along the piccolo tube also caused more heat to be convected with the jet onto the internal lip wall, as shown in figures 5.53 and 5.54.

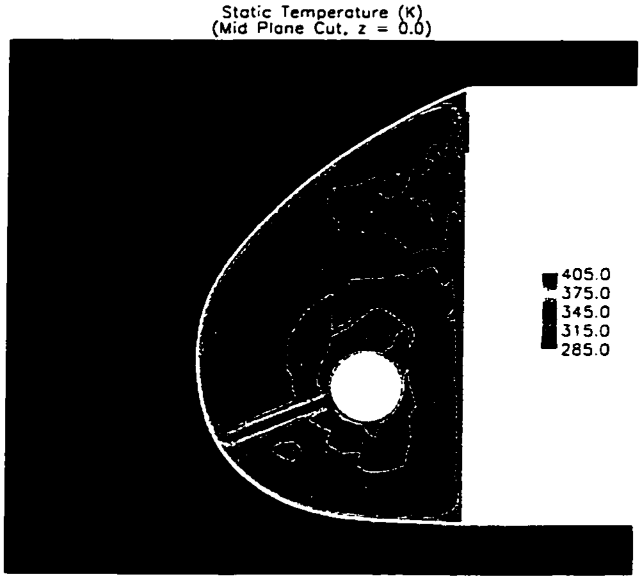

Figure 5.53: Static Temperature in the Nacelle Lip

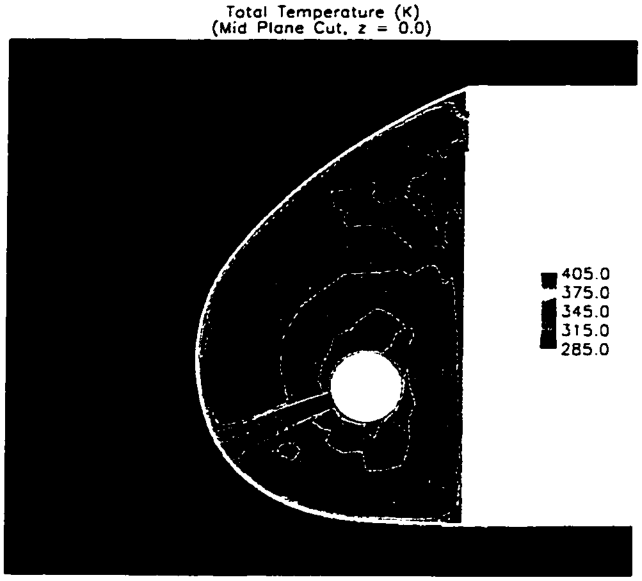

Figure 5.54: Total Temperature in the Nacelle Lip

Finally, the external and internal wall temperature distributions are shown in figures 5.55 and 5.56, respectively. There is not much difference in both figures since the metal is nearly isothermal across its small thickness. However, the impingement pattern is clearly visible for every jet. There is also not much spanwise temperature distribution along the nacelle lip except at the impinging region, where the peak to valley temperature difference is around 10 K.

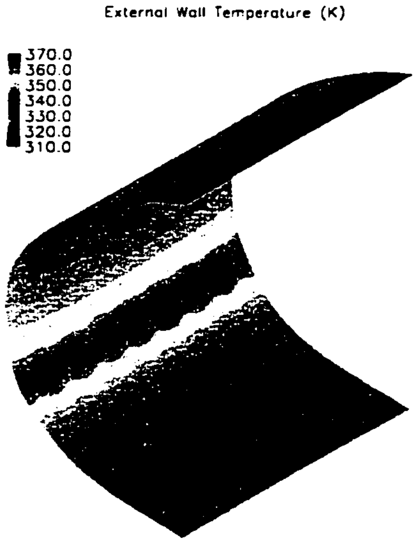

Figure 5.55: External Wall Temperature for the Nacelle Lip

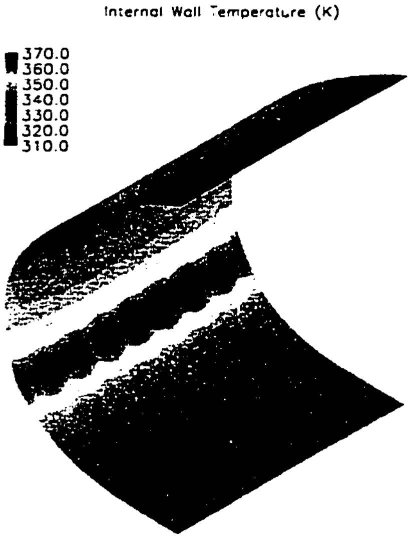

Figure 5.56: Internal Wall Temperature for the Nacelle Lip

The computed external wall temperature for the nacelle lip is compared with the experimental results provided by Scarsi, as shown in figure 5.57. The spanwise temperature variation of the computed results is compared to the thermocouple temperatures. FENSAP is able to predict the impingement region temperature (wrap distance = -35 mm) quite well. The bottom nacelle lip region temperature distribution is also well captured after the impingement (-135 mm < wrap distance < -35 mm). The jet heat transfer is properly confined in this recirculating flow region. At the external stagnation point (wrap distance = 0 mm), the external heat load is under-predicted resulting in a low wall temperature. The top nacelle lip region temperature distribution is not that good (0 mm < wrap distance < 150 mm). The far end point is totally off from the experimental value. Recall in chapter 4 that for the impinging type of flow, FENSAP can have difficulties capturing the redeveloping boundary layer along the wall after impingement, thus the internal heat load can be under-predicted resulting in a low wall temperature.

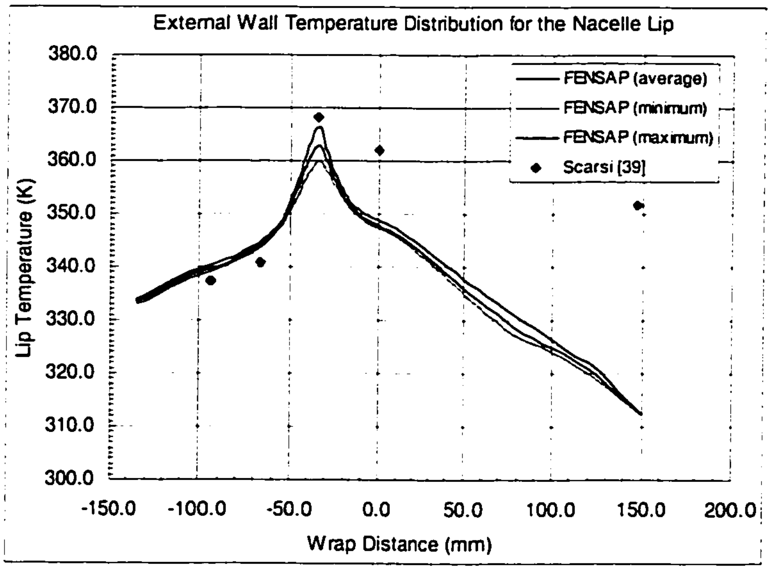

Figure 5.57: External Wall Temperature Distribution for the Nacelle Lip

One should also recall that only the lower-span thermocouples were working properly during the experiments conducted by Scarsi, since the other thermocouples were creating aerodynamic disturbances. [38] Scarsi also mentioned that in certain zones on the nacelle lip they observed transition phenomena from laminar to turbulent flow at the location of some of the thermocouples. [38] FENSAP assumes no transition point and the flow is completely turbulent. Thus, if the external flow were actually modeled with a laminar flow at the stagnation point developing into a turbulent flow along the surface, a reduction in the external heat load would ensue. This would lead to higher skin temperatures.

Also, how good are the experimental results presented by Scarsi? Can the point at the far end of the nacelle lip be measured wrong? Can there be any effects of the discharge hole flow in this region? Can the experimental weld setup between the shielding walls and the nacelle lip walls provide some shielding effect from the freestream flow, thus reducing the external heat load and augmenting the nacelle lip temperature? Can the far end thermocouple be malfunctioning?

Another possible source of error for this test case is the inability of the k-e turbulence model to correctly predict the flow structure and heat transfer for this complex three-dimensional flow. Improving or even changing turbulence model is definitely an avenue that needs to be looked at, but was not tested in this thesis because it was not part of the scope nor was another turbulence model available within FENSAP during the time period of the present thesis.

Using mesh adaptation to keep refining the grid to increase the amount of nodes can be tried out but at the expense of long solution times. This was not the interest of this study. The solution provided in this thesis is of valid engineering interest.

Finally, the modeling used for this test case is to consider the back face of the nacelle as adiabatic when it should be conducting. The shielding walls after the D-duct provide for an expanding jet coming out of the discharge holes. Thus, the heat transfer along the back face on the outside will be very low, while on the inside the flow follows mostly the back face so, the heat transfer will be higher. There will be heat transfer convected away and influencing the nacelle lip wall temperature. This can affect the overall balance of heat transfer for the whole nacelle lip.

6. Discussion

6.1. Conclusion

A conjugate heat transfer capability has been developed and embedded within a CFD code, FENSAP. The approach is a multi-domain one, whereby the fluid energy equation and the solid energy equation are solved simultaneously in a fully-implicit manner where each fluid and solid domains have their own meshes. The proposed CHT methodology has been fully integrated within a 3D framework that supports 3D structured, unstructured, and hybrid meshes, with mismatched node connectivity and with non-uniform grid densities across interfaces. Thus, the use of anisotropic mesh adaptation in the fluid domain becomes possible and greatly improves the quantitative nature of the flow predictions, and hence, heat transfer results.

The heat transfer validation for both laminar and turbulent flows has been conducted. For each test case, the results have been compared to available open literature results for simple geometries, and the agreement was excellent. The CHT validation is assessed with three cases: a blunt flat plate flow, a fully-developed pipe flow, and a complex piccolo tube system flow in a 3D nacelle lip. Open literature results were available for all test cases, and the agreement was shown to be within reasonable accuracy.

From the piccolo tube test case, it can be concluded that the proposed method can be used as a reliable and cost-effective tool for the analysis and design of thermal anti-icing devices. Different geometrical configurations can rapidly be tested and even optimized, without the need for extensive and expensive experimental testing.

The stability and robustness of the CHT algorithm developed allows for a CHT computation to be tackled from the start instead of performing a traditional adiabatic or constant wall temperature computation. The extra cost in terms of computational time and structure meshing is worth investing, but the choice belongs to the user.

6.2. Future Work

The CHT capabilities of FENSAP can easily be extended to the prediction of the thermal field of cooled gas turbine components, such as: blades, shrouds, and disks. The automotive industry can also benefit from a CHT system to analyze brake systems, and automotive under-hood cooling. Such CAD-complex analyses require a robust flow solver, a stable CHT algorithm, and accurate heat transfer modeling. The CHT methodology developed couples, in the spirit of concurrent engineering, the aerodynamic and thermal analyses into an integral system for air-cooled or air-heated components. The future ought to see the further application of the approach to these interesting situations.

The continuing need for better turbulence modeling has to be addressed, since most of the cooling or heating techniques involve low-Reynolds flows. Using a higher order turbulence model with a scalar transport model for the energy variable should be investigated. Transition modeling also needs to be addressed so that the heat transfer for blade leading edges or nacelle leading edges can be better predicted. The inclusion of a roughness model can also be of great importance when tackling aerofoil heat loads in a turbine gaspath, or for nacelles under icing conditions. Finally, a radiation model would also be beneficial for the icing heat load predictions.

The current CHT implementation is limited to a single fluid and a single solid domain. The use of multiple solid layers with different thermal conductivities, such as Thermal Barrier Coatings (TBC) on blades, cannot be supported at this moment, but could be included in future modeling. The heat loss through a film of water or a layer of ice on a wing leading edge or a nacelle lip also cannot yet be simulated with the current CHT implementation. Further programming would be required to include a physical film model within the CFD code, but this becomes cumbersome for the architecture of the code.

All of the presented results were predicted at steady-state conditions. Although unsteady heat transfer of cooled components is too time consuming to tackle today, an unsteady validation of the CHT algorithm characteristics still needs to be assessed. Thermal transient blade and disk stress analysis are of great importance in the gas turbine industry, and unsteady heat transfer analyses will become feasible in the near future.

The present CHT algorithm supports the feature of performing multiple energy equation loops for every Navier-Stokes equation loops since it speed-up the convergence of the global energy equation. A detailed study on the convergence characteristics of this feature needs to be addressed for both Steady-State and Unsteady-State computations.

Automation of the CHT setup is an issue that needs to be continuously addressed. Currently, the interpolation files used in the coupling routines are generated with the provided grids. The degree of grid mismatch can affect the interpolation accuracy. Perhaps the latter could be automated at the grid creation level so that the interpolation can be done on the native-CAD description and not on the numerical grids.

References

1. Croce, G., Habashi, W.G., Guevremont, G., and Tezok, F., "3D Thermal Analysis of an Anti-Icing Device using FENSAP-ICE", AIAA Paper 98-0193, January 1998

2. Croce, G, Beaugendre, H., and Habashi, W.G., "CHT3D: FENSAP-ICE Conjugate Heat Transfer Computations with Droplet Impingement and Runback Effects", AIAA Paper 2002-0386, January 2002

3. Croce, G., and Habashi, W.G., "Thermal Analysis of Wing and Nacelle Anti-Icing Devices", Computational Analysis of Convection Heat Transfer, Chapter 10, pp. 409-432, Wessex Institute of Technology Press, 2000

4. Funaro, D., Quarteroni, A., and Zanolli, P., "An Iterative Procedure with Interface Relaxation for Domain Decomposition Methods", SIAM Journal of Numerical Analysis, Vol. 25, No. 6, pp. 1213-1236, 1988

5. Giles, M.B., "Stability in Analysis of Numerical Interface Conditions in Fluid-Structure Thermal Analysis", International Journal for Numerical Methods in Fluids, Vol. 25, pp. 421-436, 1997

6. Imlay, S.T., Soetrisno, M., and Roberts, D.W., "Coupled Flow and Heat Transfer Analysis using Structured-Unstructured Grids", AIAA Paper 96-0622, January 1996

7. Montenay, A., Paté, and Duboué, J.M., "Conjugate Heat Transfer Analysis of an Engine Internal Cavity", ASME Paper 2000-GT-282, May 2000

8. Bohn, D., Bonhoff, B., Schönenborn, H., and Wilhelmi, H., "Validation of a Numerical Model for the Coupled Simulation of Fluid Flow and Diabatic Walls with Application to Film-cooled Gas Turbine Vanes", VDI-Berichte 1186, pp. 259-272, 1995

9. Bohn, D., Bonhoff, B., Lang, G., and Schönenborn, H., "Determination of Thermal Stress and Strain Based on a Combined Aerodynamic and Thermal Analysis for a Turbine Nozzle Guide Vane", ASME Paper 95-CTP-089, 1995

10. Bohn, D., Bonhoff, B., and Schönenborn, H., "Combined Aerodynamic and Thermal Analysis of a Turbine Nozzle Guide Vane", IGTC Paper 108, Proceedings of the 1995 Yokohana International Gas Turbine Congress, 1995

11. Bohn, D., Volker, J.B., and Kusterer, K.A., "3-D Conjugate Flow and Heat Transfer Calculations of a Film-Cooled Turbine Guide Vane at Different Operation Conditions", ASME Paper 97-GT-23, 1997

12. Kao, K.H., and Liou, M.S., "Application of Chimera/Unstructured Hybrid Grids Conjugate Heat Transfer", AIAA Journal, Vol. 35, No. 9, September 1997

13. Han, Z.H., Dennis, B.H., and Dulikravich, G.S., "Simultaneous Prediction of External Flow-Field and Temperature in Internally Cooled 3-D Turbine Blade Material", ASME Paper 2000-GT-253, May 2000

14. Thakur, S., and Wright, J., "Conjugate Heat Transfer in a Gas Turbine Blade Trailing-Edge Cavity", AIAA Paper 2002-0496, January 2002

15. Rigby, D.L., and Lepicovsky, J., "Conjugate Heat Transfer Analysis of Internally Cooled Configurations", ASME Paper 2001-GT-405, 2001

16. Baruzzi, G.S., Habashi, W.G., Guevremont, G, and Hafez, M.M., "A Second Order Finite Element Method for the Solution of Transonic Euler and Navier-Stokes Equations", International Journal for Numerical Methods in Fluids, Vol. 20, pp. 671-693, 1995

17. Jones, W.P. and, Launder, B.E., "The Prediction of Laminarization with a Two-Equation Model of Turbulence", International Journal of Heat and Mass Transfer, Vol. 15, pp. 301-314, 1972

18. Van Driest, E.R., "The Problem of Aerodynamic Heating", Aerodynamics Engineering Review, Vol. 15, No. 10, pp. 26-41, 1956

19. Jones, W.P. and, Launder, B.E., "The Calculation of Low Reynolds Number Phenomena with a Two-Equation Model of Turbulence", International Journal of Heat and Mass Transfer, Vol. 16, pp. 1119-1130, 1973

20. Mohamadi, B. and, Pironneau, O. "Analysis of the Kay-Epsilon Turbulence Model", John Wiley & Sons, 1994

21. Haroutinian, V. and, Engelman, M, "On Modelling Wall-Bounded Turbulent Flows Using Specialized Near-Wall Finite Elements and the Standard k- ε Turbulence Model", Advances in Numerical Simulation of Turbulent Flows, ASME, pp. 97-105, 1991

22. Manouzi, H. and, Fortin, M., "A Treatment of Wall Boundaries for Turbulent Flows by the Use of a Transmission Finite Method", International Journal of Numerical Methods in Engineering, Vol. 31, pp. 113-126, 1991

23. Spalding, D.B., "A Single Formula for the Law of the Wall", Journal of Applied Mechanics, Vol. 28, pp. 455-457, 1961

24. Kader, B.A., "Temperature and Concentration Profiles in Fully Turbulent Boundary Layers", Shorter Communications, International Journal of Heat and Mass Transfer, Vol. 24, No. 9, pp. 1541-1544, 1981

25. Gresho. P.M., Lee, R.L., Sani, R.L., Maslanik, M.K., and Eaton, B.E., "The Consistent Galerkin FEM for Computing Derived Boundary Quantities in Thermal and/or Fluids Problems", International Journal for Numerical Methods in Fluids, Vol. 7, pp. 371-394, 1987

26. Thornton, E.A., "Computation of Consistent Boundary Quantities in Finite Element Thermal-Fluid Solutions", Finite Element Flow Analysis, University of Tokyo Press, Tokyo, Japan, pp. 263-270, 1982

27. Sleiman, M., "Simulation of 3D Viscous Compressible Flow in Multistage Turbomachinery by Finite Element Methods", Ph.D. Thesis, CFD Lab, Mechanical Engineering Department, Concordia University, 1999

28. Lepage, C.Y., and Habashi, W.G., "Fluid-Structure Interactions Using the ALE Formulation", AIAA Paper 99-0660, 1999

29. Lepage, C.Y., and Habashi, W.G., "Conservative Interpolation of Aerodynamic Loads for Aeroelastic Computations", AIAA Paper 2000-1449, 2000

30. Schlichting, H., "Boundary Layer Theory", 7th edition, McGraw Hill, 1979

31. Dadone, A., "Presentazione dei Test Cases del Gruppo di Ricerca di Fluidodinamica delle Turbomacchine", Proceedings of the 49th Congresso Nazionale, ATI, pp. 1643-1652, Perugia, 1994

32. Dadone, A., and De Palma, P., "Calcolo di Flussi Viscosi Mediante Formulazione Conservativa Upwind", Proceedings of the 49th Congresso Nazionale, ATI, pp. 1663-1673, Perugia, 1994

33. Heyerichs, K., and Pollard, A., "Heat Transfer in Seperated and Impinging Turbulent Flows", International Journal of Heat and Mass Transfer, Vol. 39, No. 12, pp. 2385-2400, 1996

34. Klebanoff, P.S., "Characterisitcs of Turbulence in a Boundary Layer with Zero Pressure Gradient", N.A.C.A., TN 3178, 1954

35. Vogel, J.C., and Eaton, J.K., "Heat Transfer and Fluid Flow Behind a Backward-Facing Step", Report MD-44, Thermosciences Division, Department of Mechanical Engineering, Stanford University, USA, 1984

36. Van Heiningen, A.R.P., "Heat Transfer under an Impinging Slot Jet", Ph.D. Thesis, McGill University, Canada, 1982

37. Antonelli, P., "Galleria ALN 1.2 x 0.9 m", Alenia Report GENA-73031-4/140/72, 1972

38. Scarsi, R., and Sisti, A., "Proposta e Sperimentazione di un Sistema Antighiaccio Aeronautico Innovativo", M.S. Thesis, University of Genova, 1993

39. Pozzi, A., and Lupo, M., "The Coupling of Conduction with Forced Convection in Graetz Problems", Journal of Heat Transfer, Vol. 112, pp. 323-328, 1990

40. White, F.M., "Viscous Fluid Flow", 2nd Edition, McGraw Hill, 1991

41. Massardo, A.F., and Farinazzo, E., "Experimental Investigation of a New and Energy-Saving Nacelle Anti-Ice System", Journal of Aircraft, Vol. 33, No. 6, 1996

42. Holman, J. P., "Heat Transfer", 7th Edition, McGraw-Hill, 1990